LA-UR-19-30066

Title: HOSS HYBRID OPTIMIZATION SOFTWARE SUITE VERIFICATION and VALIDATION MANUAL

Author(s):
Knight, Earl E.
Rougier, Esteban
Lei, Zhou
Euser, Bryan Jeffry

Intended for: Report

Issued: 2019-10-04 (Draft)

HOSS

HYBRID OPTIMIZATION SOFTWARE SUITE

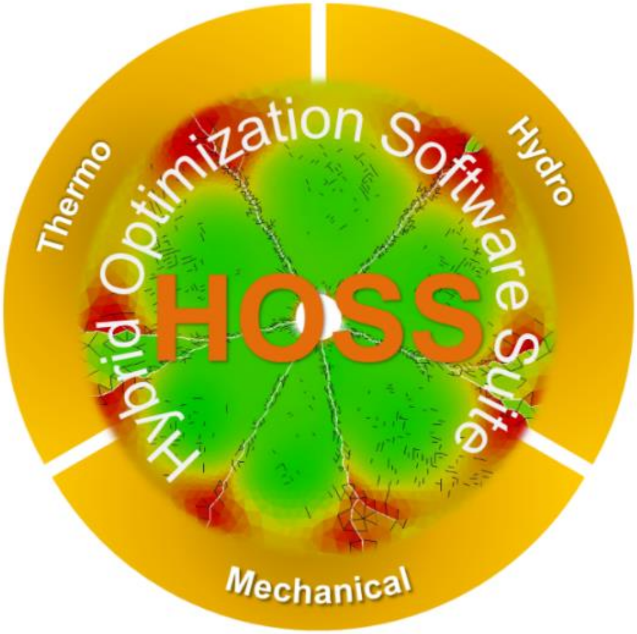

VERIFICATION and VALIDATION MANUAL

Compiled by: Earl E. Knight, Esteban Rougier, Zhou Lei and Bryan Euser

Summary

This verification and validation manual presents a compilation of examples simulated using the Hybrid Optimization Software Suite. This is a "living document" that will be updated periodically as needed. The manual contains the following sections:

- Pure Finite Element
- Fracture
- Fluid-Solid Interaction Solver
- Large Scale

For more information regarding this manual or the benchmark tests presented in here, please refer to the HOSS team:

- Earl E. Knight: knighte@lanl.gov
- Esteban Rougier: erougier@lanl.gov
- Zhou Lei: zlei@lanl.gov
- Bryan Euser: beuser@lanl.gov

Disclaimer: this manual contains a compilation of work conducted by different groups. The authorship of each section is clearly indicated.

Index

List of Tables

List of Figures

1 Pure Finite Element

1.1 Benchmarking and Validation of FDEM

TYPE: Conference Paper

REFERENCE: Proceedings of the 6th International Conference on Discrete Element Methods (DEM6), Golden, Colorado, USA, August 2013.

AUTHORS: Esteban Rougier, Earl E. Knight, Zhou Lei and Ante Munjiza

ABSTRACT: The combined finite discrete element method (FDEM) has become a tool of choice for many discontinua problems in both industrial and research arenas. In this work, a set of benchmark type of validation problems for FDEM is shown and demonstrated through the use of Los Alamos National Laboratory's Hybrid Optimization Software Suite (HOSS) simulation platform.

PROBLEM DESCRIPTION:

A Cantilever Beam under Static Load. The first problem presented in this benchmark is the one shown in Figure 1a, where a cantilever beam loaded with a uniformly distributed load (UDL) is shown.

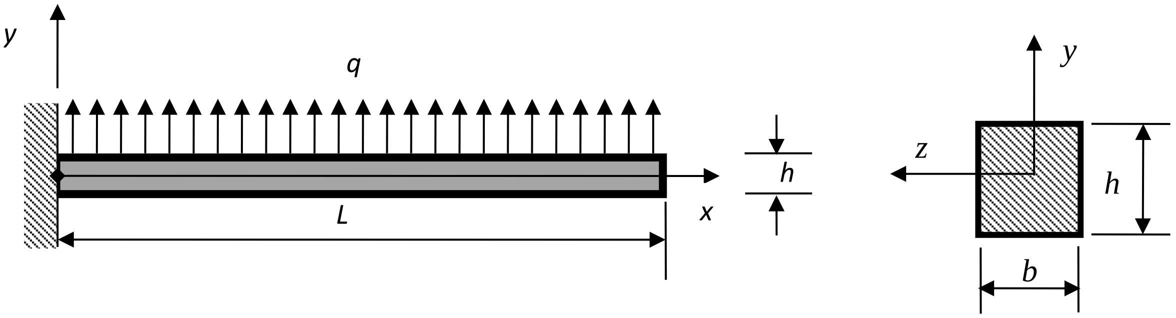

Figure 1. Cantilever beam with uniform distributed load.

For the code validation and verification the following dimensions were adopted

$$\begin{aligned} b &= 1.0\,\mathrm{m} \\ h &= 1.0\,\mathrm{m} \\ L &= 10.0\,\mathrm{m} \end{aligned} \tag{1}$$

The material properties used in this analysis are given by

$$\begin{aligned} \mathrm{E} &= 10.0\ \mathrm{GPa} \\ \nu &= 0.0 \\ \rho &= 1000.0\ \mathrm{kg/m^3} \end{aligned} \tag{2}$$

where E, ν, and ρ are the material's Young's modulus, Poisson's ratio and density. The analytical solution for the tip displacement under static load is given by

$$u_{tip} = \frac{qL^4}{8EI} = 0.015 \text{ m} \tag{3}$$

RESULTS: The tip displacement using HOSS is given in Figure 2. As it can be seen, as the number of elements increases (i.e., the element size decreases), the HOSS solution converges to the theoretical solution, thus demonstrating that FDEM reproduces continuum results obtained by classical FEM codes; but with the added benefit that exact large displacements, finite strains, non-linear material multiplicative decomposition based formulation has been employed.

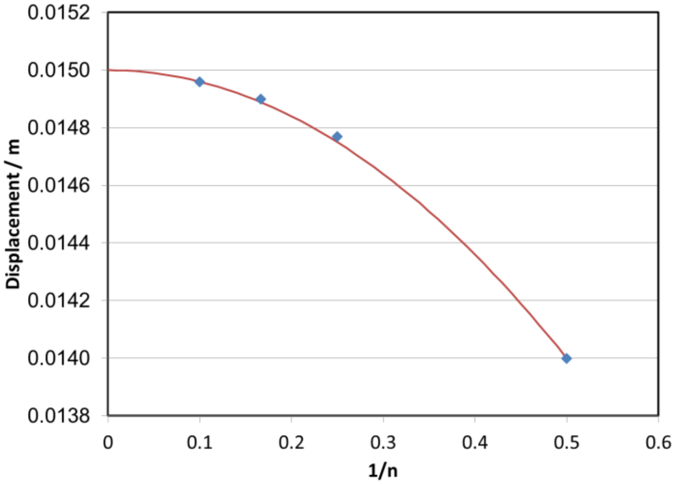

Figure 2. Convergence of the tip displacement with the increase in the number of elements for HOSS code.

A Cantilever beam under dynamic load. The same beam shown in Figure 1 is subjected to the instantaneously rising dynamic UDL. The result of the FDEM simulation obtained using HOSS is shown in Figure 3. As the mesh is refined, HOSS results converge to the theoretical ones, again demonstrating that the multiplicative decomposition based finite strain formulation of FDEM is able to exactly reproduce classical FEM simulation results.

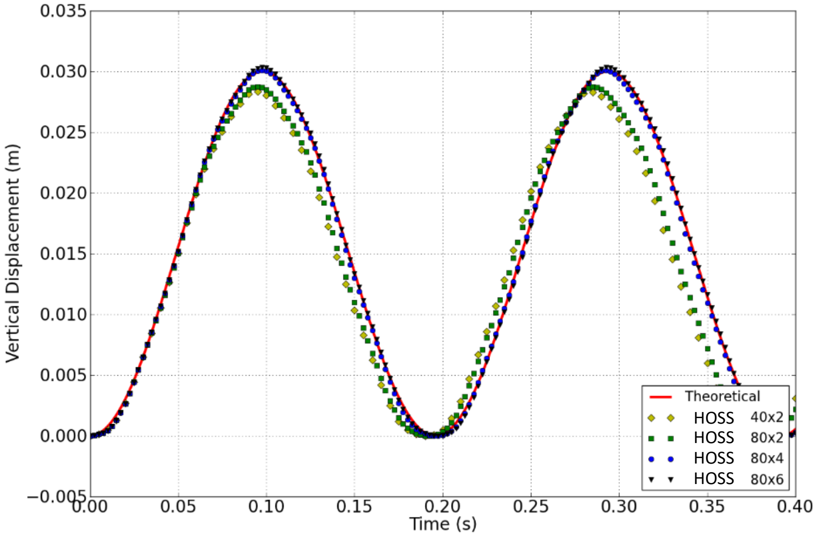

Figure 3. Cantilever beam. Deflection at the tip of the beam. Comparison of dynamic solution obtained by HOSS versus theoretical results.

1.2 Stresses Surrounding a Wellbore

TYPE: Internal Report

REFERENCE: N/A

AUTHORS: Angel M. Padilla

PROBLEM DESCRIPTION:

In this problem, a square with a circular hollow center is used to represent a wellbore. The stress state surrounding the hole is analyzed both analytically and through HOSS simulations. The system is configured as shown in Figure 4, where it can be seen that an internal pressure is applied on the wall of the borehole while additional far field stresses are imposed on the boundary of the model. The maximum principal stress, σ_H, is applied horizontally while the minimum principal stress, σ_h, is applied vertically on the sides of the square.

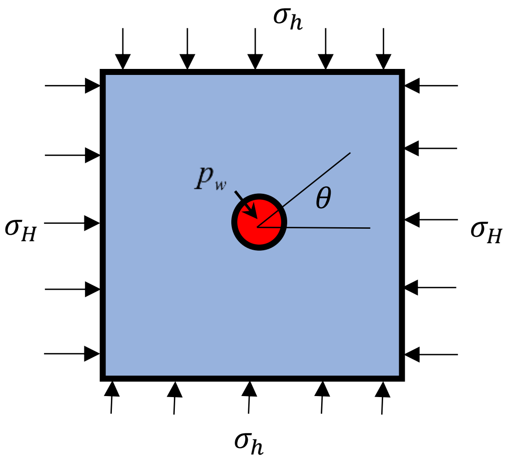

Figure 4. Schematic setup of the problem. σ_h and σ_H are the minimum and maximum principal stresses respectively, θ is the angle measured from the direction defined by $+\sigma_H$, and p_w is the internal pressure inside the borehole.

The radial and tangential (Hoop) stresses are used as a benchmark. The theoretical solutions for the evolution of the radial (σ_r) and Hoop/tangential (σ_θ) stresses as a function of the distance r and the angle θ are given by

$$\sigma_r = \frac{1}{2}(\sigma_H+\sigma_h)\left(1-\frac{r_w^2}{r^2}\right)+\frac{1}{2}(\sigma_H-\sigma_h)\left(1+3\frac{r_w^4}{r^4}-4\frac{r_w^2}{r^2}\right)\cos(2\theta)+\frac{r_w^2}{r^2}p_w \tag{4}$$

$$\sigma_\theta = \frac{1}{2}(\sigma_H+\sigma_h)\left(1+\frac{r_w^2}{r^2}\right)-\frac{1}{2}(\sigma_H-\sigma_h)\left(1+3\frac{r_w^4}{r^4}\right)\cos(2\theta)-\frac{r_w^2}{r^2}p_w \tag{5}$$

where r_w is the radius of the borehole, p_w is the pressure inside the borehole, and σ_h and σ_H are the minimum and maximum principal stresses respectively. The results obtained from HOSS were compared to the analytical solutions for the array of points shown in Figure 5.

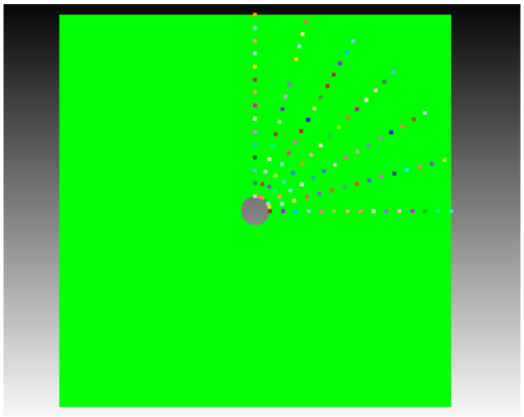

Figure 5. Depiction of the array of points used for the comparison between HOSS and the analytical solutions.

RESULTS:

For this simulation, a geometry consisting of a 4m x 4m square with a circle of radius 0.15m was chosen. The mesh size used for this model was 0.007m. 105 sensors are spaced from 0 degrees to 90 degrees at 15 degree increments to provide more information at these points, see Figure 5. The material properties and the boundary conditions used for this benchmark are listed in Table 1.

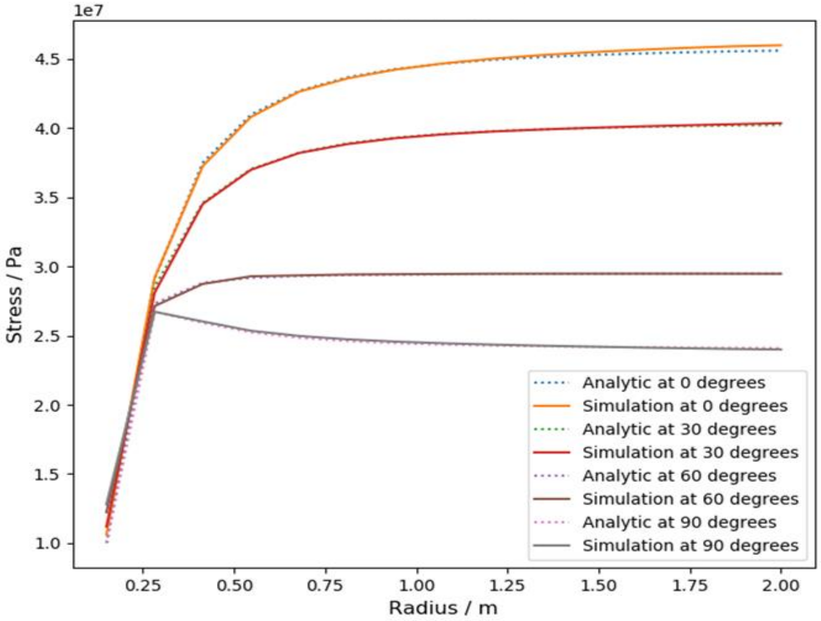

Figure 6. Comparison of the evolution of the radial stress σ_r as a function of distance for different azimuth angles θ .

Table 1. Material properties and boundary condition values.

Parameter	Value
Young's modulus / Pa	1.853e10
Poisson's ratio	0.22
Density / (kg/m^3)	7.8e3
p_w / Pa	1.0e7
σ_h / Pa	2.4e7
σ_H /Pa	4.6e7

The comparison between the results obtained from HOSS and the analytical solution are shown in Figure 6 and Figure 7, where a very good match between the numerical results and the theoretical ones can be seen.

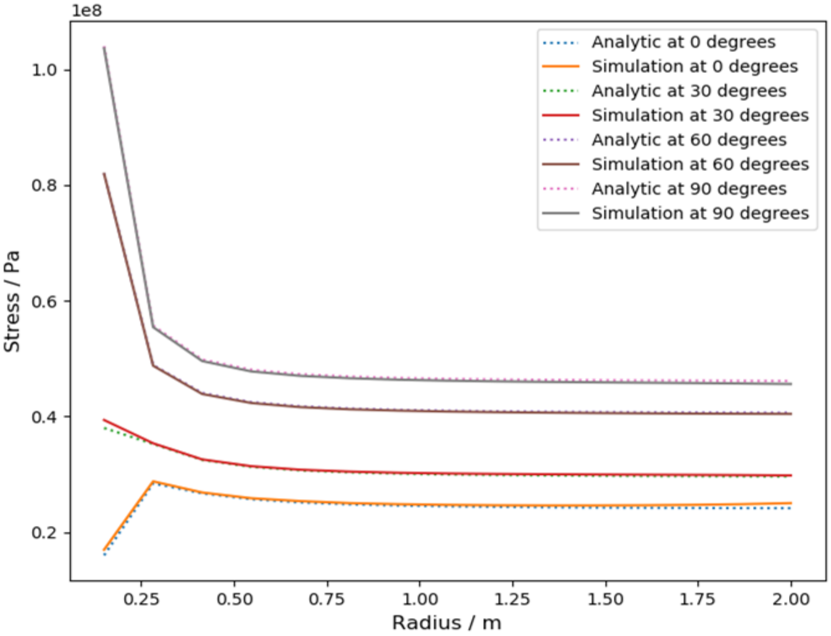

Figure 7. Comparison of the evolution of the tangential stress σ_θ as a function of distance for different azimuth angles θ .

REFERENCES:

J. Zhang, C. Ai, B. Zeng, Y. Li, J. Zeng, "Study on Wellbore Stability of Shallow Sediments in Deepwater Drilling," in *The Open Petroleum Engineering Journal*, Sept. 2017. [Online]. Available: https://benthamopen.com/FULLTEXT/TOPEJ-10-48

J. Zhang, M. Bai, J. Roegiers, "Dual-porosity poroelastic analyses of wellbore stability," in *International Journal of Rock Mechanics and Mining Sciences*, Feb. 2003. [Online]. Available: https://www.researchgate.net/publication/34032781_Dual-porosity_approach_to_wellbore_stability_in_naturally_fractured_reservoirs

S. He, W. Wang, J. Zhou, Z. Huang, M. Tang, "A model for analysis of wellbore stability considering the effects of weak bedding planes," in *Journal of Natural Gas Science and Engineering*, Sept. 2015. [Online]. Available: https://www.researchgate.net/publication/282590157_A_Model_for_Analysis_of_Wellbore_Stability_Considering_the_Effects_of_Weak_Bedding_Planes

S. Grandi, R. Rao, M. Toksoz, "Geomechanical Modeling of In-Situ Stresses Around a Borehole," Dept. of Earth, Atmospheric, and Planetary Sciences, Massachusetts Institue of Technology, Cambridge, MA, US, July 25,

2019. [Online]. Available: https://pdfs.semanticscholar.org/8f5c/f23a3b4640b9244783931a314275db7de518.pdf

1.3 Thick Walled Cylinder with Internal Pressure

TYPE: Internal Report

REFERENCE: N/A

AUTHORS: Angel M. Padilla

PROBLEM DESCRIPTION:

For this problem, a thick walled cylinder with an internal pressure is analyzed both analytically and through HOSS simulations. A thick walled cylinder is defined as having a radius to thickness ratio of less than or equal to 10. To analyze this problem, both the tangential (hoop) stress and radial stresses at several locations along the wall of the cylinder are considered.

ANALYTIC SOLUTION:

The following equations are used to calculate tangential stress (σ_t) and radial stress (σ_r)

$$\sigma_r = \frac{a^2 p_i}{b^2 - a^2}\left(1 - \frac{b^2}{r^2}\right) \tag{6}$$

$$\sigma_t = \frac{a^2 p_i}{b^2 - a^2}\left(1 + \frac{b^2}{r^2}\right) \tag{7}$$

where a and b are the inner and outer radius of the cylinder respectively, p_i is the pressure inside the cavity (inside the inner radius) and r is the radial distance measured from the center of the cylinder, see Figure 8.

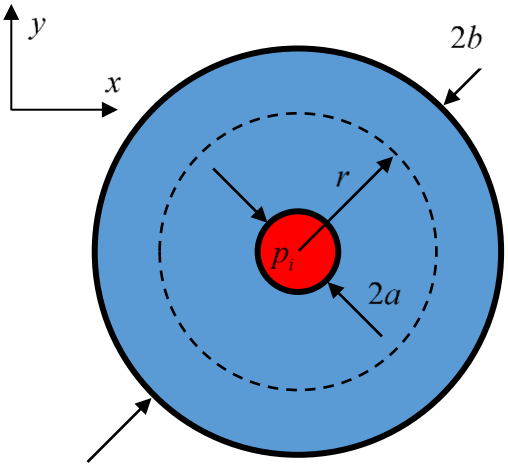

Figure 8. General setup.

RESULTS:

For this benchmark the dimensions of the cylinder were set to $a = 1\text{ m}$ and $b = 10\text{ m}$, while the material properties and the boundary conditions used are listed in Table 2. A set of sensors was located at 0.25m increments along the radius of the cylinder. The mesh size used for this simulations was 0.065m. In order to obtain the static solution of the problem a mass-proportional damping was used in the simulations, to dissipate the dynamic waves traveling through the model. The results obtained for σ_{xx}, σ_{yy} and σ_{xy} stresses along a line coinciding with the x axis are shown in Figure 9.

Table 2. Material properties and boundary condition values.

Parameter	Value
Young's modulus / Pa	2.0e11
Poisson's Ratio	0.26
Density / (kg/m^3)	7.8e3
p_i /Pa	1.0e7

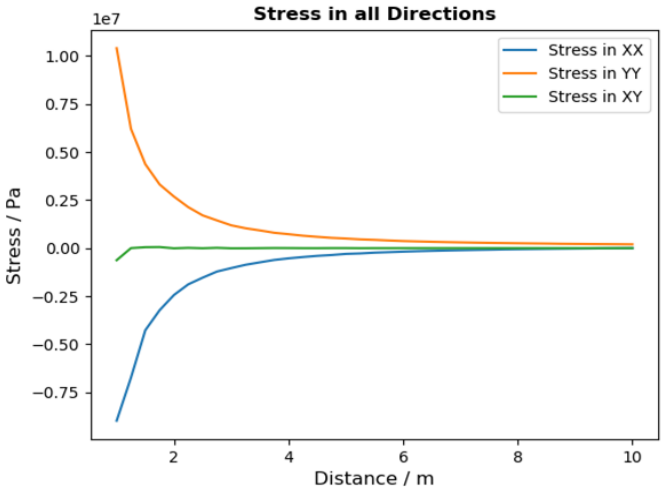

Figure 9. Evolution of σ_{xx}, σ_{yy} and σ_{xy} stresses along a line coinciding with the x axis (see Figure 8).

The comparison of the numerical solution against the analytic one is shown in Figure 10. As shown in the figure, the results of the HOSS simulation are almost on top of the analytic solution. The percent error between the analytic and simulation results are 2.43% for radial stress with a confidence of two standard deviations. For tangential stress, the percent error is 2.08%.

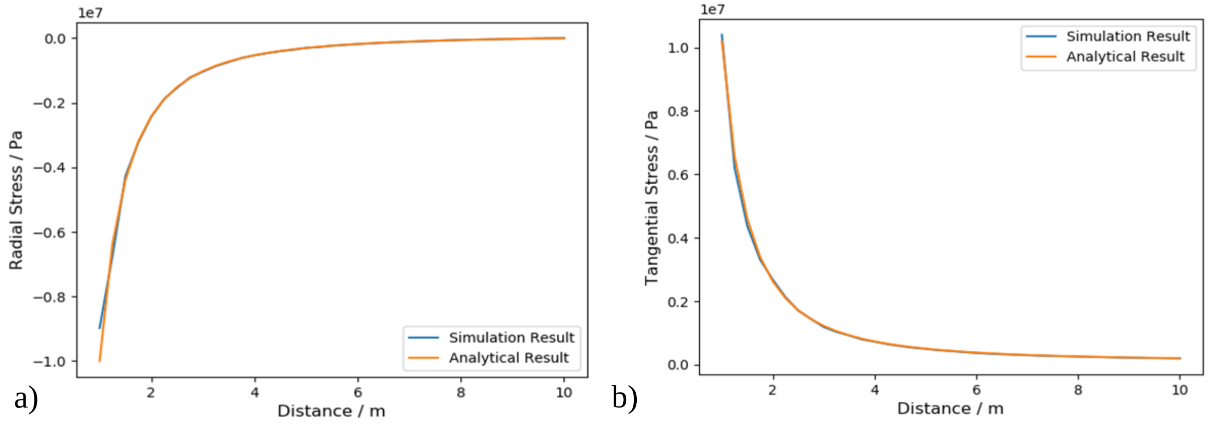

a) b)

Figure 10. Comparison between the numerical and the analytical solutions. a) Radial stress. b) Tangential stress.

A convergence study was conducted in order to determine how the results are affected by the mesh size. The mesh sizes selected for this study were 0.500 m, 0.250 m, 0.100 m, and 0.065 m. The results obtained are shown in Figure 11 where it is clear that, as the mesh size decreases, the numerical solution tends to the analytical one.

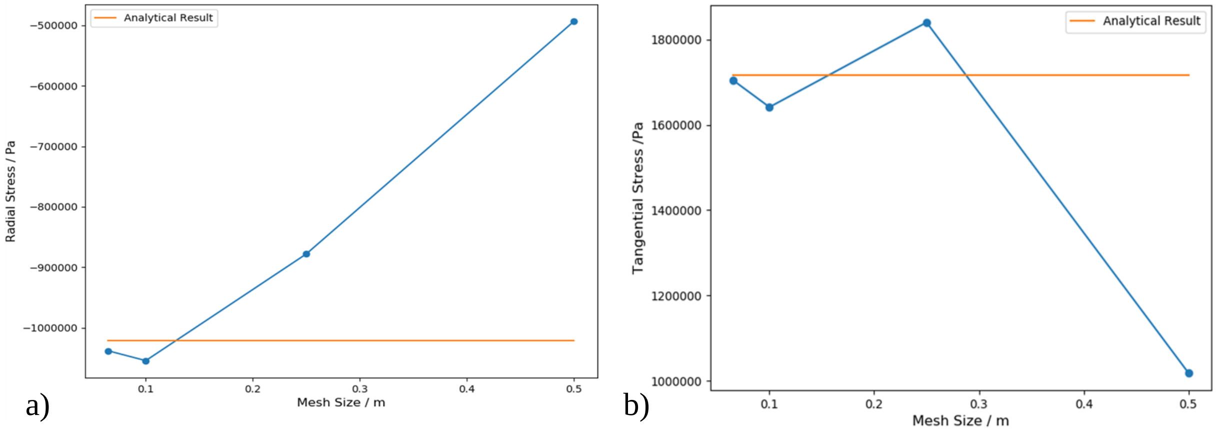

a) b)

Figure 11. Convergence study. a) Radial stress. b) Tangential stress.

REFERENCES:

"Thick Walled Cylinders." Memorial University.
http://www.engr.mun.ca/~katna/5931/Thick%20Walled%20Cylinders(corrected).pdf

S. Choudhury, "Stress Analysis of Thick Walled Cylinders," B.S. thesis, Dept. Mech. Eng., National Institute of Tech., Rourkela Odisha, India, 2010.

1.4 A Generalized Anisotropic Deformation Formulation

TYPE: Peer Reviewed Paper

REFERENCE: A generalized anisotropic deformation formulation for geomaterials. Computational Particle Mechanics, 3:215-228, 2016. https://doi.org/10.1007/s40571-015-0079-y

AUTHORS: Z. Lei, E. Rougier, E.E. Knight, A. Munjiza, and H. Viswanathan

ABSTRACT: In this work, the combined finite-discrete element method (FDEM) has been applied to analyze the deformation of anisotropic geomaterials. In the most general case geomaterials are both non-homogeneous and non-isotropic. With the aim of addressing anisotropic material problems, improved 2D FDEM formulations have been developed. These formulations feature the unified hypo-hyper elastic approach combined with a multiplicative decomposition-based selective integration for volumetric and shear deformation modes. This approach is significantly different from the co-rotational formulations typically encountered in finite element codes. Unlike the co-rotational formulation, the multiplicative decomposition-based formulation naturally decomposes deformation into translation, rotation, plastic stretches, elastic stretches, volumetric stretches, shear stretches, etc. This approach can be implemented for a whole family of finite elements from solids to shells and membranes. This novel 2D FDEM based material formulation was designed in such a way that the anisotropic properties of the solid can be specified in a cell by cell basis, therefore enabling the user to seed these anisotropic properties following any type of spatial variation, for example, following a curvilinear path. In addition, due to the selective integration, there are no problems with volumetric or shear locking with any type of finite element employed.

PROBLEM DESCRIPTION:

Wave Propagation around a Borehole

In this section, the implementation of the unified material model is illustrated using a 2D square block with a circular borehole in a center, as shown in Figure 12. The model was exercised with isotropic and with anisotropic materials that had Poisson's ratios of 0.00 and 0.25.

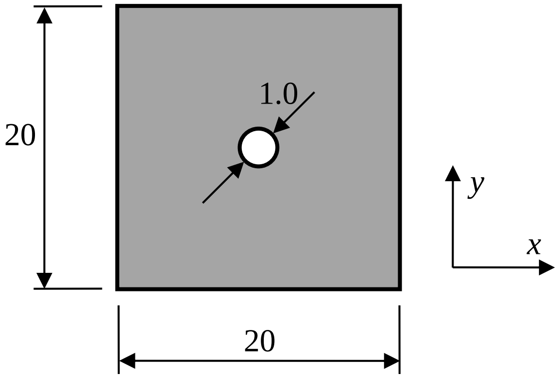

Figure 12. General dimensions of the model (all dimensions in meters).

A pressure pulse described by a Heaviside step function with a magnitude of 1.0 MPa was applied to the borehole at the beginning of the simulation. Two types of materials were considered: an isotropic material and a general anisotropic material.

For each case, four different orientations for the material axes $\left[\boldsymbol{\alpha} \quad \boldsymbol{\beta}\right]$ were used, as shown in Figure 13. In all four cases the material axis $\boldsymbol{\alpha}$ and $\boldsymbol{\beta}$ are orthogonal to each other. In Figure 13-a, the material axis $\boldsymbol{\alpha}$ is collinear with the x-axis across the whole model. The material axis orientation shown in Figure 13-b is the same as the one shown in Figure 13-a, but rotated 45º counter-clockwise. Figure 13-c shows a general orientation of the material axes that changes from finite element to finite element. The orientation of the material axis shown in Figure 13-d is the same as the one shown in Figure 13-c, but rotated 45º counter-clockwise.

For the sake of comparing the waveforms obtained with the different material axes orientations, the monitoring points shown in Figure 13 were introduced. In all cases, the radial range of the monitoring points was set to 5 m. For the cases shown in Figure 13-a and Figure 13-c, the monitoring points were located along the x axis while for the cases shown in Figure 13-b and Figure 13-d their positions were rotated 45 degrees counter-clockwise to facilitate the comparison of the radial velocity histories.

Poisson's Ratio = 0.00. For the isotropic case the material properties were given by

$$M_v = 0.0\,\text{GPa} \quad ; \quad M_\alpha = M_\beta = M_\psi = 1.0\,\text{GPa} \quad ; \quad \rho = 1000.0\,\text{kg/m}^3 \qquad (8)$$

For the anisotropic case the material properties used were the same as the ones listed above with the following exception

$$M_\beta = 2.0\,\text{GPa} \qquad (9)$$

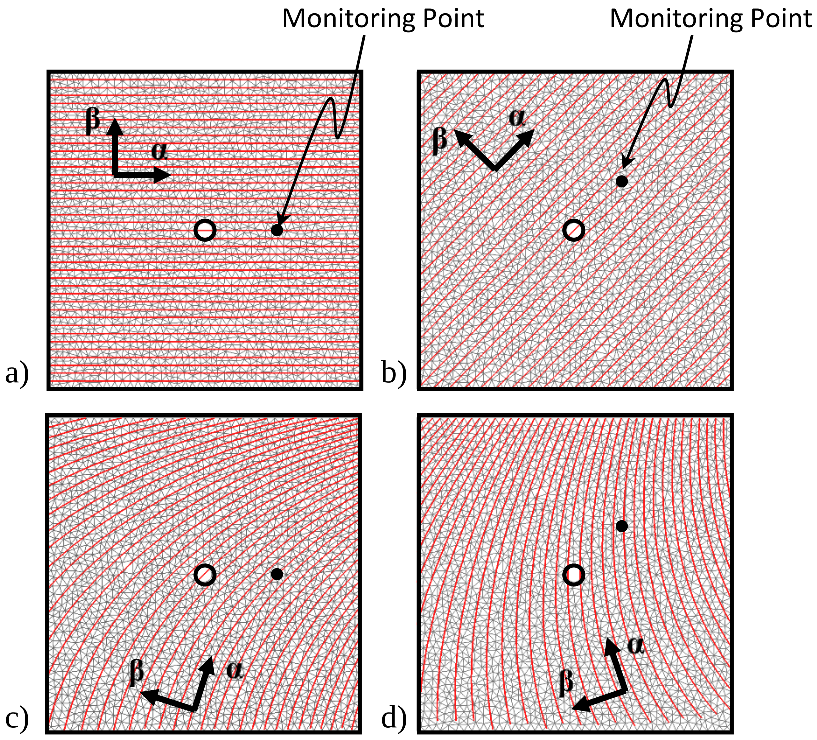

Figure 13. Orientation of the material axis $\boldsymbol{\alpha}$: a) horizontal, b) 45º, c) general #1, and d) general #2. The black dots identify the position of the monitoring points for each case.

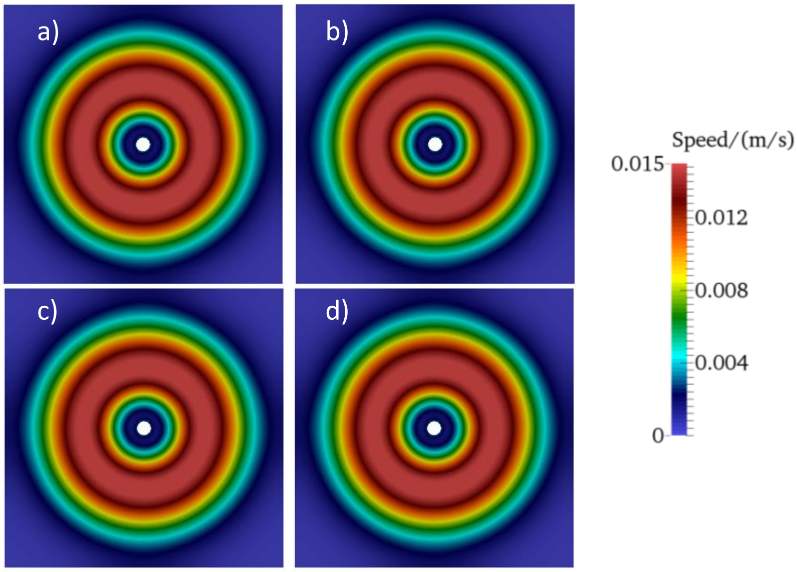

Figure 14. Wave propagation for the isotropic material model with $\nu = 0.00$: a) horizontal, b) 45º, c) general #1, and d) general #2.

A snapshot of the wave propagation for the case with an isotropic material is shown in Figure 14. As expected, the wave front preserves a circular shape regardless of the orientation of the material axes. This is also confirmed by the analysis of the radial velocity time histories which are shown in Figure 15. All four curves fall on top of each other which demonstrates that the formulation is not sensitive to the orientation of the material axes.

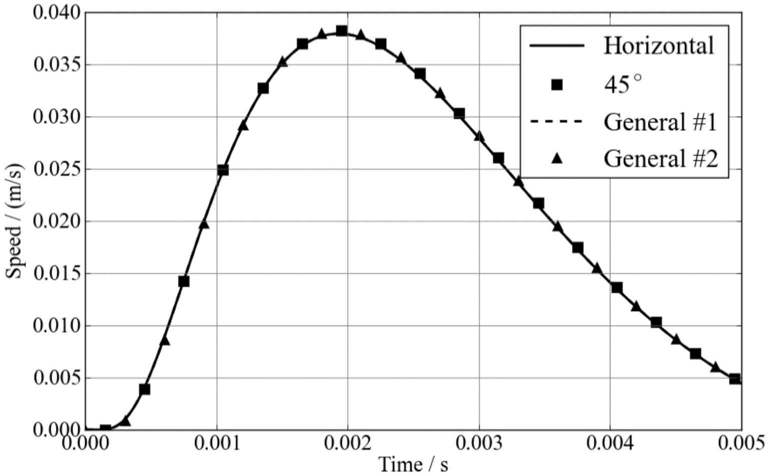

Figure 15. Isotropic Material case: comparison of the time histories of the radial speed for the monitoring points shown in Figure 13.

A snapshot of the wave propagation for the case with an anisotropic material is shown in Figure 16. In this case, the shape of the wave propagation front is strongly affected by the orientation of the material axes.

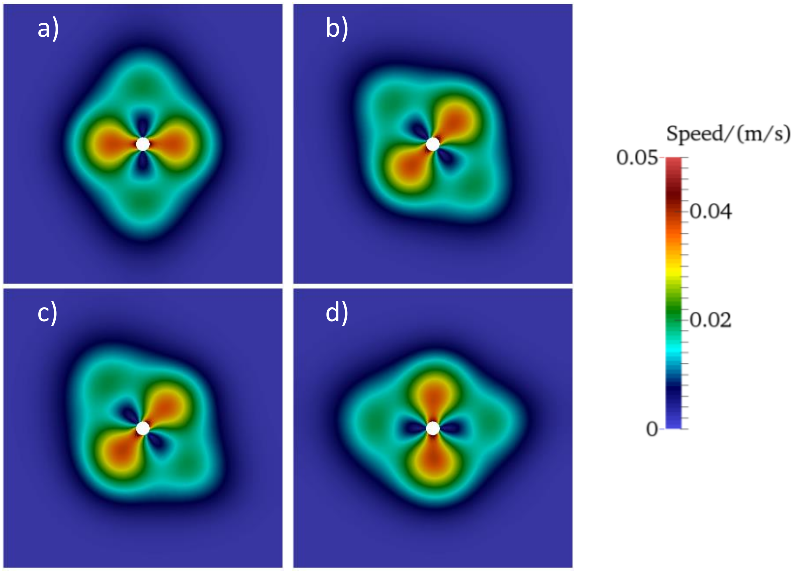

Figure 16. Wave propagation for the anisotropic material model with $\nu = 0.00$: a) horizontal, b) 45º, c) general #1, and d) general #2.

For the general anisotropic case the independence of the results with respect to the orientation of the material axes is demonstrated by comparing Figure 16-a against Figure 16-b rotated 45º clockwise and Figure 16-c against Figure 16-d, also rotated 45º clockwise. These comparisons are shown in Figure 17 with the help of isolines. The red isolines correspond to the un-rotated results (Figure 16-a and Figure 16-c), while the white isolines correspond to the rotated results (Figure 16-b and Figure 16-d). A comparison of the velocity histories for the two monitoring points for the general anisotropic case is shown in Figure 18. It is evident that there is no change in the wave propagation front as the material axis are rotated.

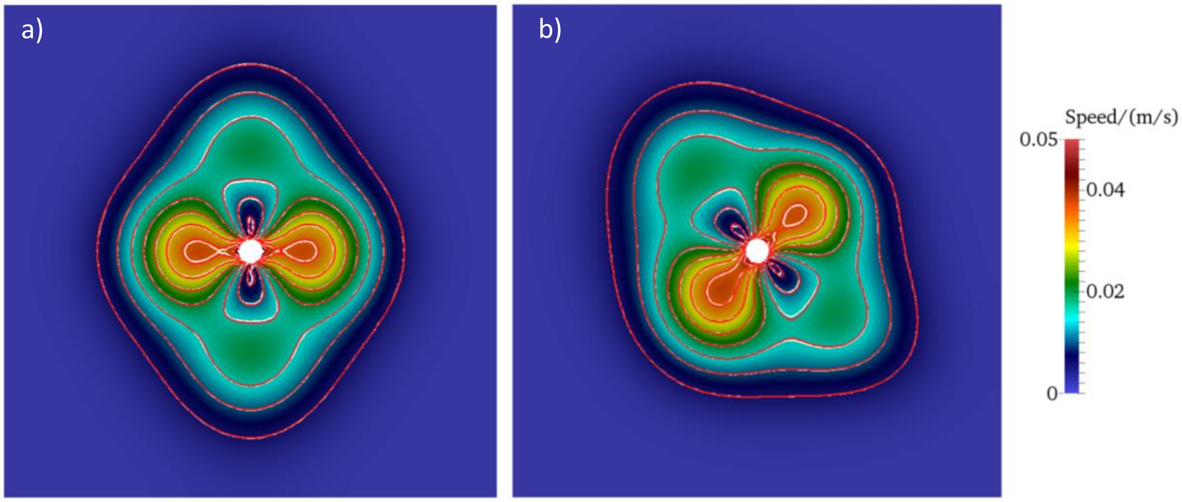

Figure 17. Wave propagation for the anisotropic material model with $\nu = 0.00$: a) horizontal and b) general.

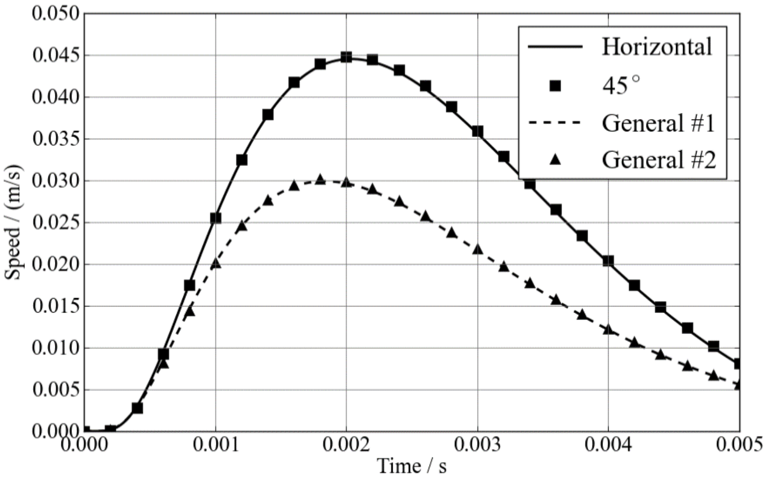

Figure 18. Comparison of radial speed for monitoring points shown in Figure 13.

Poisson's Ratio = 0.25. The same model used in the previous example was used to test the composite triangle formulation implemented in HOSS for a case with Poisson's ratio

$$\nu = 0.25 \tag{10}$$

For the isotropic case the material properties were given by

$$M_\nu = 0.267\,\text{GPa} \quad ; \quad M_\alpha = M_\beta = M_\psi = 0.800\,\text{GPa} \quad ; \quad \rho = 1000.0\,\text{kg/m}^3 \tag{11}$$

For the anisotropic case the material properties used were the same as the ones listed above with the following exception

$$M_\beta = 1.600\,\text{GPa} \tag{12}$$

A snapshot of the wave propagation for the case with an isotropic material is shown in Figure 19. As in the previous example, the wave front preserves a circular shape regardless of the orientation of the material axes.

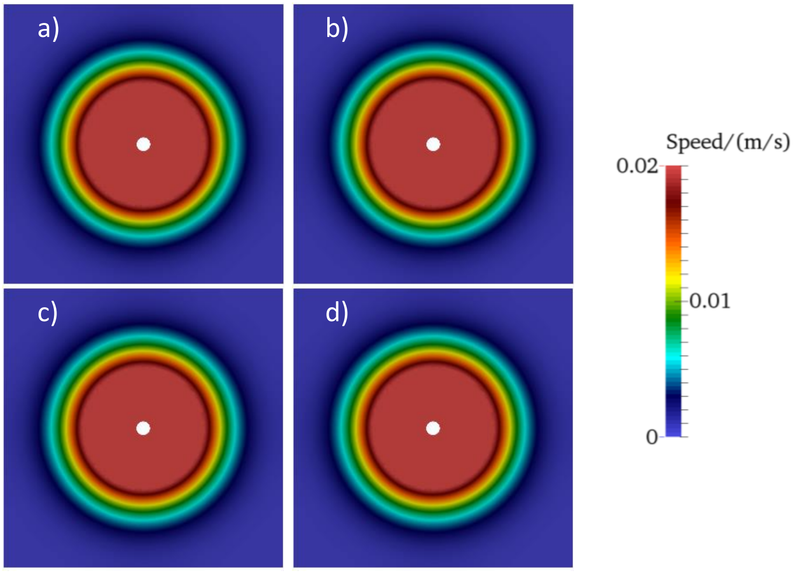

Figure 19. Wave propagation for the isotropic material model with $\nu = 0.25$: a) horizontal, b) 45º, c) general #1, and d) general #2.

A snapshot of the wave propagation for the case with an anisotropic material is shown in Figure 20. As in the previous example, the shape of the wave propagation front is strongly affected by the orientation of the material axes.

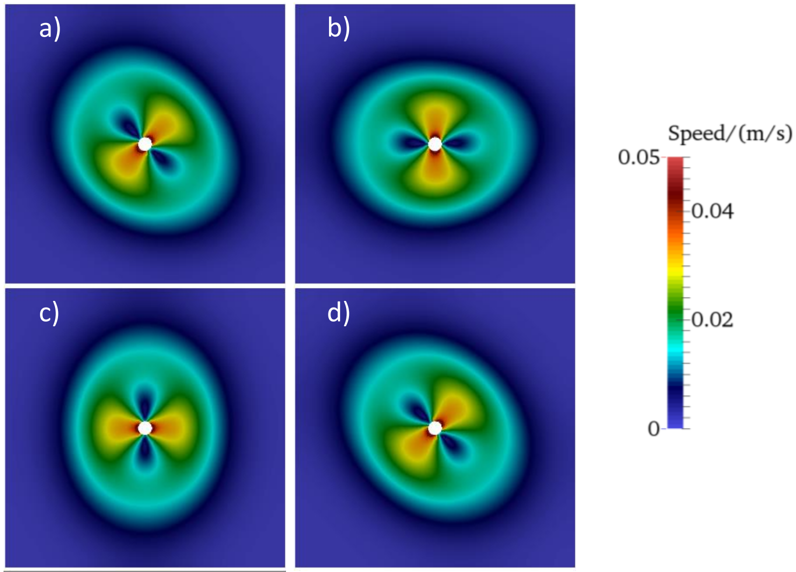

Figure 20. Wave propagation for the anisotropic material model with $\nu = 0.25$: a) horizontal, b) 45º, c) general #1, and d) general #2.

The comparisons of the wave fronts and of the radial velocity time histories for the matching cases are shown in Figure 21 and in Figure 22. There is virtually no difference between the un-rotated and the rotated material axes cases, as it should be.

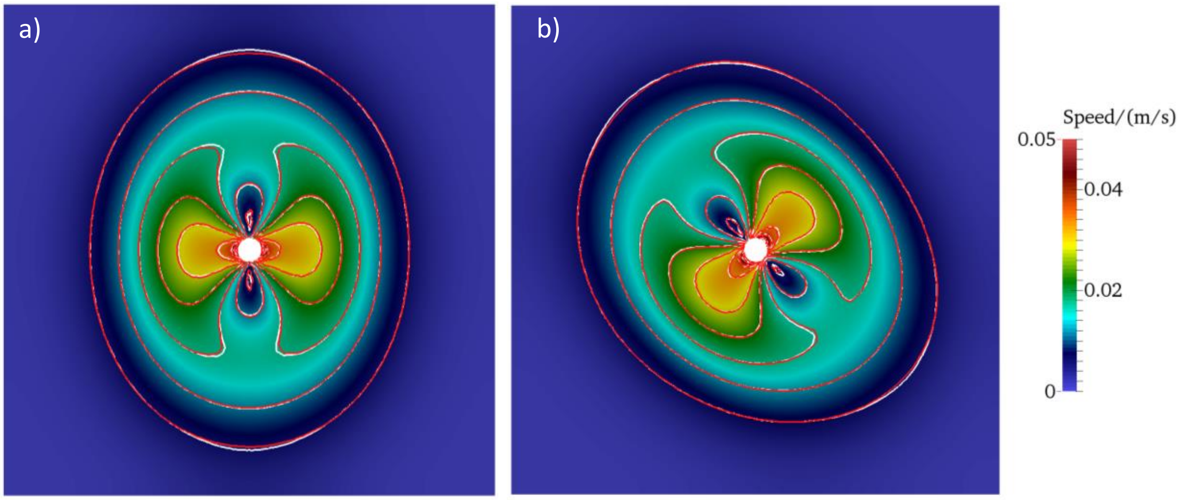

Figure 21. Wave propagation for the anisotropic material model with $\nu = 0.25$: a) horizontal and b) general.

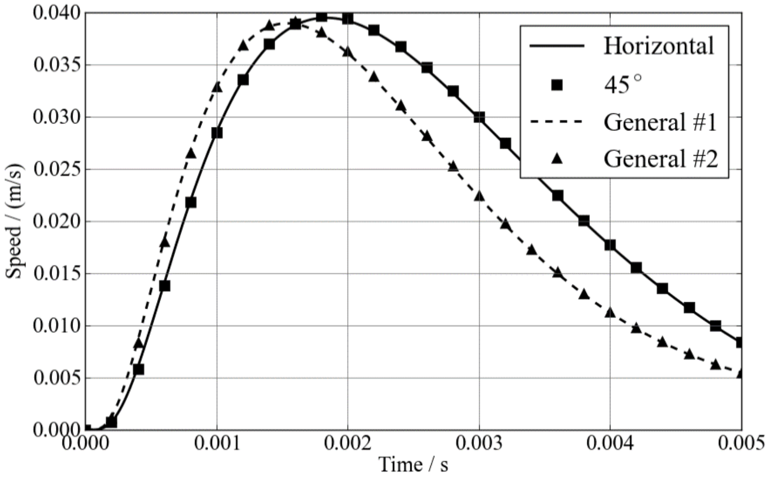

Figure 22. Comparison of radial speed for monitoring points shown in Figure 13.

Behavior under Volumetric Locking Conditions

Figure 23 shows one of the models that was used to demonstrate that the composite element proposed here does not suffer from the problems generated by volumetric locking. The model consists of a square with the left and bottom edges fixed and a force

$$\mathbf{f} = \begin{bmatrix} f_i \\ f_j \end{bmatrix} \tag{13}$$

applied to the corner node. The example was run under plane stress and plane strain conditions utilizing a standard constant strain triangle (CST) formulation and the composite triangle (COMPT) proposed in this work. Since the aim of this exercise was to obtain the quasi-static response of the system, the simulations were damped accordingly. Therefore, the results shown in this section correspond to the static solutions.

For the plane stress case the Munjiza elastic constants used are

$$M_v = M_\alpha = M_\beta = M_\psi = 0.667\,\text{GPa} \;\; ; \;\; \rho = 1000.0\,\text{kg/m}^3 \tag{14}$$

These constants were derived considering $E = 1.0\,\text{GPa}$ and $\nu = 0.5$. For the plane strain case the Munjiza elastic constants used are

$$M_v = 1{,}666.4\,\text{GPa} \;\; ; \;\; M_\alpha = M_\beta = M_\psi = 0.667\,\text{GPa} \;\; ; \;\; \rho = 1000.0\,\text{kg/m}^3 \tag{15}$$

It is worth noting that in this case the Poisson's ratio was set to 0.4999.

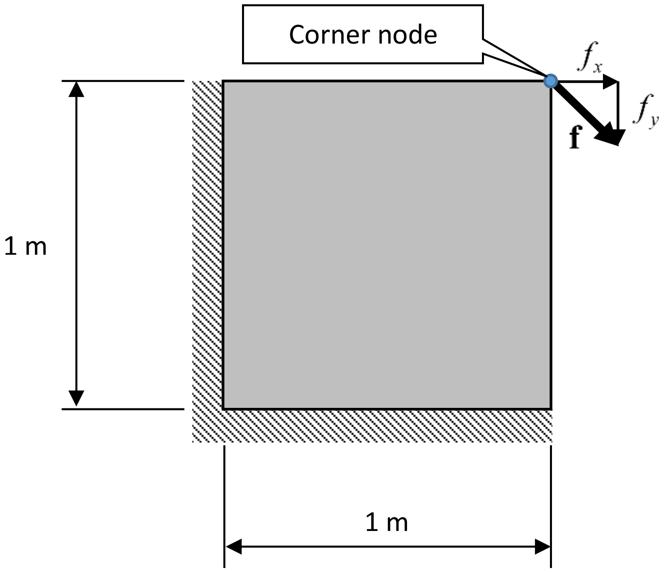

Figure 23. Model setup for volumetric locking test with corner force.

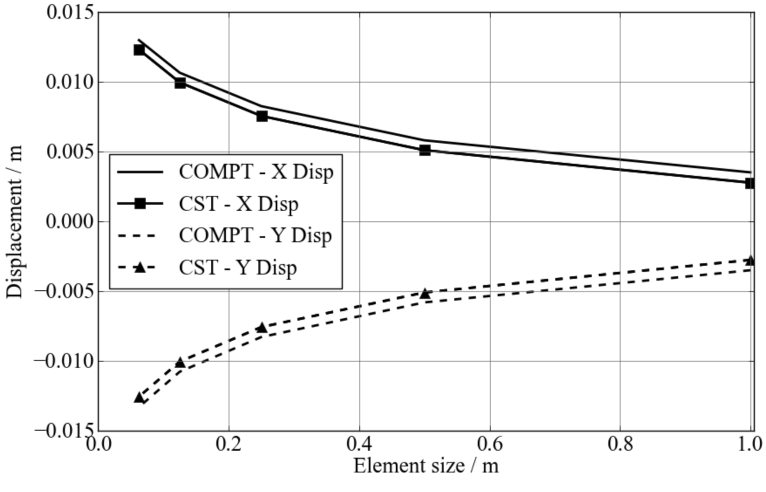

Figure 24. Evolution of the x- and y-displacements of the corner node for the plane stress case.

The results obtained for the x- and y-displacements of the corner node as a function of the element size for the plane stress case are shown in Figure 24. The response obtained from the COMPT model is consistently softer that the one obtained from the CST model, as it is expected to be. These differences in displacement response do not change substantially relative to each other as the element size is decreased. A snapshot of the x component of the Cauchy stress tensor (**C**$_{xx}$)

for both cases is shown in Figure 25. The stress map in both cases is quite uniform, except around the corner where the force is being applied. It is worth noting that the CST case shows a much more pronounced checkerboard pattern effect around the corner than the COMPT case.

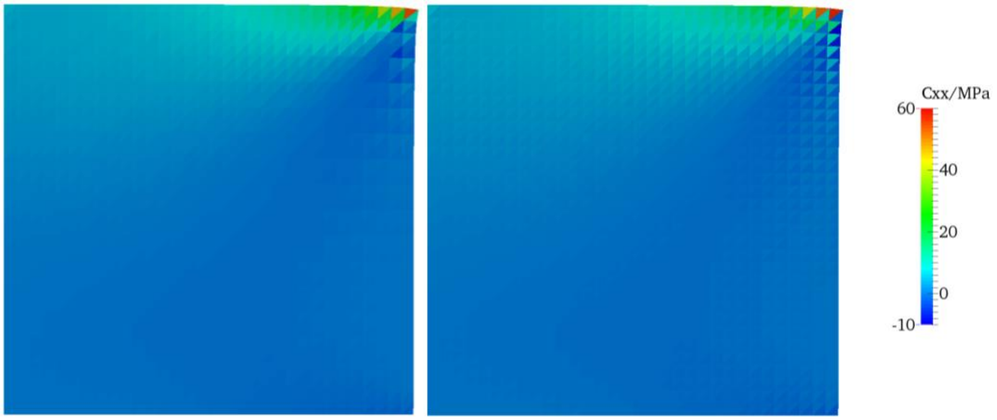

Figure 25. Stress distribution in the plane stress case: a) with the COMPT and b) with the CST.

For the plane strain case, the story is quite different. The x- and y-displacements of the corner nodes as a function of the element size are shown in Figure 26. The CST case exhibits very strong volumetric locking effects resulting in an almost non-existent displacement of the corner node. On the other hand, the COMPT model is not affected by this, as is demonstrated by the curves shown in Figure 26.

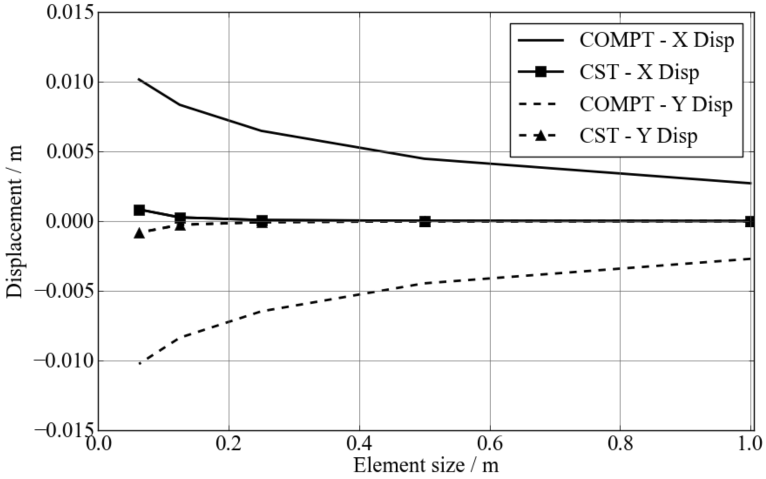

Figure 26. Evolution of the x- and y-displacements of the corner node for the plane strain case.

The snapshots of the x component of the Cauchy stress tensor for the CST and for the COMPT models in plane strain conditions are shown in Figure 27. The stress field obtained for the CST shows a very strong “checkerboard” pattern effect caused by the volumetric locking of the elements. On the other hand, the stress field obtained for the COMPT is very smooth, with only some incipient evidence of “checkerboard” pattern effect close to the corner where the force is being applied.

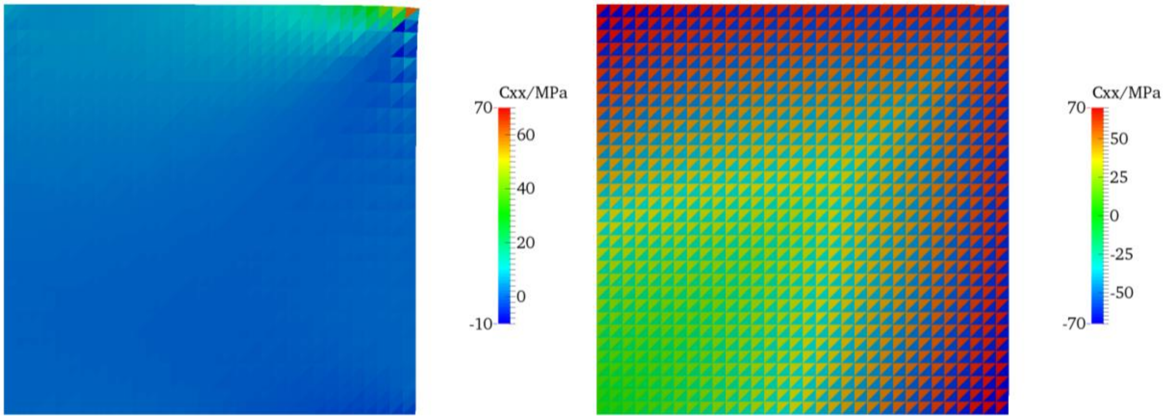

Figure 27. Stress distribution in the plane strain case: a) with the COMPT and b) with the CST.

Another example to demonstrate the absence of volumetric locking problems for the composite triangles is shown in Figure 28. In this case, a constant body force $p = 1000\,\text{Pa}$ was applied to both sides of the sample, as shown in the figure. In this example, two different values of the Poisson's ratio were tested under plain strain conditions: $\nu_1 = 0.25$ and $\nu_2 = 0.4999$. The results obtained for both cases are shown in Figure 29. For the cases of $\nu = 0.25$ there is no significant difference between the results obtained by using either the constant strain triangle or the composite triangle. However, when $\nu = 0.4999$ the consequences of the constant strain triangle locking problems are quite evident, as demonstrated by the checkerboard pattern effect shown in Figure 29-d.

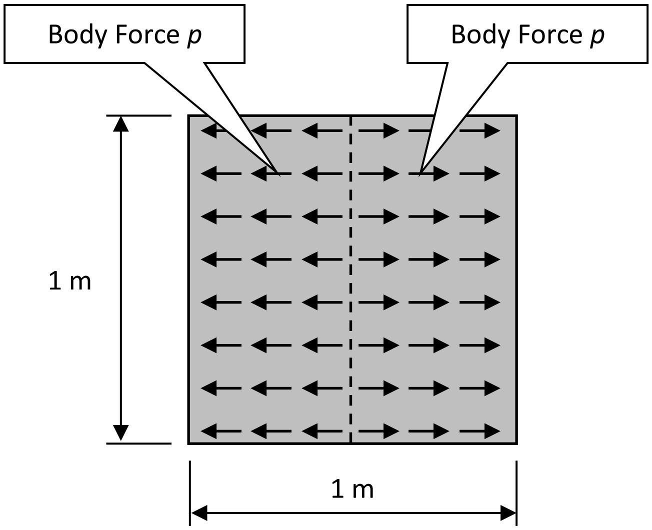

Figure 28. System setup for volumetric locking test with body force.

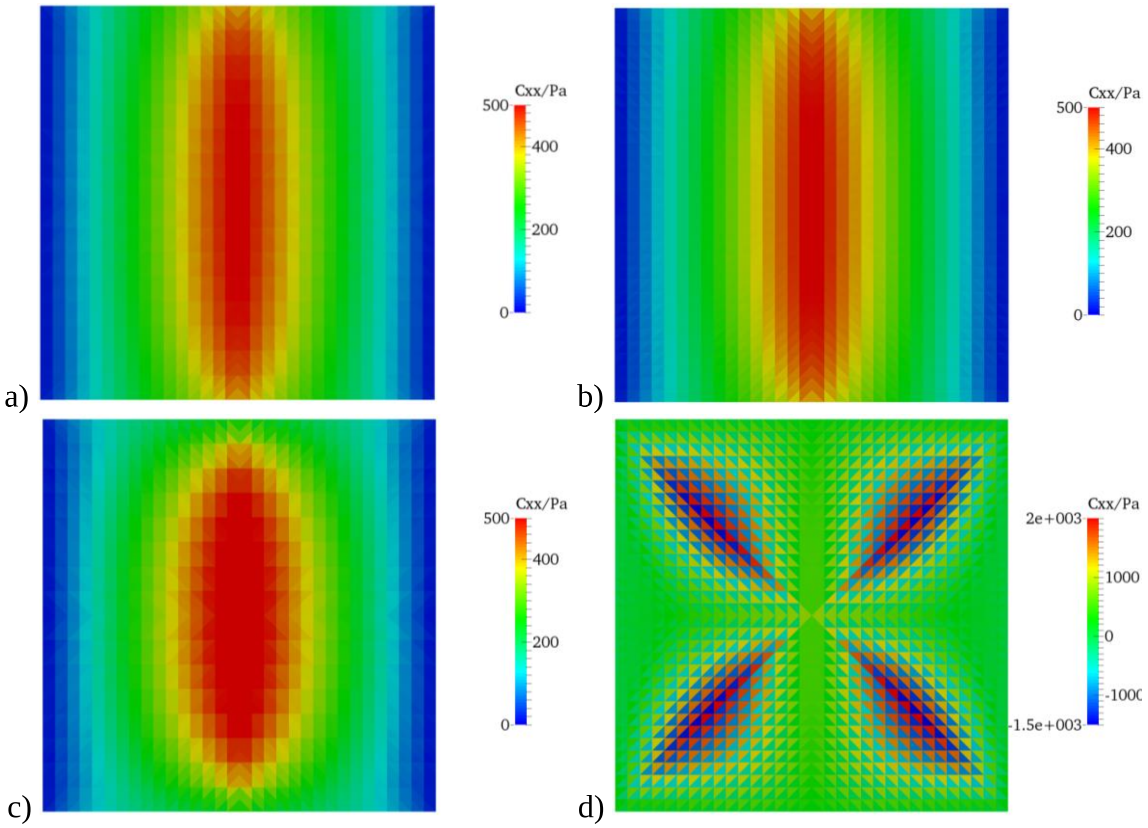

Figure 29. Stress distribution in the plane strain case: a) COMPT – $\nu_1 = 0.25$, b) CST – $\nu_1 = 0.25$, c) COMPT – $\nu_2 = 0.4999$, and d) CST – $\nu_2 = 0.4999$.

Numerical Illustration: Influence of Anistropic Material Properties on Geomaterials under Blast Loading

Finally, a more realistic type of problem was simulated using both isotropic and anisotropic material descriptions. For this purpose, the model shown in Figure 30 was utilized.

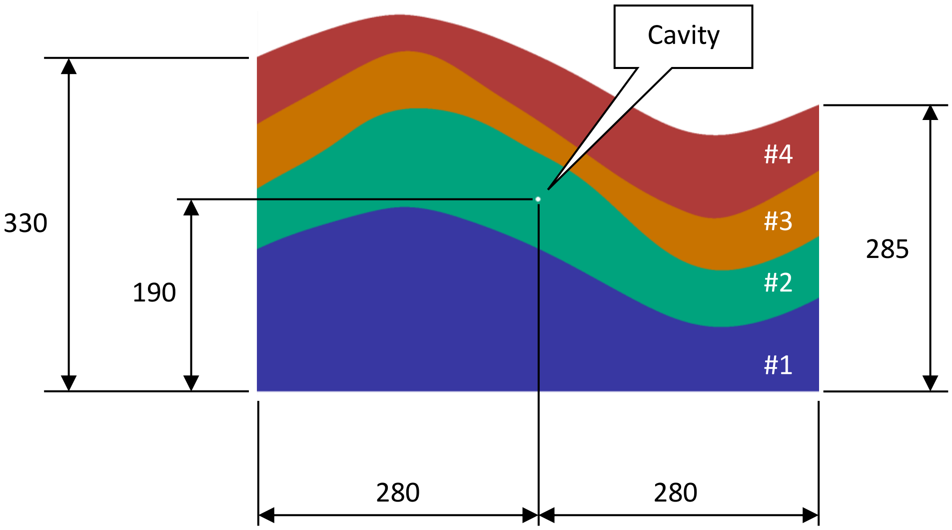

Figure 30. General description of the model of a representative geologic structure (all dimensions in meters). The radius of the cavity is 2.5 meters. Four different types of materials are included in the model.

The model consists of a section of a generic geological structure containing four different layers of different materials. For both the isotropic and the anisotropic cases, the material properties of each of the layers are listed in Table 3 and Table 4 respectively.

Table 3. Material properties for each layer of material shown in Figure 30. Isotropic case. All values in GPa.

Layer #	M_v	M_α	M_β	M_ψ
1	6.7	20.0	20.0	20.0
2	5.3	16.0	16.0	16.0
3	8.0	24.0	24.0	24.0
4	6.7	20.0	20.0	20.0

Table 4. Material properties for each layer of material shown in Figure 30. Anisotropic case. All values in GPa. See Figure 31-a.

Layer #	M_v	M_α	M_β	M_ψ
1	6.7	20.0	6.7	13.3
2	5.3	16.0	6.7	11.3
3	8.0	24.0	8.0	16.0
4	6.7	20.0	5.3	12.7

The cavity located inside of the layer of material #2 is subjected to a pressure boundary condition with a time history as shown in Figure 31-b. The sequence of the wave propagation for both types of mediums, i.e., anisotropic and isotropic are shown in Figure 32 and Figure 33. In the numerical results presented, the fractures are plotted in white while the wave propagation is colored according to the particle speed.

Figure 32 and Figure 33 clearly show the effects of the material descriptions on both the wave and fracture propagation. In the anisotropic case the shape of the wave propagation front is strongly affected by the orientation of the material axes, which further influences fracture initiation and propagation as well as the final patterns. This clearly demonstrates that modelers should always account for anisotropic material properties if the geophysical characterization shows that the substructure contains highly non-homogenous non-isotropic material. The above anisotropic deformation approach is one potential choice that can be utilized to handle these type of problems.

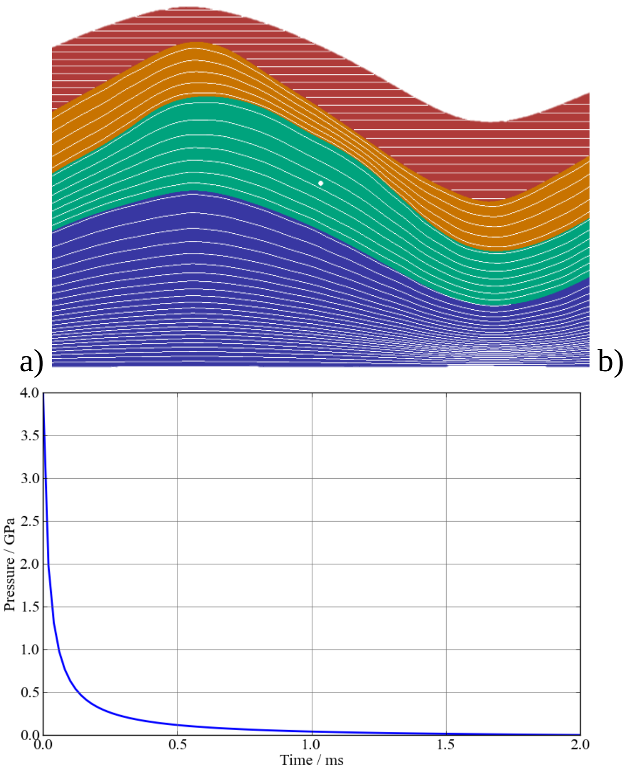

Figure 31. a) General description of the anisotropic model of a representative geologic structure. The white lines represent the direction of the material axis α with material axis β being perpendicular to α for the whole model, and b) Time history of the pressure pulse applied to the circular cavity.

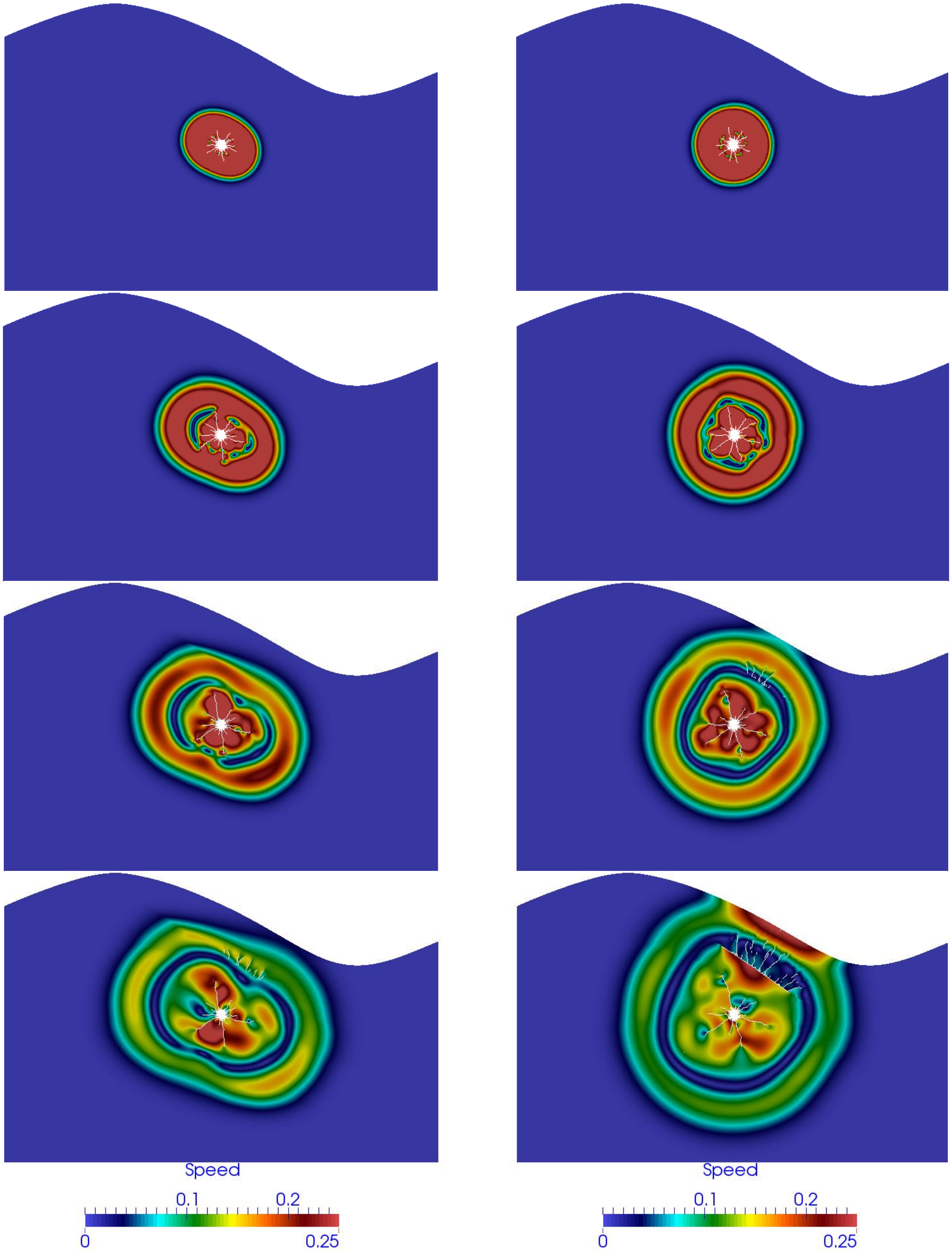

Figure 32. Comparison of the initial stages of the wave propagation through the geologic medium: Left: anisotropic material and Right: isotropic material.

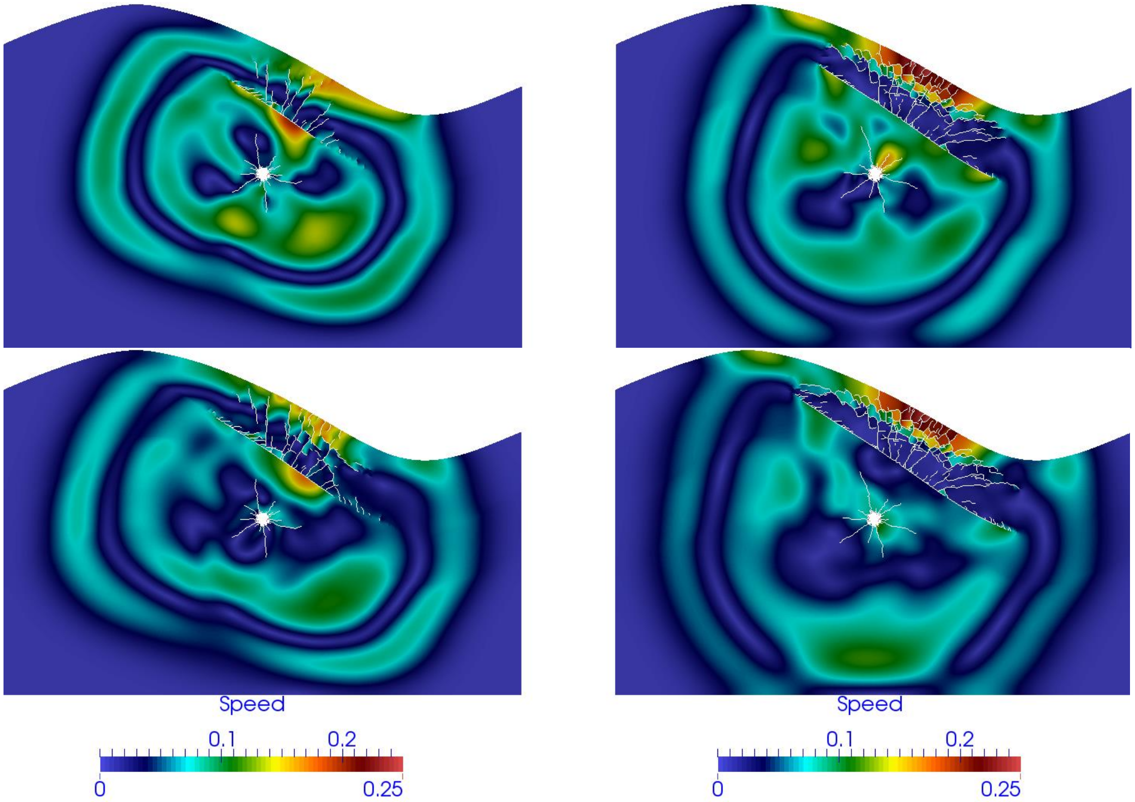

Figure 33. Comparison of the final stages of the wave propagation through the geologic medium: Left: anisotropic material and Right: isotropic material.

1.5 A Non-locking Composite Tetrahedron Element

TYPE: Peer Reviewed Paper

REFERENCE: A non-locking composite tetrahedron element for the combined finite discrete element method. Engineering Computations, 33:1929-1956, 2016. https://doi.org/10.1108/EC-09-2015-0268

AUTHORS: Z. Lei, E. Rougier, E.E. Knight, L. Frash, J.W. Carey, and H. Viswanathan

ABSTRACT: A ten-noded composite tetrahedral finite element which is composed of eight four-noded low order tetrahedrons has been implemented for the combined finite-discrete element method based on Munjiza's multiplicative decomposition approach. This approach naturally decomposes deformation into translation, rotation, plastic stretches, elastic stretches, volumetric stretches, shear stretches, etc. In order to avoid the problem of volumetric locking often encountered when using constant strain tetrahedral finite elements, a selective integration approach is employed which allows for different constitutive components to be evaluated at different integration points. A number of validation cases, considering different loading and boundary conditions and different materials, for the proposed composite finite element are presented. A practical application of the use of the composite tetrahedral finite element is presented by quantitative comparison of numerical model results against simple theoretical estimates and results from physical acrylic fracturing experiments**.**

PROBLEM DESCRIPTION:

Compressive load on opposite surface in both x and y directions

In this case a compressive load $p = 1000\ \mathrm{Pa}$ is applied on the opposite surfaces of a 1.0 m cube in both x and y directions as shown in Figure 34. The analytical expressions for the displacements at point A are given by:

$$\Delta x = -\frac{1-\nu}{\mathrm{E}} p \quad ; \quad \Delta y = -\frac{1-\nu}{\mathrm{E}} p \quad ; \quad \Delta z = \frac{2\nu}{\mathrm{E}} p \tag{16}$$

This calculated displacement is compared against the analytical displacement and the error in displacement is obtained:

$$e_{\Delta} = \frac{\left|\Delta - \underline{\Delta}\right|}{\Delta} \tag{17}$$

where $\Delta = \sqrt{\Delta x^2 + \Delta y^2 + \Delta z^2}$ and $\underline{\Delta} = \sqrt{\underline{\Delta} x^2 + \underline{\Delta} y^2 + \underline{\Delta} z^2}$ are the analytical and the numerical solutions respectively.

Four element sizes were used in conjunction with three different Poisson's ratios. The evolutions of the error in the displacement as a function of the element size for different values of Poisson ratios are shown in Figure 35. As can be observed from the figure, the error e_{Δ} nicely converges to zero as the element size is decreased, the convergence for the case with $\nu = 0.499$ being the fastest one.

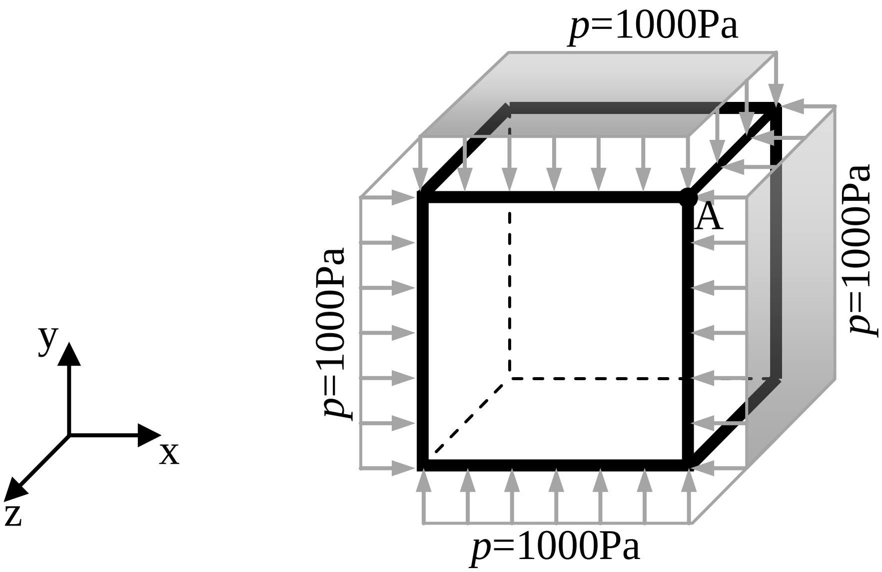

Figure 34. Model setup: a 1m cube loaded with compressive load on four surfaces.

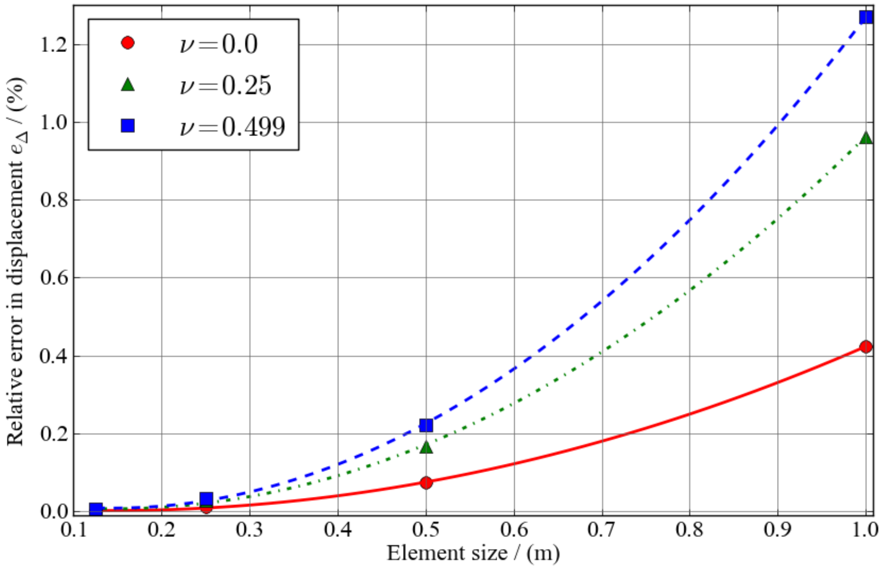

Figure 35. Relative error in displacement (e_{Δ}) as a function of element size – quadratic convergence with element size is observed.

Stress due to quadratic displacement field

In this case, the following quadratic displacement field is supplied to the 1m cube shown in Figure 36,

$$\begin{aligned} \tilde{x} &= \bar{x} + k_x \bar{x}^2 \\ \tilde{y} &= \bar{y} \\ \tilde{z} &= \bar{z} \end{aligned} \qquad (18)$$

where $(\tilde{x}, \tilde{y}, \tilde{z})$ and $(\bar{x}, \bar{y}, \bar{z})$ are the current and the initial coordinates of the nodes, and k_x is a constant parameter which is set to 1e-6.

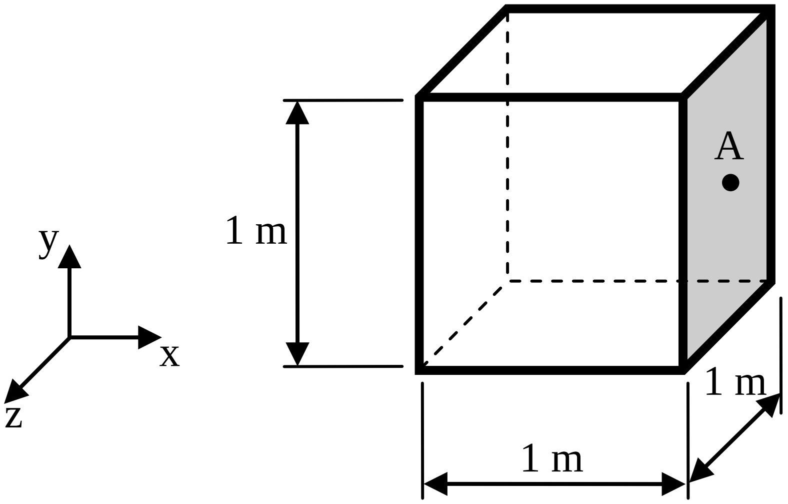

Figure 36. Model setup.

The analytical expression for the small strain formulation corresponding to the displacement field shown in equation (18) is given by

$$\begin{bmatrix} \varepsilon_x \\ \varepsilon_y \\ \varepsilon_z \end{bmatrix} = \begin{bmatrix} 2k_x\bar{x} \\ 0 \\ 0 \end{bmatrix} \tag{19}$$

where ε_x, ε_y, and ε_z are the strains in the x, y, and z directions respectively. These strains produce the following stresses

$$\begin{bmatrix} \sigma_x \\ \sigma_y \\ \sigma_z \end{bmatrix} = \frac{\mathrm{E}}{(1+\nu)(1-2\nu)} \begin{bmatrix} (1-\nu) & \nu & \nu \\ \nu & (1-\nu) & \nu \\ \nu & \nu & (1-\nu) \end{bmatrix} \begin{bmatrix} \varepsilon_x \\ \varepsilon_y \\ \varepsilon_z \end{bmatrix} \tag{20}$$

where E and ν are the Young's module and the Poisson's ratio respectively.

The stresses obtained from the numerical calculations are compared against the analytical stresses and for each Cartesian direction the error in stress is obtained by

$$e_\sigma = \frac{|\sigma - \underline{\sigma}|}{\sigma} \tag{21}$$

where σ and $\underline{\sigma}$ are the values of the stress obtained analytically and numerically.

The material used in this case had a Young's modulus $\mathrm{E} = 1.0\mathrm{e}9$ and a Poisson's ratio $\nu = 0.0$. Different mesh sizes were used in order to study the convergence rate of the ten-noded COMPTet formulation. The four coarsest meshes used in this analysis are shown in Figure 37 while the results obtained are shown in Figure 38, from where it can be concluded that for the quadratic displacement field, the convergence rate in stress is linear, with respect to the element size.

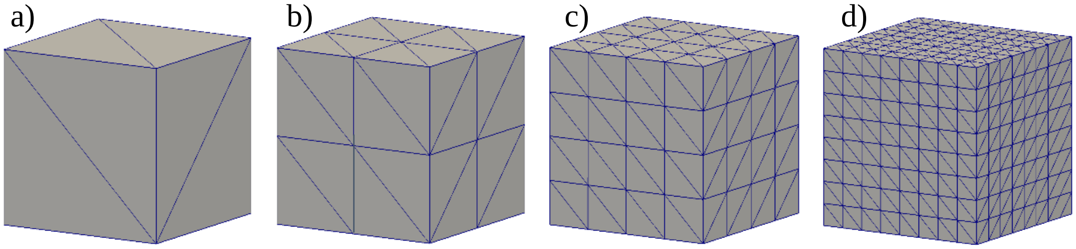

Figure 37. Different meshes used: a) 1.0 m, b) 0.5 m, c) 0.25 m and d) 0.125 m.

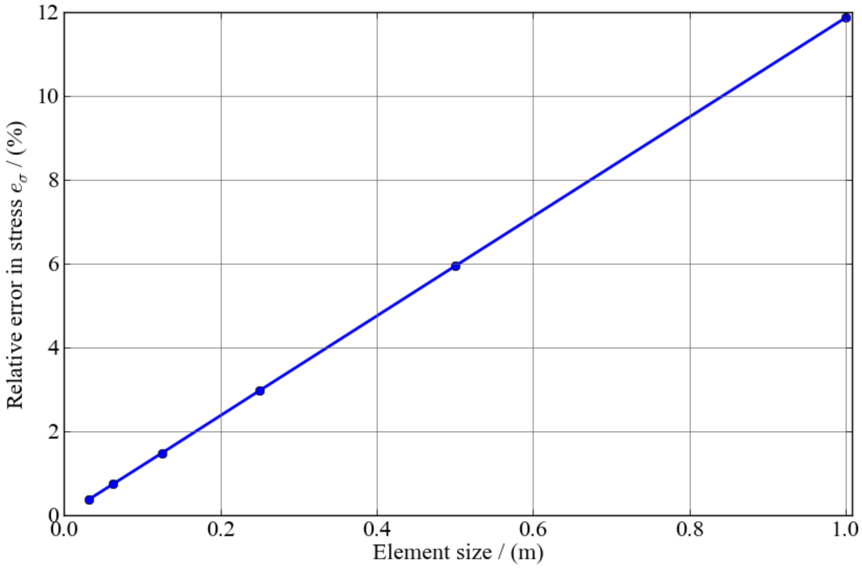

Figure 38. Relative error in stress (e_σ) as a function of element size – Linear convergence with element size is observed.

Tests for Volumetric Locking

In this section the behaviour of the composite element COMPTet in nearly incompressible conditions is demonstrated. Comparisons between the results obtained with COMPTet and with CSTet are also presented.

A 1.0 m cube with its back-, left- and bottom-faces fixed (shaded faces shown in Figure 39) is one of the cases used to test the volumetric locking behaviour of the composite element formulation. A force

$$\mathbf{f} = \begin{bmatrix} f_x \\ f_y \\ f_z \end{bmatrix} = 1.0\text{e}6 \begin{bmatrix} 1 \\ 1 \\ 1 \end{bmatrix} \text{N} \tag{22}$$

is applied at point A of a cube, as shown in Figure 39. The obtained results for the stress maps are shown in Figure 40 and in Figure 41. The stress distribution obtained for the CSTet (Figure 40-b and -d) shows clear signs of volumetric locking behaviour, evidenced by a quite marked checkerboard pattern and large values of stresses near the point of application of the force. The COMPTet does not suffer from these ailments, as is shown in Figure 40-a and -c, i.e., the stress distribution is smooth without checkerboard patterns and the values of the stresses are not excessively large close to the point where the force is applied.

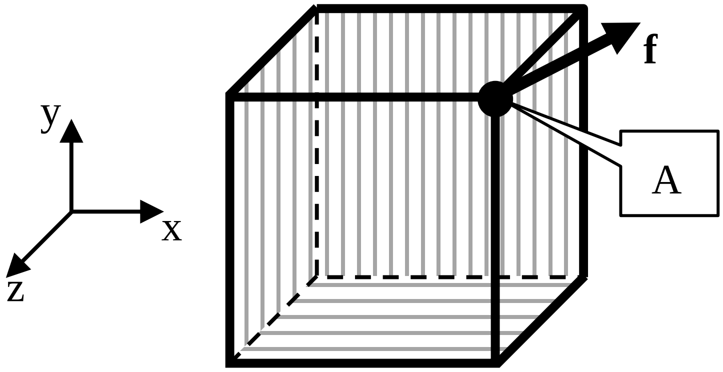

Figure 39. Model setup: 1m cube loaded with a concentrated load at point A.

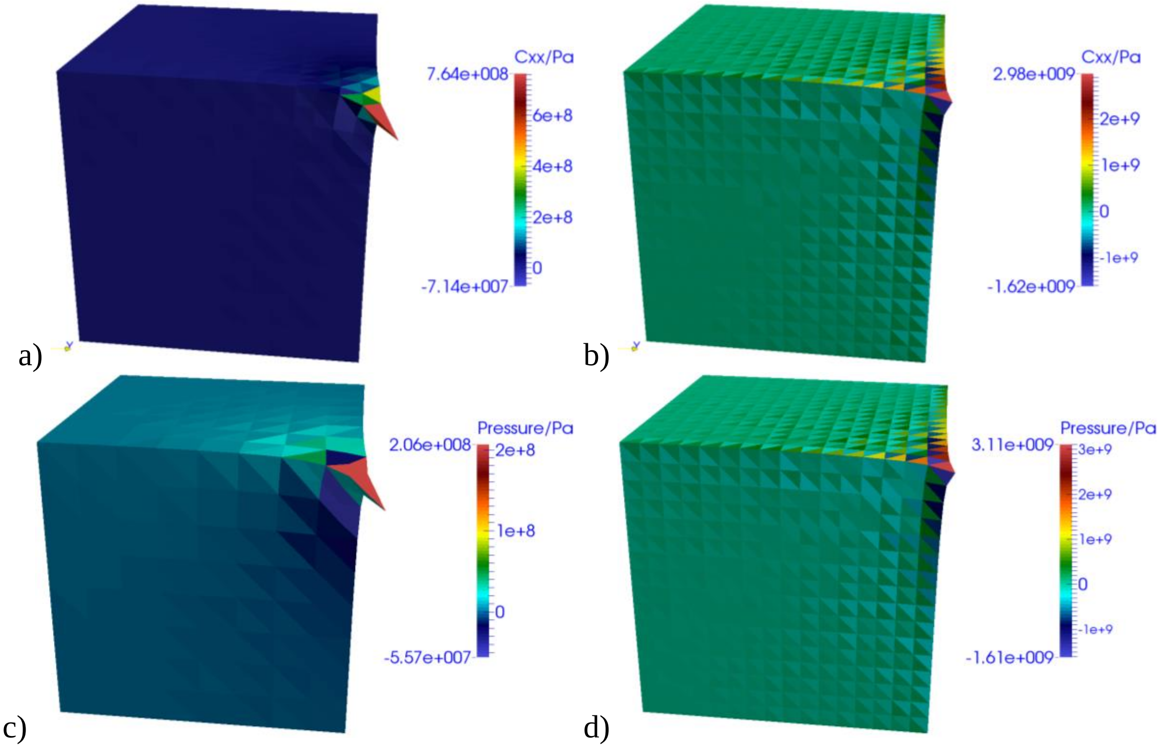

a)

b)

c)

d)

Figure 40. Stress distribution: a) σ_x for the composite element, b) σ_x for the constant strain element, c) Munjiza pressure for the composite element and d) Munjiza pressure for the constant strain element (ν=0.499).

Other evidence that the derived composite element formulation does not exhibit volumetric locking problems is given by Figure 41, where the magnitude of the displacements is plotted on top of the un-deformed mesh for both cases. Due to the volumetric locking effects, a very small displacement is observed for the case of the CSTet (in the order of 0.05 m), while for the case of the COMPTet a much larger displacement is obtained (in the order of 0.18 m).

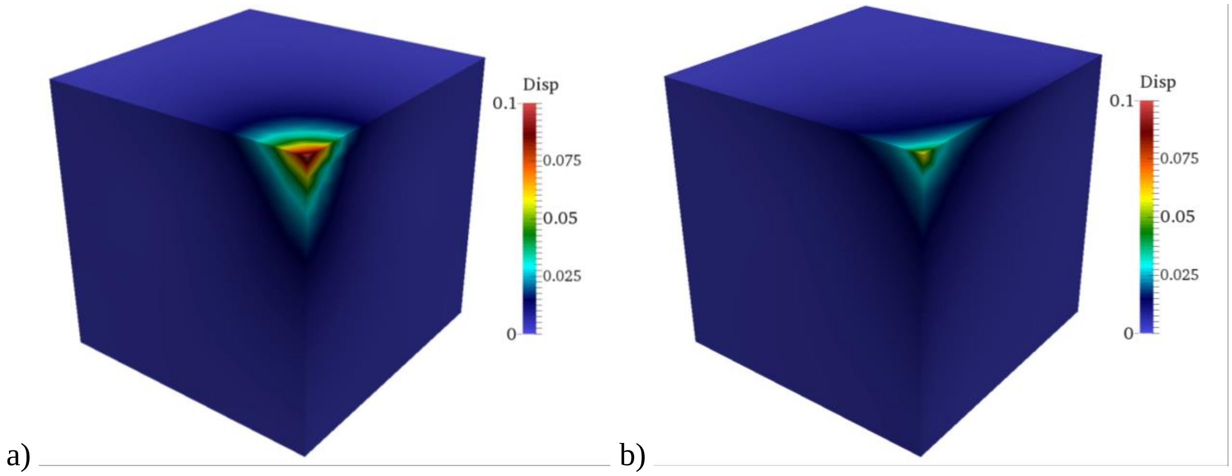

a) b)

Figure 41. Displacement distribution on undeformed mesh: a) composite element and b) constant strain element (ν=0.499).

The second example that was utilized to test the volumetric locking behaviour is shown in Figure 42, where an infinite plate with a circular hole of radius $a = 0.1\,\mathrm{m}$ in the middle is subjected to tensile stresses at its ends in plane strain.

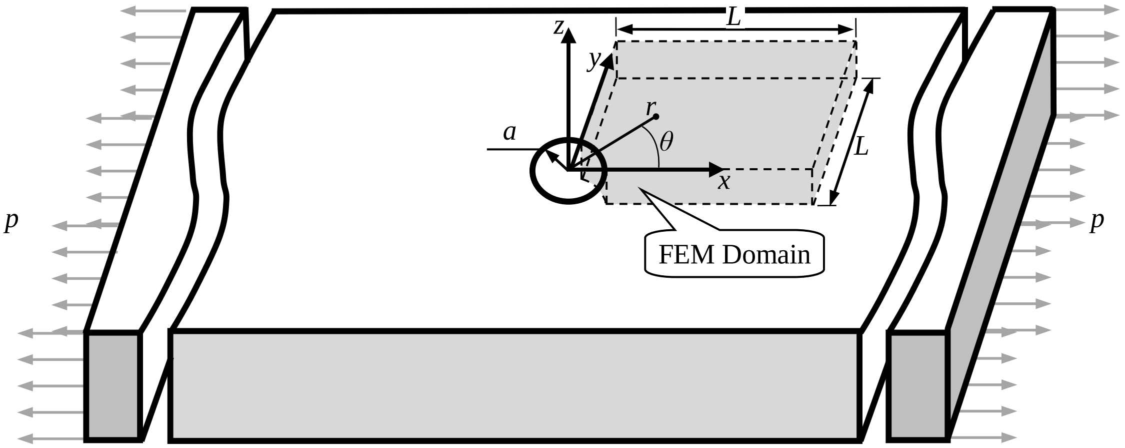

Figure 42. Infinite plate with a circular hole.

The analytical solution for the radial and tangential displacements is given by (Timoshenko and Goodier, 1970)

$$\begin{aligned}\Delta_r &= \frac{p(1+\nu)}{2E}\left[\frac{1-\bar{\nu}}{1+\bar{\nu}}r + \frac{a^2}{r} + \left(r - \frac{a^4}{r^3} + \frac{4a^2}{(1+\bar{\nu})r}\right)\cos 2\theta\right] \\ \Delta_\theta &= -\frac{p(1+\nu)}{2E}\left(r + \frac{a^4}{r^3} + \frac{2(1-\bar{\nu})a^2}{(1+\bar{\nu})r}\right)\sin 2\theta\end{aligned} \tag{23}$$

The displacements in the global coordinate system are given by:

$$\begin{bmatrix}\Delta_x \\ \Delta_y\end{bmatrix} = \begin{bmatrix}\cos\theta & -\sin\theta \\ \sin\theta & \cos\theta\end{bmatrix}\begin{bmatrix}\Delta_r \\ \Delta_\theta\end{bmatrix} \tag{24}$$

Due to the symmetry of the problem, only one quadrant was simulated. A finite analysis domain in x-y plane of size 1.0 (10*a*) is taken from the infinite plate (see Figure 42). The exact analytical displacements calculated from equation (23) are applied to the nodes on the remote sides of the analysis domain. The nodes of the finite element mesh that are on the other sides of the plate are allowed to move only in the x-z plane, while the nodes that are on the top and bottom faces of the plate are allowed to move only in the x-y plane. The material properties used for this case are Young's modulus $\mathrm{E} = 30\,\mathrm{MPa}$ and Poisson's ratio $\nu = 0.25, 0.4999$. This latter value of the Poisson's ration ($\nu = 0.4999$) tests the performance of the proposed COMPTet in a near-incompressible conditions. Four different mesh sizes (see Figure 43) were used in order to verify the convergence of the results with the decreasing element size.

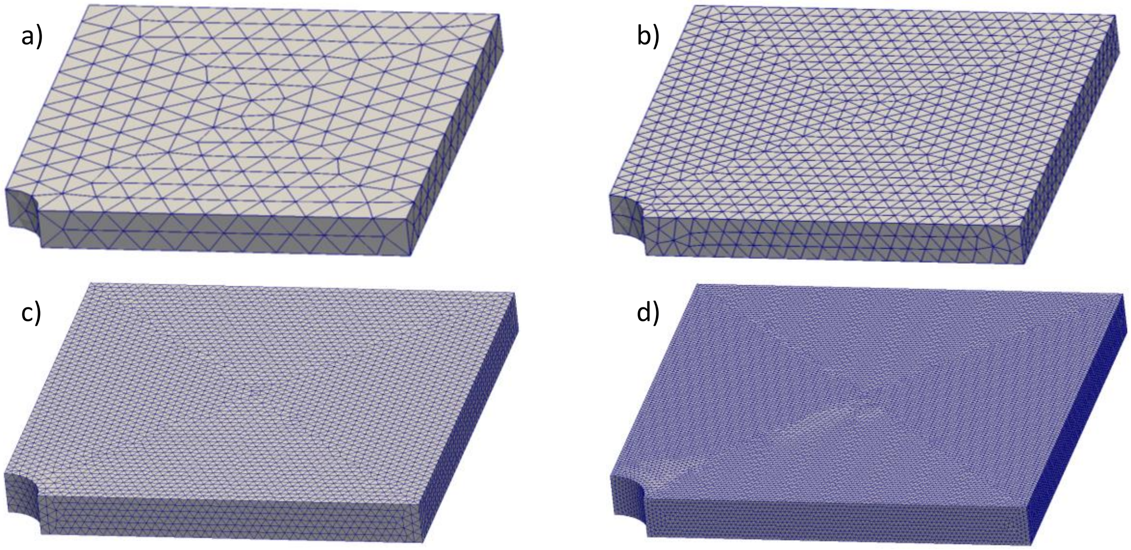

Figure 43. Finite element model: a) mesh size *h*/*L* = 1/12, b) mesh size *h*/*L* = 1/24, c) mesh size *h*/*L* = 1/48, d) mesh size *h*/*L* = 1/96.

The relative error (based on the displacement field) of the numerical results when compared against the analytical ones is calculated as follows

$$e = \frac{\left|\Delta - \underline{\Delta}\right|}{\Delta} \tag{25}$$

where $\Delta = \int \sqrt{\Delta x^2 + \Delta y^2 + \Delta z^2}\,\mathrm{d}\Omega$ and $\underline{\Delta} = \int \sqrt{\underline{\Delta} x^2 + \underline{\Delta} y^2 + \underline{\Delta} z^2}\,\mathrm{d}\Omega$ are the sum of all the displacements over the domain for the analytical and the numerical solutions respectively. The evolution of the error with the element size is shown in Figure 44. Again, this composite element formulation clearly shows its capability in eliminating volumetric locking.

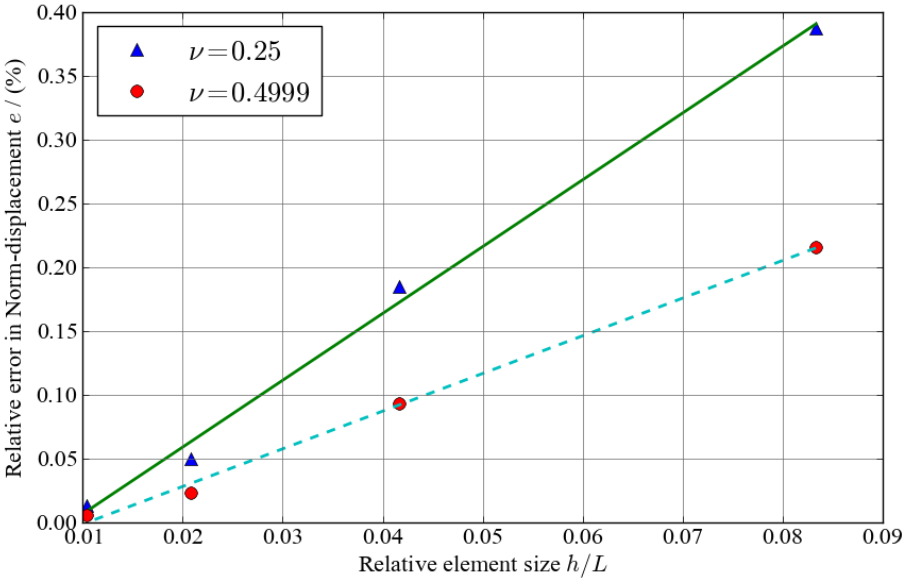

Figure 44. Relative error in Norm-displacement as a function of element size – Linear convergence with element size is observed.

Practical Application

Early analysis results for a Los Alamos National Laboratory directed research program experiment (Frash et al., 2015) utilized a FDEM CSTet element to estimate the stress state at the bottom of a notch manufactured inside of an acrylic cylindrical sample. The low order element's limitations were evident, as it is demonstrated by the stress checkerboard pattern observed in Figure 45. These limitations were due to volumetric locking problems inherent to the CSTet formulation for the particular conditions being tested. As is demonstrated in the rest of this section, the composite tetrahedral element (COMPTet) simulation results show remarkable improvement on the stress field and on the convergence with decreasing element size over the CSTet results. The numerical results obtained with the COMPTet are also compared against experimental results.

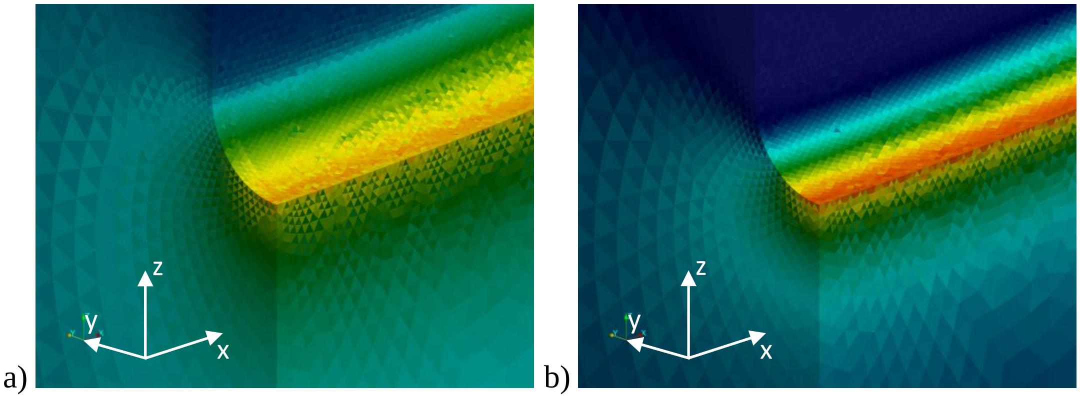

Figure 45. Checkerboard problems encountered with the constant strain tetrahedron: a) map of C_{xx}. b) map of C_{yy}.

The geometry of the notched samples under consideration is shown in Figure 46. Two different models were taken into account: Model 1 contains a smaller notch with a radius of 5.0 mm, a depth of 3.81 mm and aperture of 0.15 mm, while Model 2 contains a larger notch which radius, depth and aperture are 11.0 mm, 9.4 mm and 0.17 mm respectively (Figure 46).

These notched samples contain a novel geometry that was utilized in hydrofracture experiments under triaxial stress conditions. As such, the samples were subjected to three different stress fields (or loading cases) (Frash et al., 2015): 1) an axial confining stress (p_1), 2) a lateral confining stress (p_2) and 3) a notch opening stress (p_3).

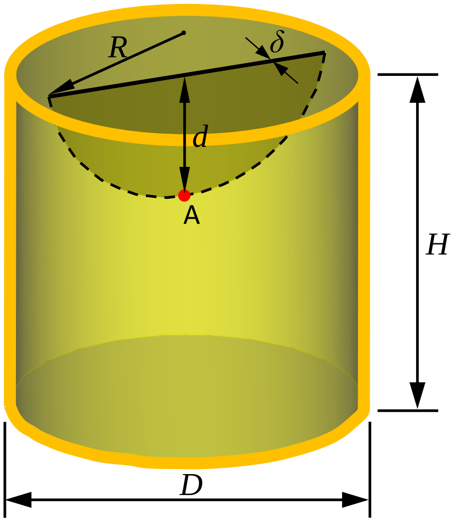

Figure 46. Geometry of the sample. D and H are the diameter and the height of the sample, R, d and δ are the radius, the depth and the aperture of the notch respectively. $D = H = 25.4\,\text{mm}$. Model 1: $R = 5.0\,\text{mm}$, $d = 3.81\,\text{mm}$, $\delta = 0.15\,\text{mm}$; Model 2: $R = 11.0\,\text{mm}$, $d = 9.4\,\text{mm}$, $\delta = 0.17\,\text{mm}$.

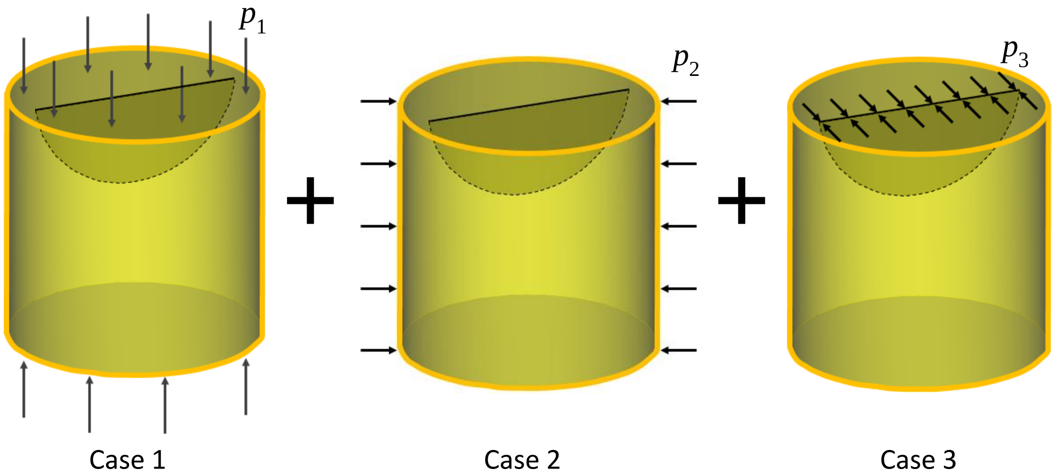

Figure 47. The general loading of the sample can be obtained as the sum of individual loading cases: Case 1: axial load, Case 2: confining pressure load, Case 3: pressure in the notch load.

For the purpose of the estimation of the stress state at the bottom of the notch (point A in Figure 46) as a function of the stress fields, it is assumed that the material behaves as a linearly elastic medium. Therefore, the stress state at point A can be determined by superimposing the stress states due to the three stress fields described before. Because of this, the three different loading cases were considered: Case 1: axial load with a pressure p_1, Case 2: confining load with a pressure p_2, and Case 3: notch opening load with a pressure p_3 (see Figure 47). In this way, the stresses at point A are given by,

$$\begin{aligned} \sigma_{xx}^{\mathrm{A}} &= c_{1xx} p_1 + c_{2xx} p_2 + c_{3xx} p_3 \\ \sigma_{yy}^{\mathrm{A}} &= c_{1yy} p_1 - c_{2yy} p_2 + c_{3yy} p_3 \end{aligned} \tag{26}$$

where c_{1xx}, c_{2xx}, and c_{3xx} are the contributions of the stress fields p_1, p_2, and p_3 to the stress σ_{xx}^{A} at point A. In a similar way, c_{1yy}, c_{2yy}, and c_{3yy} are the contributions of the stress fields p_1, p_2, and p_3 to the stress σ_{yy}^{A} at point A. Since the material is assumed elastic, the loads for each one of the stress fields can be set to unity and the coefficients shown in equation (26) can be determined, which allows for the estimation of the stress state at point A for any general combination of p_1, p_2, and p_3. The material of the sample is acrylic with the following properties: Young's modulus $\mathrm{E} = 3.3\ \mathrm{GPa}$, Poisson's ratio $\nu = 0.38$ and density $\rho = 1200\ \mathrm{kg/m^3}$.

Model 1: The dimensions for this model are shown in Figure 46. In order to verify the convergence of the stress values at the bottom of the notch with decreasing element sizes three different mesh sizes (see Figure 48) were tested.

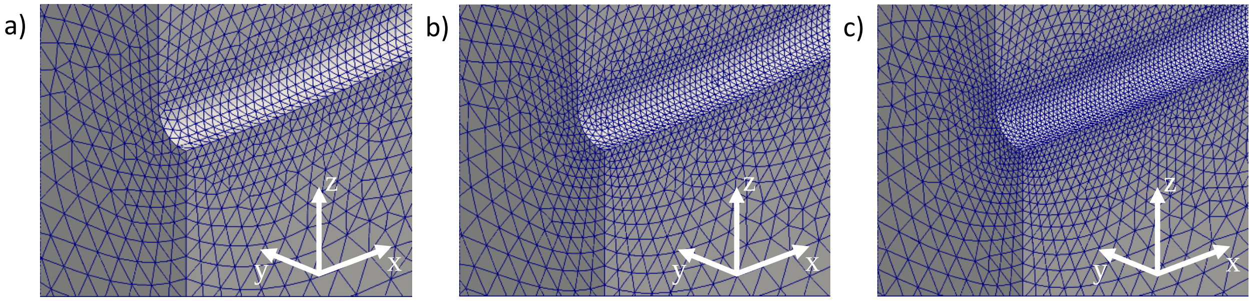

Figure 48. Details of the finite element discretization at the bottom of the notch: a) L1 – mesh size 0.3*r*, b) L2 – mesh size 0.2*r*, c) L3 – mesh size 0.15*r*; where *r* is the radius of the notch (see Figure 46).

The values of the stresses in the x and y directions for the three cases analyzed are listed in Table 5. For all the cases, the results obtained with the finest mesh were taken as a reference. From the table it can be seen that, as the element size decreases, the difference in the numerical results is smaller (in the order of a couple of percentage points).

Table 5. Results for cases 1, 2 and 3 in model 1.

	Mesh	C_{xx} /MPa	error	C_{yy} /MPa	error
Case 1	L1	0.61	5.7%	0.65	13.5%
	L2	0.66	1.5%	0.72	4.5%
	L3	0.65	Ref.	0.75	Ref.
Case 2	L1	-4.94	1.6%	-10.7	5.3%
	L2	-4.99	0.6%	-11.0	2.7%
	L3	-5.02	Ref.	-11.3	Ref.
Case 3	L1	3.25	2.2%	8.99	4.4%
	L2	3.27	2.8%	9.23	1.8%
	L3	3.18	Ref.	9.40	Ref.

Therefore, the stresses at point A for this case are given by,

$$\begin{aligned} C_{xx}^{\mathrm{A-1}} &= 0.65 p_1 - 5.02 p_2 + 3.18 p_3 \\ C_{yy}^{\mathrm{A-1}} &= 0.75 p_1 - 11.30 p_2 + 9.40 p_3 \end{aligned} \tag{27}$$

It is worth noting that Frash et al. (Frash et al., 2015) also obtained an estimate of the stress values at the bottom of the notch by making a number of simplifying assumptions regarding the geometry of the sample and by considering that the material behaved elastically. Their results for the stresses at point A (see Figure 46) are given by

$$C_{yy}^{t} = 1.00\ p_1 - \left(1 + 2\sqrt{2d/\delta}\right) p_2 - \left(1 - 2\sqrt{2d/\delta}\right) p_3 \tag{28}$$

where d is the notch depth and δ is the aperture of the notch. For this particular sample geometry $2d/\delta = 50.8$, therefore, the stress values at the bottom of the notch according to Frash et al. (Frash et al., 2015) are given by

$$C_{yy}^{t-1} = 1.00\,p_1 - 15.25\,p_2 + 13.25\,p_3 \tag{29}$$

The coefficients for p_1, p_2, and p_3 obtained from the theoretical approximation are in quite good agreement with the ones obtained from the finite element analysis. This is because both approaches use similar assumptions regarding the material behaviour (elastic). It is known that, as the material around point A approaches the breaking point (fracture initiation) plastic deformations can occur. This will be addressed in future work by the finite element analysis team via the incorporation of the appropriate plasticity material model.

For illustration purposes, the stress fields for all three cases are shown in Figure 49 thru Figure 51. In this case, the map of stresses obtained with the COMPTet is very smooth, without any sign of checkerboard pattern issues.

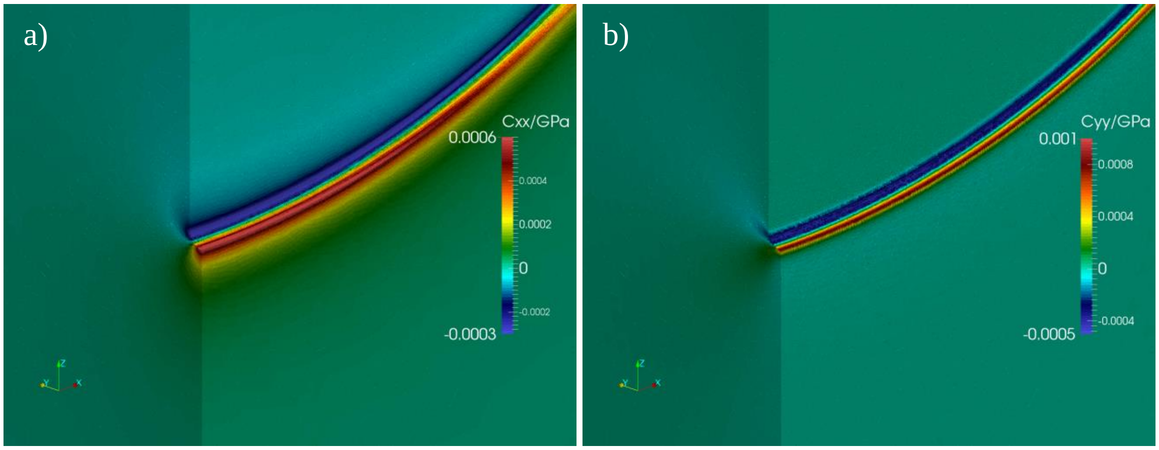

Figure 49. Case 1 – Mesh L3 – a) detail of Cauchy stress C_{xx}, b) detail of the Cauchy stress C_{yy}.

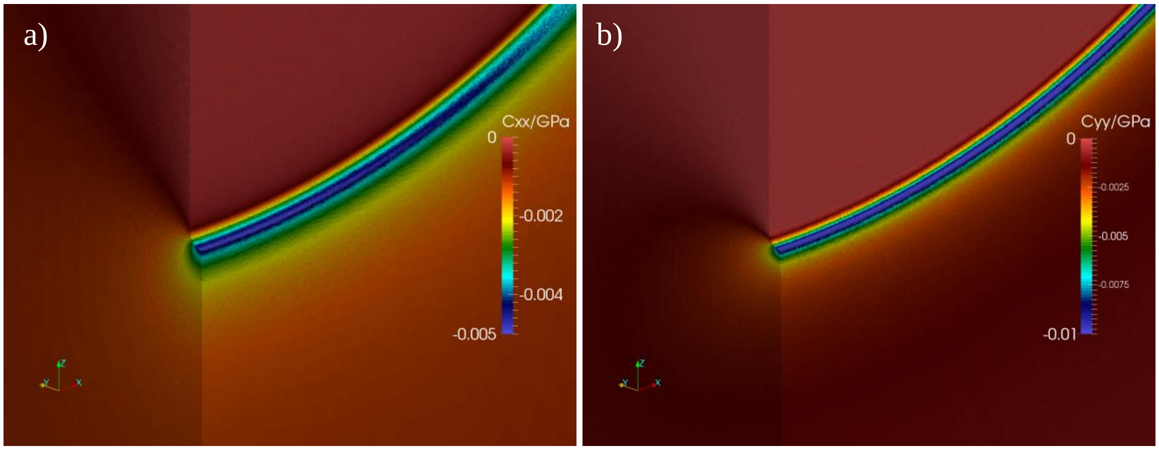

Figure 50. Case 2 – Mesh L3 – a) detail of Cauchy stress C_{xx}, b) detail of the Cauchy stress C_{yy}.

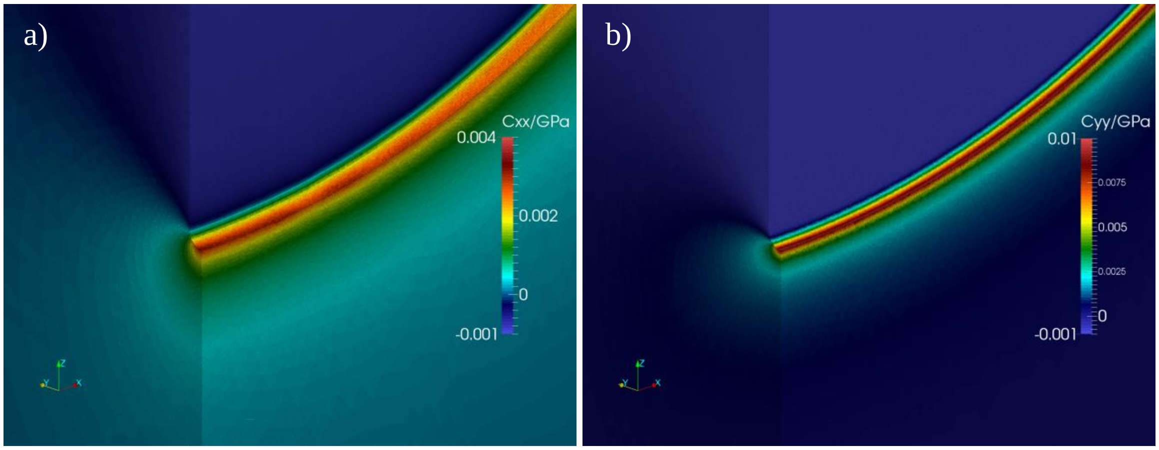

Figure 51. Case 3 – Mesh L3 – a) detail of Cauchy stress C_{xx}, b) detail of the Cauchy stress C_{yy}.

Model 2: The dimensions for this model are shown in Figure 46. In order to verify the convergence of the stress values at the bottom of the notch with decreasing element sizes three different mesh sizes (see Figure 52) were tested.

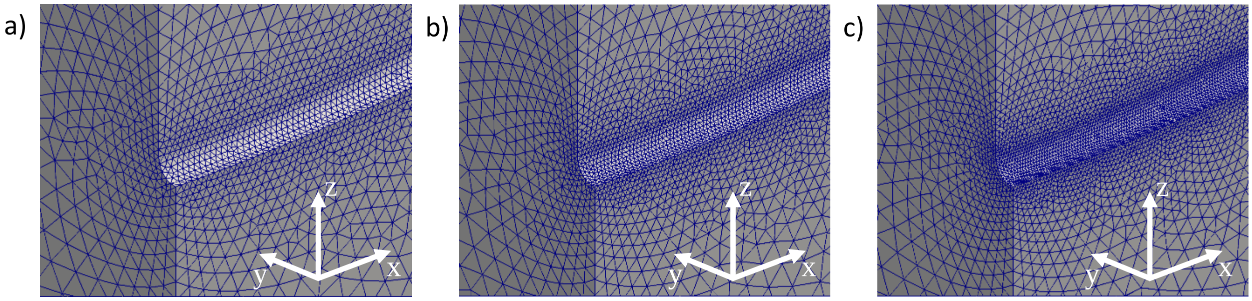

Figure 52. Details of the finite element discretization at the bottom of the notch: a) L1 – mesh size 0.3*r*, b) L2 – mesh size 0.2*r*, c) L3 – mesh size 0.15*r*; where *r* is the radius of the notch (see Figure 46).

The values of the stresses in the x and y directions for the three cases analyzed are listed in Table 6. For all the cases, the results obtained with the finest mesh were taken as a reference. Again, from the table it can be seen that, as the element size decreases, the difference in the numerical results is smaller (in the order of a couple of percentage points).

Table 6. Results for cases 1, 2 and 3 in model 2.

	Mesh	C_{xx} /MPa	error	C_{yy} /MPa	error
Case 1	L1	0.69	4.0%	0.85	6.7%
	L2	0.70	1.9%	0.88	2.7%
	L3	0.72	Ref.	0.91	Ref.
Case 2	L1	-9.37	1.1%	-24.3	2.0%
	L2	-9.67	2.1%	-24.5	1.2%
	L3	-9.47	Ref.	-24.8	Ref.
Case 3	L1	7.58	1.2%	22.4	2.2%
	L2	7.86	2.4%	22.6	1.3%
	L3	7.67	Ref.	22.9	Ref.

Therefore, the stresses at the bottom of the notch are then given by,

$$\begin{aligned} C_{xx}^{\mathrm{A}-2} &= 0.72\,p_1 - 9.47\,p_2 + 7.67\,p_3 \\ C_{yy}^{\mathrm{A}-2} &= 0.91\,p_1 - 24.8\,p_2 + 22.9\,p_3 \end{aligned} \tag{30}$$

while, the stress values at the bottom of the notch according to Frash et al. are given by

$$C_{yy}^{t-2} = 1.00\,p_1 - 22.0\,p_2 + 20.0\,p_3 \tag{31}$$

Again, the coefficients for p_1, p_2, and p_3 obtained from the theoretical approximation are in quite good agreement with the ones obtained from the finite element analysis.

For illustration purposes, the stress fields for all three cases are shown in Figure 53 thru Figure 55. In this case, the map of stresses is very smooth, without any sign of checkerboard pattern issues.

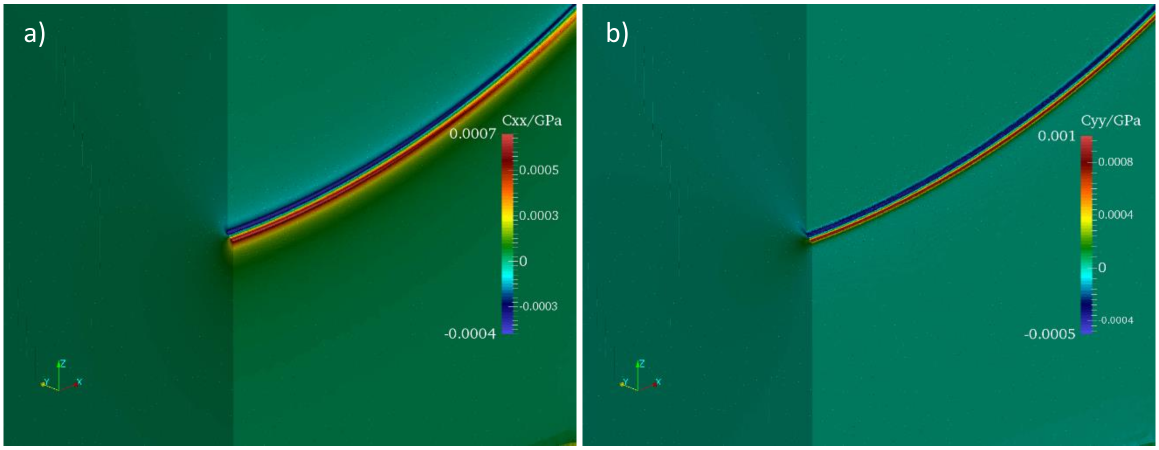

Figure 53. Case 1 – Mesh L3 – a) detail of Cauchy stress C_{xx}, b) detail of the Cauchy stress C_{yy}.

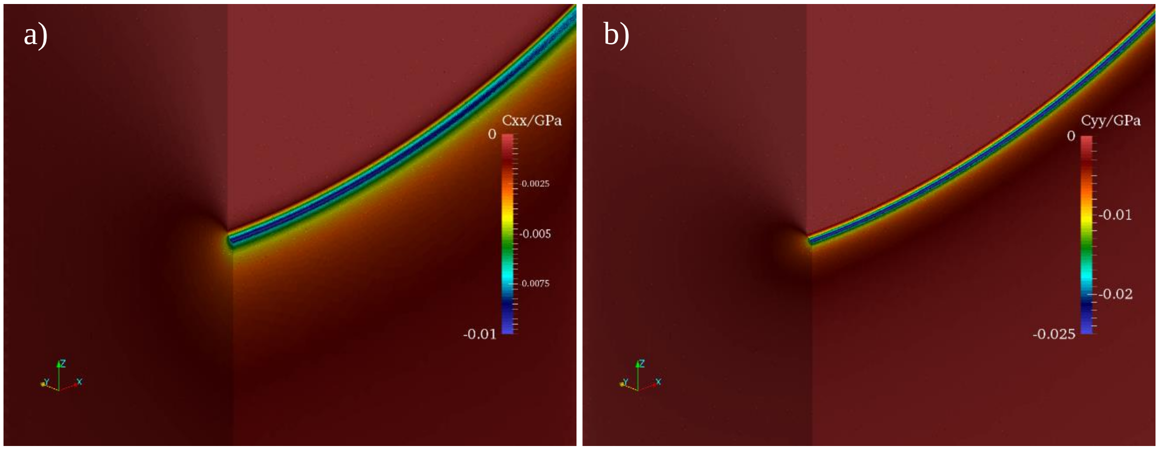

Figure 54. Case 2 – Mesh L3 – a) detail of Cauchy stress C_{xx}, b) detail of the Cauchy stress C_{yy}.

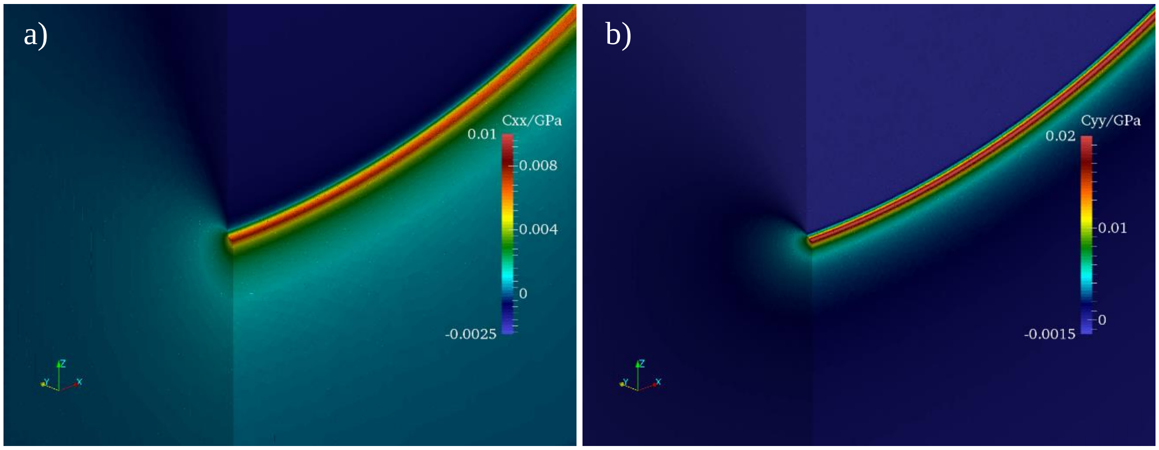

Figure 55. Case 3 – Mesh L3 – a) detail of Cauchy stress C_{xx}, b) detail of the Cauchy stress C_{yy}.

Experimental Results: Physical samples of acrylic cut to the dimensions of Models 1 and 2 were fractured under triaxial stress conditions with hydraulic pressure inside the notches (Frash et al., 2015). The stress fields at fracture initiation were recorded for each experiment giving the results shown in Table 7. Substituting these stress fields into equations (27), (29), (30) and (31) gives estimates of C_{yy} at fracture initiation for each respective model, representing the estimated notch tensile strength of the acrylic (Table 3). The bulk tensile yield strength of acrylic measured by conventional means is in the range of 56 to 76 MPa (McMaster-Carr Supply Company, 2015). The error in tensile strength estimation using the numerical approach was less than that of the theoretical approach (Frash et al., 2015). These results emphasize the importance of incorporating plasticity in future work to more accurately model fracturing processes.

Table 7. Experimental fracture initiation stress fields for Models 1 and 2.

Model	p_1 (MPa)	p_2 (MPa)	p_3 (MPa)	C_{yy}^{A} (MPa)	C_{yy}^{t} (MPa)
Model 1 – L3	28	2	12.5	298	414
Model 2 – L3	116	2	24.8	263	235

2 Fracture

2.1 Split Hopkinson Pressure Bar (SHPB) Brazilian Experiment

TYPE: Peer Reviewed Paper

REFERENCE: Validation of a three-dimensional Finite-Discrete Element Method using experimental results of the Split Hopkinson Pressure Bar test. International Journal of Rock Mechanics and Mining Sciences, 70:101-108, 2014. https://doi.org/10.1016/j.ijrmms.2014.03.011

AUTHORS: E. Rougier, E.E. Knight, S.T. Broome, A.J. Sussman and A. Munjiza

ABSTRACT: Transient dynamics of fracturing media has received significant attention in recent years and a number of simulation approaches have been developed. One of these is the combined finite-discrete element method (FDEM). FDEM produces complex fracture and fragmentation patterns in processes such as blast loads, blasting, impact, mining and oil exploration. LANL has an in-house FDEM software package called HOSS (Hybrid Optimization Software Suite). HOSS is a state-of-the-art 2D/3D FDEM package incorporating sophisticated contact interaction, contact detection, parallelization, fracture, deformability and material models. Presented here is a full-scale 3D analysis of a SHPB experiment on granite material with a reproduction of the softening behavior after sample breakage.

PROBLEM DESCRIPTION: Pictorially, we display the setup and experimental waves in Figure 56.

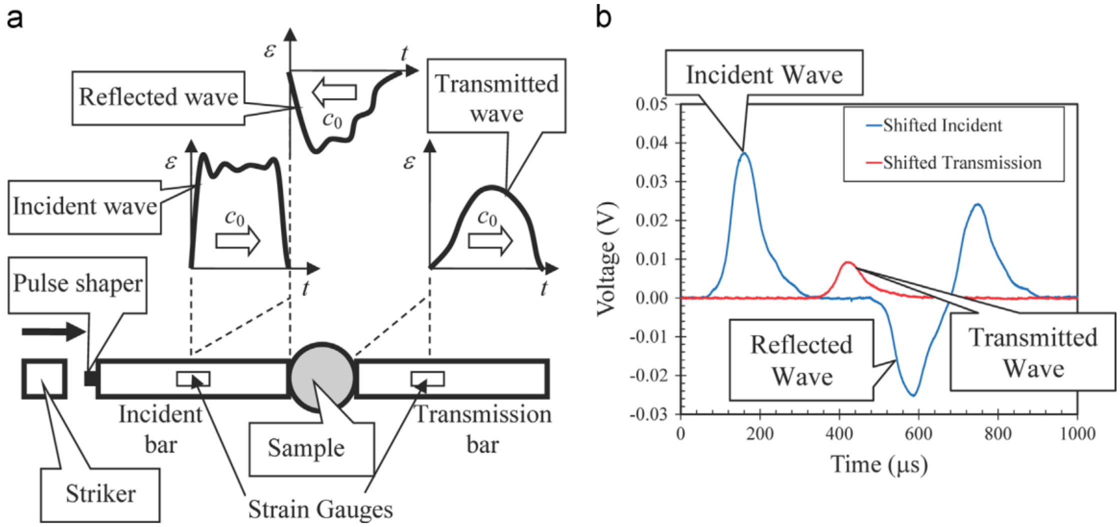

Figure 56. (a) Setup of the SHPB experiment and (b) incident, reflected and transmitted waves taken from the experiment.

The incident and the transmission bars are supported to avoid any lateral movement and to allow only longitudinal movement. Because of this, the stress state in these bars can be described by the one dimensional wave equation. The displacement as a function of time for a given point along the bars is given by

$$u = c_0 \int_0^t \varepsilon \, dt \tag{32}$$

Where ε is the strain in the bar and c_0 is the elastic wave speed in the bar given by

$$c_0 = \sqrt{\frac{E}{\rho}} \tag{33}$$

while E is the Young modulus and ρ is the density.

Due to the fact that the incident and reflected waves travel in opposite directions, the displacement at the interface between the incident bar and the sample is obtained as a combination of the effects of these two waves, as follows

$$\begin{aligned} u_1 &= c_0 \int_0^t \varepsilon_i \, dt - c_0 \int_0^t \varepsilon_r \, dt \\ &= c_0 \int_0^t \left(\varepsilon_i - \varepsilon_r \right) dt \end{aligned} \tag{34}$$

Where ε_i and ε_r are the strains due to the incident and reflected waves respectively. On the other hand, the displacement at the interface between the sample and the transmission bar is solely dictated by the transmitted wave, as follows

$$u_2 = c_0 \int_0^t \varepsilon_t \, dt \tag{35}$$

where ε_t is the strain due to the transmitted wave. Following this line of reasoning, the contact surface between the incident bar and the sample moves at velocity v_1, which is given by

$$v_1 = \frac{\partial u_1}{\partial t} = c_0 \left(\varepsilon_i - \varepsilon_r \right) \tag{36}$$

while the contact surface between the sample and the transmission bar moves at velocity v2, which is given by

$$v_2 = \frac{\partial u_2}{\partial t} = c_0 \varepsilon_t \tag{37}$$

The material properties used to describe the material of the bars (Titanium Ti–6Al–4V) are E_b = 113.8GPa, ν_b = 0:32 and ρ_b = 4540 kg/m3, where E_b is Young's modulus, ν_b is Poisson's ratio, and ρ_b is the density. The interaction between the bars and the granite sample was modeled using the standard FDEM contact approach with a Coulomb coefficient of friction of 0.1. The elastic properties of the granitic material are E_s = 35:0 GPa, ν_s = 0:16 and ρ_s = 2550 kg/m3. Also, the following fracture-related material properties for the rock were supplied to the model: s_t = 4:0 MPa, s_s = 31:0 MPa, δ_c = 0:12 mm and μ = 0:6, where s_t and s_s are the tensile and shear strength respectively, δ_c is the maximum fracture aperture, and μ is the internal friction coefficient. Additionally, the strain softening curve utilized is shown in Figure 57. The model setup utilized is shown in Figure 58.

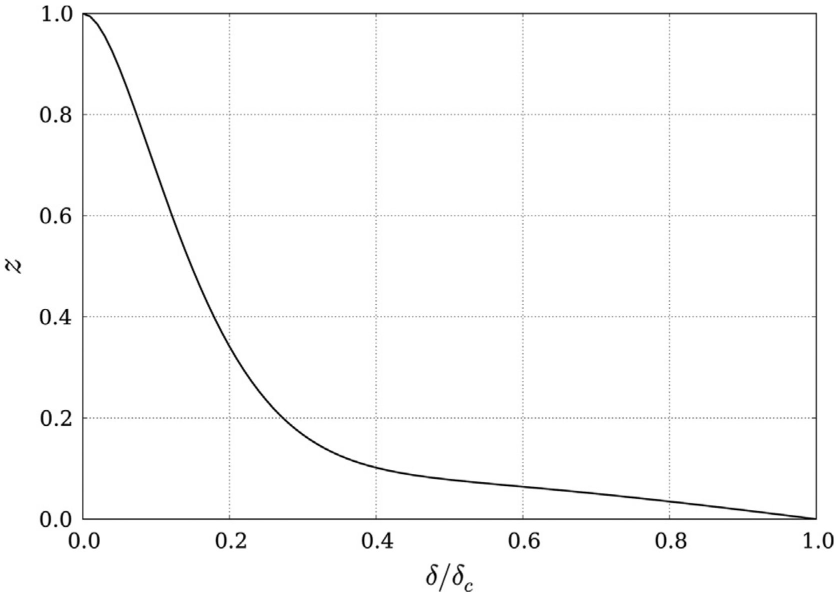

Figure 57. Strain softening curve for granite. The parameter z defines the post-peak strain softening behavior for the material, as a function of the ratio between the current fracture opening δ and the maximum allowable fracture opening δ_c.

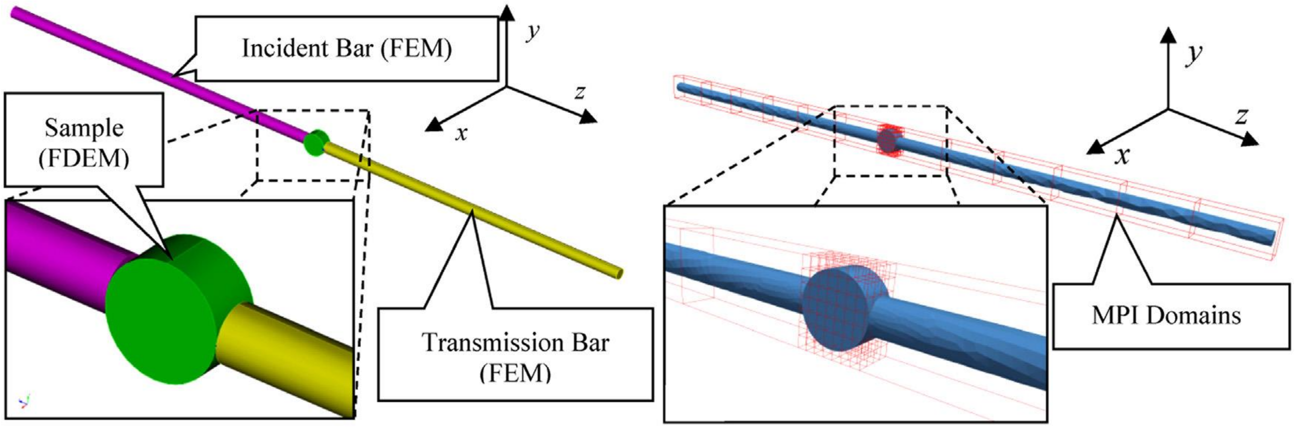

Figure 58. 3D setup of the HOSS numerical model with MPI domains.

RESULTS: The obtained crack initiation and propagation sequence is shown in Figure 59.

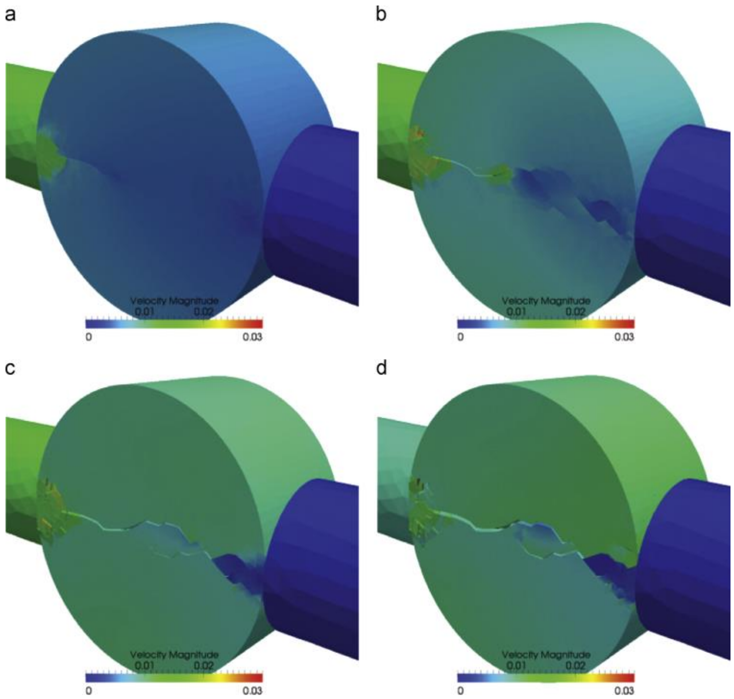

Figure 59. Sequence of the breakage of the sample.(a) 80 μs, (b)100 μs, (c)120 μs, and(d)140 μs.

The obtained fracture pattern sequence is shown in Figure 60 with Figure 61 showing the comparison between the simulation and experimental results.

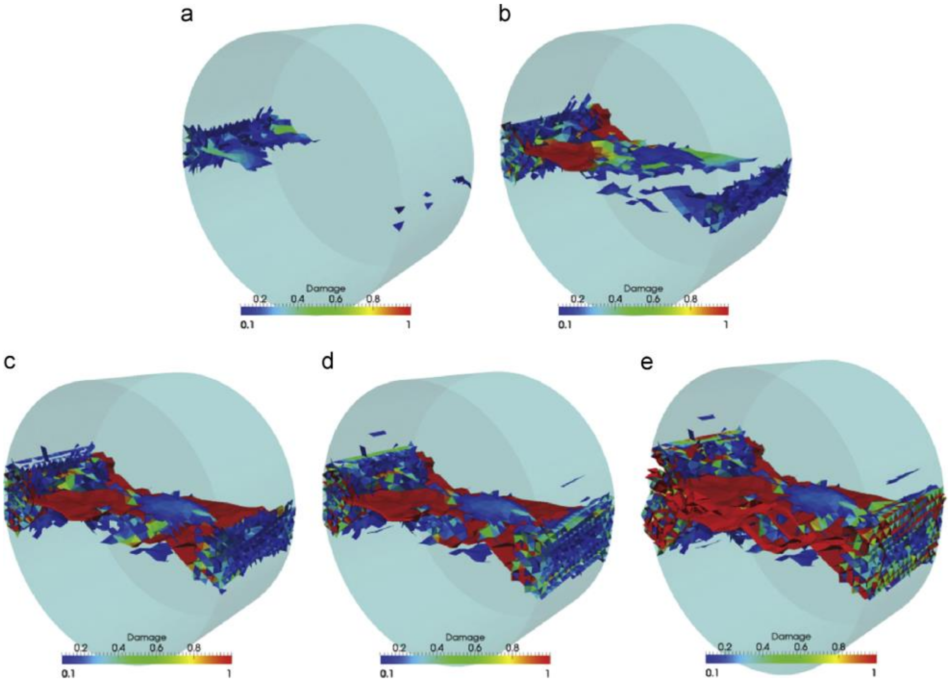

Figure 60. Fracture pattern sequence.(a) 80 μs, (b)100 μs, (c) 120 μs, (d) 140 μs, and (e) 460 μs. Incident and transmission bars are located to the left and to the right of the sample respectively.

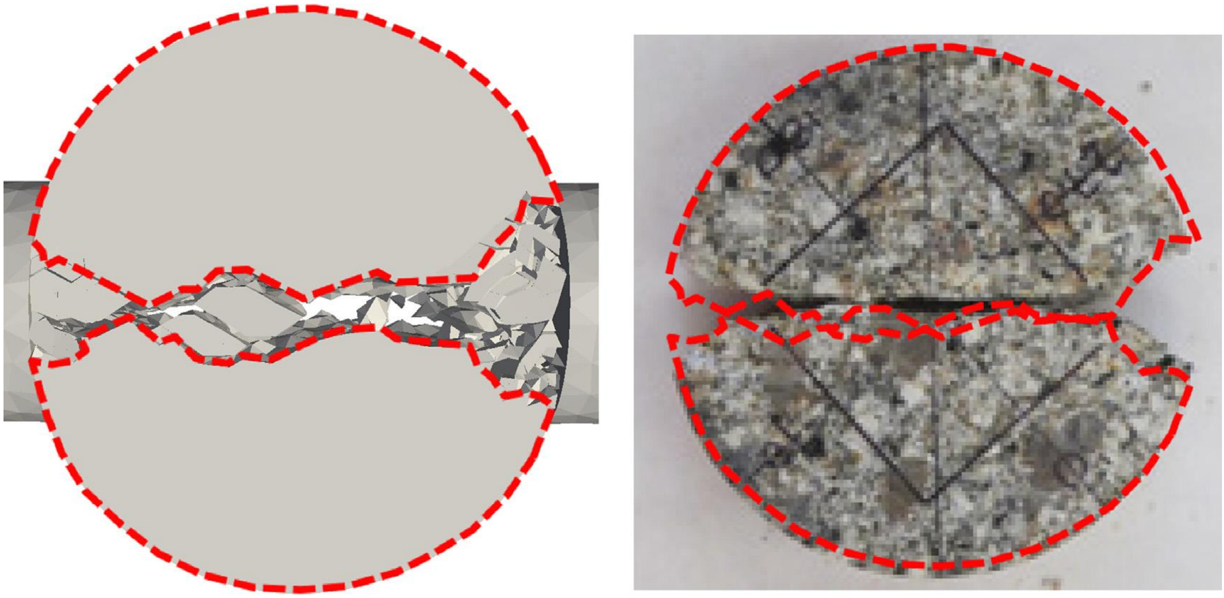

Figure 61. Comparison between the 3D FDEM results at 460 μs with the final shape of the sample after the physical experiment.

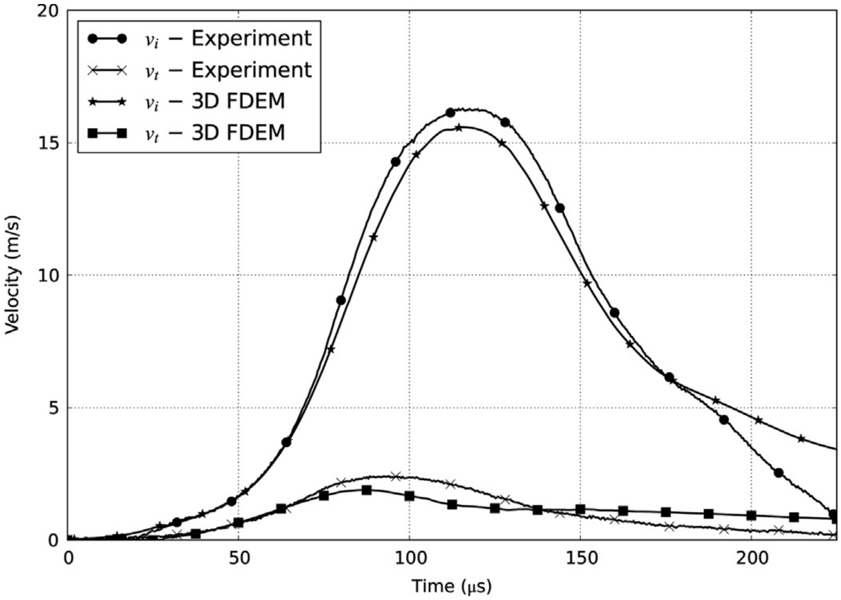

Figure 62. Comparison of the axial velocity of points located at the interface between the incident bar and the sample(v_i) and between the transmission bar and the sample (v_t).

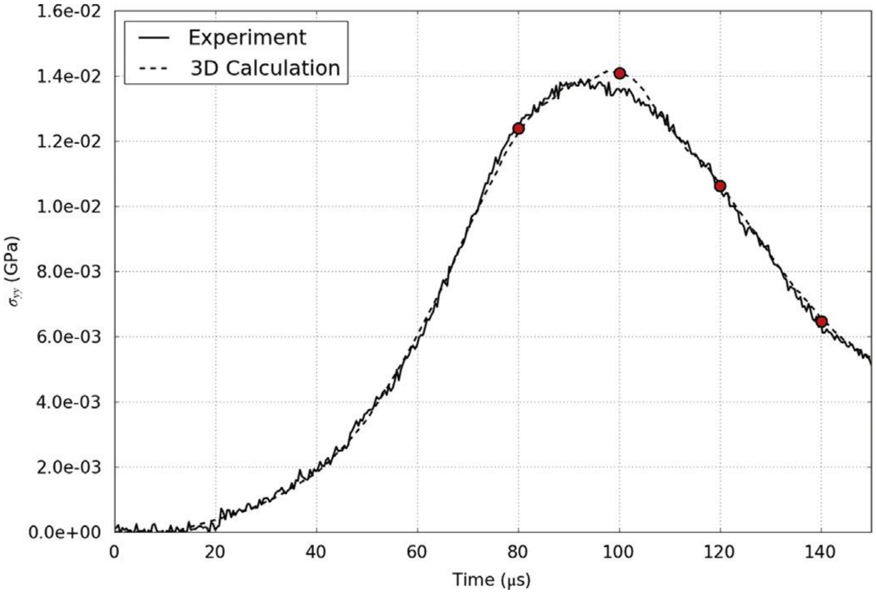

Figure 63. Tensile stress as a function of time. Note the softening behavior match. The red dots shown correspond to the frames shown in Figure 59.

Since FDEM simulation technology deals with complex phenomena of dynamic fracture and fragmentation, analytical results are not readily available. Existing experimental results are often not documented in a way suitable to be reproduced using numerical simulation (model parameters and/or data not being reported). Thus, a tailor made set of experiments was designed and performed at Sandia National Laboratory using granitic rock samples. The material properties of the rock have been measured in a format suitable for FDEM simulation. In addition, data acquisition was designed in such a way that a direct comparison of experimental and simulation results was possible as seen here. The simulation conducted here clearly demonstrates the ability of HOSS to model complex processes of dynamic fracture in a “virtual experiment” type of environment, where simulation setup closely mimics the experimental setup, including the FEM model of the incident and transmitting bars together with “simulation sensors” used for “data acquisition” from the simulation-based virtual experiment.

2.2 Flyer Plate Experiment

TYPE: Peer Reviewed Paper – Under Review

REFERENCE: Numerical Analysis of Flyer Plate Experiments in Granite via the Combined Finite Discrete Element Method. Computational Particle Mechanics.

AUTHORS: V. Chau, E. Rougier, Z. Lei, E.E. Knight, K. Gao, A. Hunter, G. Srinivasan, H. Viswanathan

ABSTRACT: In this study, the Finite-Discrete Element Method (FDEM), which merges the finite element based analysis of continua with discrete element based transient dynamics, contact detection, and contact interaction solutions, is used to simulate the response of a flyer-plate impact experiment in a Westerly granite sample that contains a randomized set of cracks. FDEM has demonstrated to be a strongly improved physical model as it can accurately reproduce the Velocity Interferometer System for Any Reflector (VISAR) plot, and capture the spall region and spall strength obtained from flyer plate experiments in granite. The number and the distributions of pre-existing fractures have also been studied to get better understanding of the effect of structural cracks on the mechanical behavior and the failure path of Westerly granite under high strain rate impact. These FDEM capabilities, in the context of rock mechanics, are very important for two main reasons. First, the FDEM can be further applied to many complex large scale problems such as planetary impact, rock blasting, seismic wave propagation, characterization of material failure around explosive crater formations, detection of hydrocarbon flow in petroleum industry, etc. Second, it can be used to validate high strain rate impact experiments and essentially, via virtual experimentation, replace these high cost experiments by very cost- and time-effective simulations.

PROBLEM DESCRIPTION:

In the recent study by Yuan and Prakash, plate impact experiments are employed to better understand the stress threshold for inelasticity in Westerly granite samples. The experiments are designed to obtain the Hugoniot Elastic Limit (HEL) as well as spall strength following shock-induced compression in the samples. The plate-impact experiments are conducted using an 82.5 mm bore single-stage gas-gun facility. Figure 2 shows the schematic of the plate-impact experimental configuration. The rear end of the projectile has a sealing O-ring and a Teflon key that slides key-way inside the gun barrel to prevent any rotation of the projectile. In our simulations, for simplicity, two dimensional plane strain conditions are assumed due to the O-ring constraint that produces zero strain in the radial direction of the target plate. In order to mimic the Teflon key effect on the target plate, roller supports are placed on the left and right side of the target plate. The aluminium flyer impacts the thick granite target plate with an initial velocity, which is modelled accordingly with the applied velocity on the flyer plate show in Figure 2. A poly-methyl methacrylate (PMMA) window plate is placed behind the granite target plate to provide a reflective surface to enable particle velocity measurements by using a laser interferometer. The multi-beam VALYN VISAR is used as the interferometer system to measure the free surface particle velocity history at the rear surface of the target plate (Yuan & Prakash, 2013). A sensor is placed in our FDEM model to record the particle velocity on the back of granite sample.

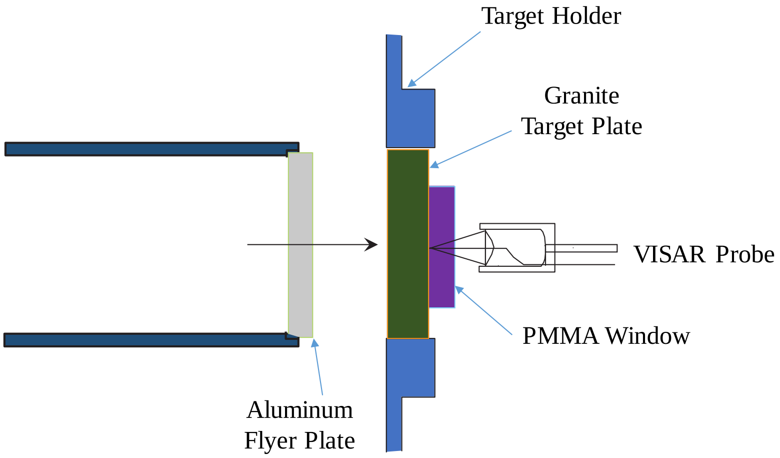

Figure 64. Schematic of the flyer plate experiment.

The FDEM material parameters for Westerly granite have been determined based on previously reported experimental results. The granite target plate has a Young’s modulus of 59.3 GPa and Poisson’s ratio of 0.28, while the Young’s modulus and Poisson’s ratio of the aluminum flyer plate are 80.7 GPa and 0.3, respectively. The Young’s modulus and Poisson’s ratio of the PMMA are estimated to be 5.0 GPa and 0.36, respectively. These materials are assumed to be elastically isotropic. The elastic properties are obtained from the previously mentioned laboratory experiment. Within the FDEM framework, contact interaction is resolved using the penalty method approach (Antonio A. Munjiza et al., 2011). This approach employs a penalty parameter in order to calculate the contact force. To achieve perfect contact without overlapping, this penalty parameter should be infinity. Since this is not numerically possible, a large but finite penalty parameter is employed. A recent study shows that in general a penalty parameter that is about 1-2 orders of magnitude larger than the Young’s modulus of the material will ensure the correctness of the results (Tatone & Grasselli, 2015). By compromising between achieving the correct elastic response between contact elements and maximizing the time step size in order to reduce the overall computational expense, a penalty parameter one hundred times larger than the particles’ Young’s modulus, i.e., 5930 GPa, is used.

The problem of interest is shown schematically in Figure 2. This figure illustrates the geometry of the FDEM model, which is based on the plate impact experiment. The model consists of 3 plates: aluminum flyer plate, granite target plate, and PMMA momentum trap. Within the sample, there are a number of pre-existing cracks each with initial lengths determined by a power law distribution, and randomly distributed orientations (Saadati, Forquin, Weddfelt, Larsson, & Hild, 2015).

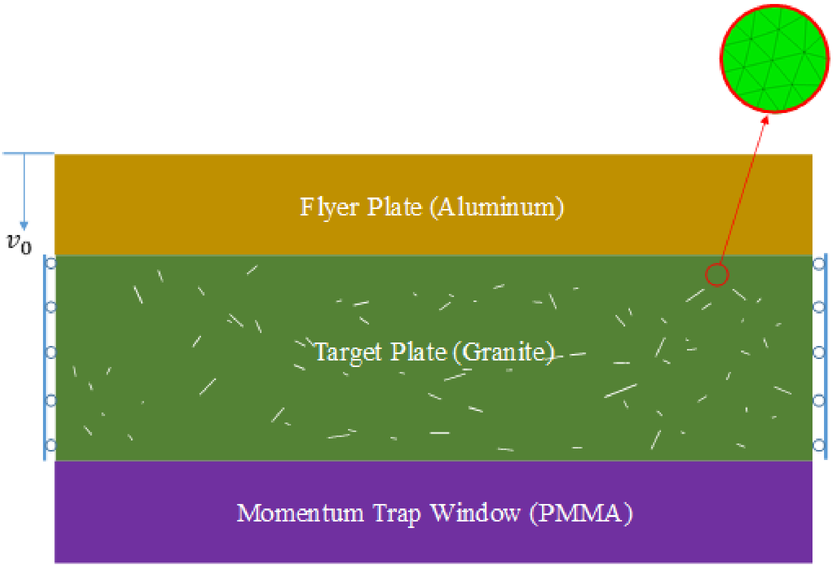

Figure 65. 3D setup of the HOSS numerical model with MPI domains.

RESULTS: The obtained crack initiation and propagation sequence is shown in Figure 4.

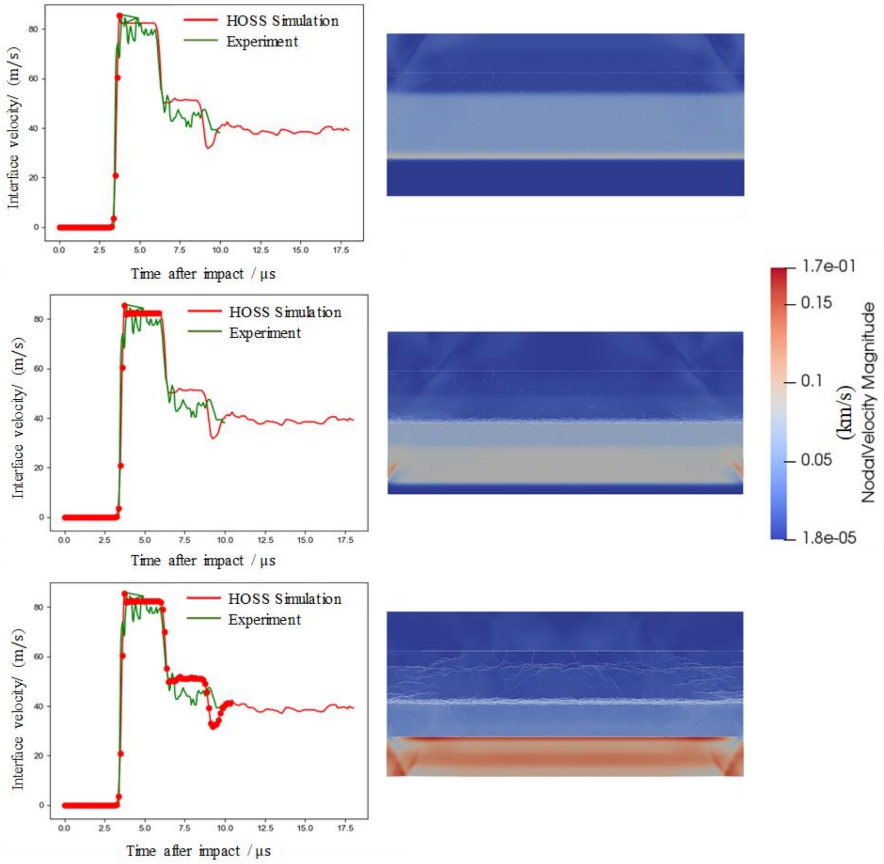

Figure 66. Particle velocity versus time (left) and corresponding nodal velocity profile (right) for an impact velocity of 91.5 m/s at different times: 3μs, 9μs, and 18μs.

From our simulation results, the spall strength, σ_{spall} can be calculated from the estimated particle velocities by using the following equations:

$$\sigma_{spall} = \frac{v_{\mathrm{B}} - v_{\mathrm{A}}}{2} \left(\rho C_L \right)_{granite} \tag{38}$$

$$v_{\mathrm{B}} = \frac{\left(\rho C_L \right)_{granite} - \left(\rho C_L \right)_{PMMA}}{\left(\rho C_L \right)_{granite}} v_{\max} \tag{39}$$

$$v_{\mathrm{a}} = \frac{\left(\rho C_L \right)_{granite} + \left(\rho C_L \right)_{PMMA}}{\left(\rho C_L \right)_{granite}} v_{\min} \tag{40}$$

where $\left(\rho C_L \right)_{granite}$ and $\left(\rho C_L \right)_{PMMA}$ represent the longitudinal impedance of granite and PMMA respectively.

Table 8: Spall strength calculated from simulation and experiment

	Experiment	Simulation	% Difference
Shot 1: V=91.5m/s	41 MPa	43.5 MPa	6.09%
Shot 2: V=156m/s	46 MPa	46.67 MPa	1.45%
Shot 3: V=249.1m/s	45 MPa	48.45 MPa	7.67%
Shot 4: V=356.1m/s	47 MPa	50.15 MPa	6.7%

As shown in Table 8, the spall strength of the Westerly granite at different impact stresses (or impact velocities) are calculated from the simulation results and is approximately 48 MPa. It is found that the spall strengths estimated from the experiments are in very good agreement with those from simulation, and it is nearly independent of the applied compression stress levels in the experiments. In overall, the simulated results slightly over-predict the experimental values due to the fact that the material model used for calculating the stresses is elastic and therefore, does not consider plastic processes (at the material point level inside the finite elements) that may take place in this type of experiment.

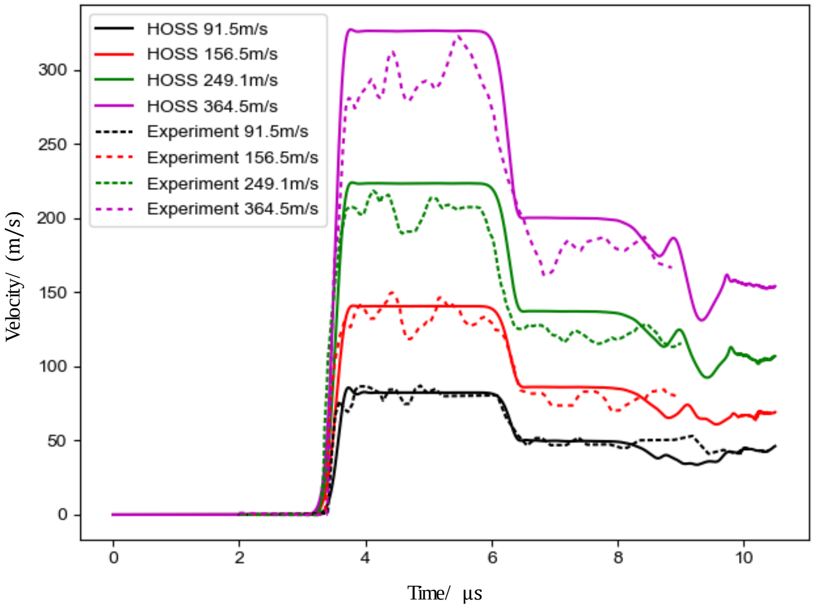

Figure 67. Particle-velocity versus time plot. Comparison between simulations vs. experiments, at impact velocities of 91.5 m/s, 156.5 m/s, 249.1 m/s, and 364.5 m/s.

In this work an in-house implementation of the Combined Finite-Discrete Element method (HOSS) was employed to simulate flyer plate experiments on Westerly granite samples. Simulated VISAR profiles show excellent matches to experimental VISAR profiles for an aluminum plate (flyer) impacting a granite plate. Multiple impact velocities were modelled and showed good matches for the spall strength calculations. The FDEM model doesn't need to calibrate many parameters like other pure continuum model or pure discrete models. All we need are the elastic material properties of granite, aluminum, and PMMA, such as Young modulus, density and Poisson ratio, and the strength properties, i.e., tensile and shear strengths, and their associated specific fracture energies. Overall, it is interesting to find that the common metric used to quantify the overall material response for these types of experiments, the VISAR signal, can be well matched. This motivates the need for models, such as the FDEM, that can explicitly capture the fracturing behavior of the material in addition to common metrics that can be measured experimentally. Such approaches can ensure that the fracturing process itself is accurately modeled.

2.3 Triaxial core-flood experiment of shale

TYPE: Peer Reviewed Papers, Conference Papers

REFERENCE: FDEM simulation on a triaxial core-flood experiment of shale. ARMA 49th US Rock Mechanics/Geomechanics Symposium, San Francisco, CA, June 28–July 1, 2015. https://www.onepetro.org/conference-paper/ARMA-2015-312

AUTHORS: Z. Lei, E. Rougier, E. E. Knight, A. Munjiza, W. Carey.

REFERENCE: Fracture-Permeability behavior of shale. Journal of Unconventional Oil and Gas Resources, 11: 27–43, 2015. https://doi.org/10.1016/j.juogr.2015.04.003

AUTHORS: J. Carey, Z. Lei, E. Rougier, H. Mori, H. Viswanathan.

REFERENCE: Shale fracture analysis using the combined finite-discrete element method. AGU Fall Meeting, San Francisco, California, USA, Dec. 15–19, 2014. http://adsabs.harvard.edu/abs/2014AGUFM.H11H0996C

AUTHORS: Z. Lei, J. W. Carey, E. Rougier, E. E. Knight, H. Viswanathan.

REFERENCE: Understanding hydraulic fracturing: a multi-scale problem. Philosophical Transactions of the Royal Society, 374: 20150426, 2016. https://doi.org/10.1098/rsta.2015.0426

AUTHORS: J. D. Hyman, J. Jiménez-Martínez, H. S. Viswanathan, J. W. Carey, M. L. Porter, E. Rougier, S. Karra, Q. Kang, L. Frash, L. Chen, Z. Lei, D. O'Malley, N. Makedonska.

ABSTRACT: Hydraulic fracturing (hydrofrac) is a very successful method that has been used to extract oil and gas from highly carbonate rocks like shale for a number of decades. However, there are still many aspects related to hydrofrac operations and how they affect the hydrocarbon's recovery levels that remain poorly understood. At Los Alamos National Laboratory (LANL), the combined finite-discrete element (FDEM) modeling team is working in conjunction with an experimental team to improve the understanding of fracture initiation and propagation in shale rocks. In this paper, in order to address the effects of the fluid pressure, a pseudo fluid solver has been implemented in HOSS. The pseudo fluid solver calculates the pressure in the fluid domain as a function of both the time and the distance from the fluid source. During the hydrofrac simulation, the pressure calculated from the pseudo solver is applied to the original free faces as well as the faces created by fracturing. After that, the sensitivity of the obtained fracture patterns related to uncertainties and/or changes in the boundary conditions is demonstrated using FDEM. Simulation results compared to triaxial core flooding experiments are presented. FDEM numerical simulations were able to replicate the main features of the fracturing processes while showing the importance of fluid penetration into fractures as well as layering in determining final fracture patterns.

PROBLEM DESCRIPTION: The setup of the FDEM model used in the simulations, which replicates the setup of the accompanying experiment conducted is shown in Figure 68. The rock sample is compressed in an asymmetric way by the action of two semi-circular, rigid anvils (direct shear configuration).

The shale rock sample was modelled by using 10 identical horizontal layers, denoted in Figure 68 by two different colors: yellow and blue. Within each layer the material properties are assumed to be homogeneous. At the interlayers, it is assumed that the material has a strength less than or equal to the strength inside of the layers. The material properties used for this analysis corresponded to those of a generic shale rock (Table 9).

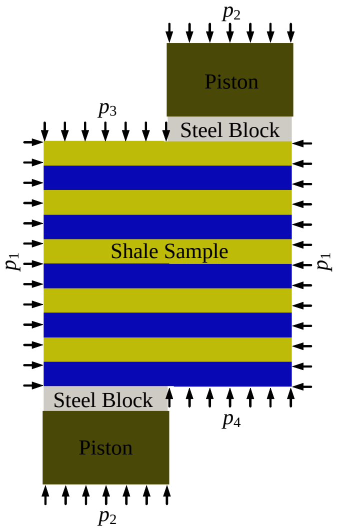

Figure 68. Model setup for the numerical simulations.

Table 9. Material parameters for the interlayers of the shale rock sample.

Parameter	Values
Young's modulus / MPa	12000
Poisson's ratio	0.15
Density / (kg/m^3)	2400.0
Tensile strength / MPa	9.7
Shear strength / MPa	33.7
Maximum normal displacement / m	0.0001
Maximum tangential displacement / m	0.00005

A summary of the cases modeled is presented in Table 10; where, p_1 is the confining pressure in the triaxial experiments, p_2 is the pressure applied by the action of the axial pistons under initial hydrostatic conditions and p_3 and p_4 represent the pore pressure at either end of the sample. η is the ratio between the material strengths in the interlayers and inlayers, i.e., $\eta=0.5$ means the strengths in the interlayers are half of that in the inlayers.

The simulation contains two main stages. In the first stage, the confining pressures are applied on the faces according to the accompanying experimental setup. A dynamic relaxation approach is used to get a stable, pre-stressed state for the shale sample. In the second stage, the top piston is slowly moved downwards while the bottom piston is slowly moved upwards. In this way, the sample is progressively strained and, eventually, the fracture propagation process is modelled.

Table 10. Summary of cases modeled.

Case	p_1 (MPa)	p_2 (MPa)	p_3 (MPa)	p_4 (MPa)	η	p_{frac}
1	3.45	6.89	1.24	1.38	0.5	YES
2	3.45	6.89	1.38	1.38	0.5	YES
3	3.45	6.89	1.24	1.38	0.5	NO
4	3.45	6.89	1.24	1.38	1.0	YES

In order to address the effects of the fluid pressure, a pseudo fluid solver has been implemented. In the pseudo fluid solver, we assume the fluid pressure is generated and propagated from a point source. The pressure at the point source can be defined as a function of time:

$$p_0 = p_0(t) \tag{41}$$

where the function $p_0(t)$ is provided as input to the FDEM analysis. Some examples of time histories of $p_0(t)$ for different conditions are shown in Fig. 1.

During the fluid pressure propagation, the fluid source has an area of influence that is determined by the pressure wave propagation speed and time. The distance from the source origin to the wave front is given by:

$$R = v \cdot t \tag{42}$$

where *v* is the wave speed and *t* is the time from when the fluid source started working.

Due to head losses, the fluid pressure decreases with range. The functional form describing the evolution of the fluid pressure as a function of both time and distance from the source origin is defined as follows

$$p = p_0 \varphi(d) \tag{43}$$

where $\varphi(d)$, represents the pressure decay as a function of distance *r* from the source origin. The decay function $\varphi(d)$ is also provided as input for the analysis. A typical shape of $\varphi(d)$ is shown in Fig. 2., where *d* is the relative distance from the source origin calculated as:

$$d = \frac{r}{R} \tag{44}$$

During the hydrofrac simulation, the pressure calculated from the pseudo solver is first applied to the specific free faces (e.g., the boundaries of the sample) and after fracturing occurs, the fluid pressure is applied on both the original free faces and the faces created by fracturing.

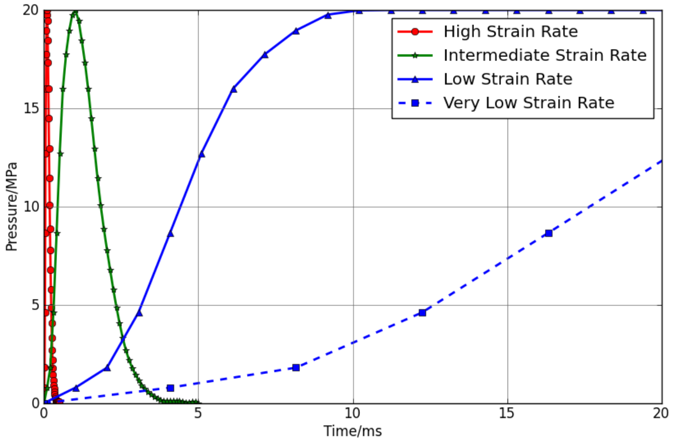

Figure 69. Examples of the pressure at the fluid source as a function of time.

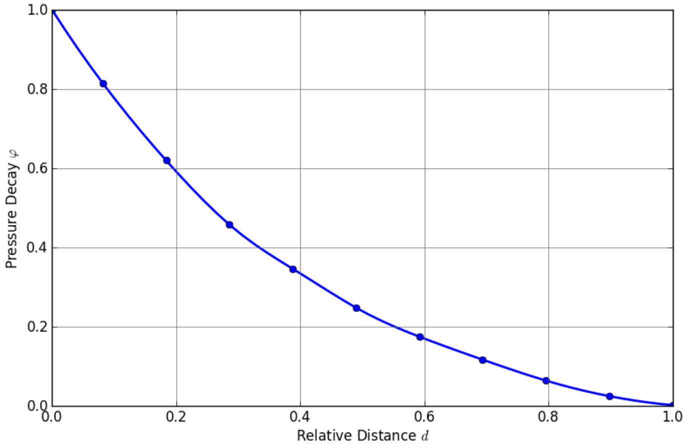

Figure 70. An example of the pressure decay as a function of relative distance from the fluid source origin.

RESULTS: A comparison between the final fracture patterns obtained from the numerical simulation against the experimental observations shows reasonable agreement (Figure 71): the main features of the experiment are reproduced, including the central fracture line, the two surrounding fracture arcs, and the densification of fracture networks near the anvils.

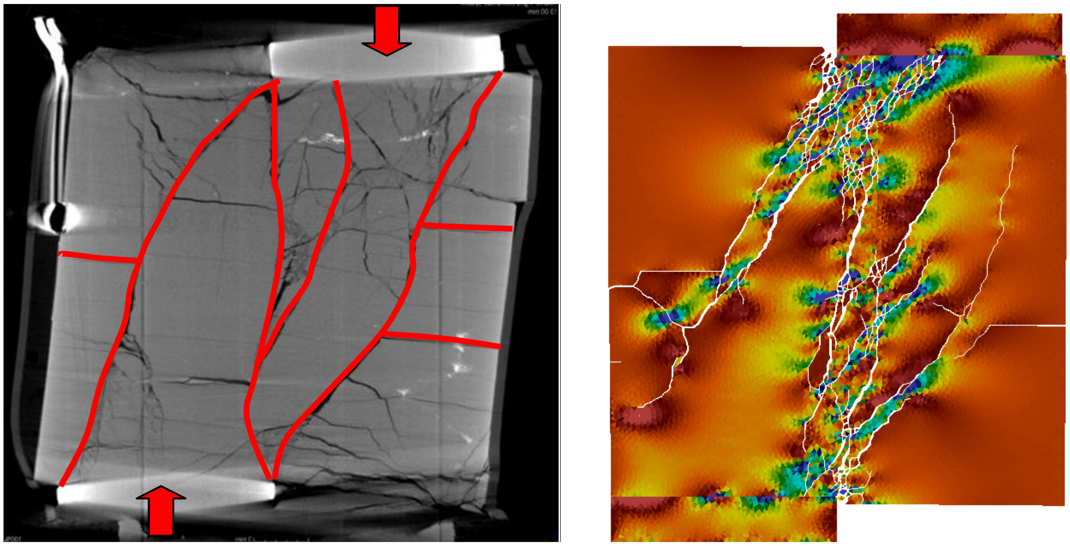

Figure 71. Comparison of experimental results vs. FDEM results for case 1.

For cases 1 and 2, two different values of the upper pore pressure (p_3) were used, while the lower p_4 was kept constant. The fracture patterns obtained for these two cases are shown in Figure 72, where some striking differences can be seen as a result of introducing small changes in the applied pore pressure. In case 1, a central vertical fracture system develops and it connects the edges of the anvils. The two bounding arcs are present, similar to case 2, but they are not as well developed as they are in case 2. Most interestingly, case 2 lacks any vertical fracture development.

In cases 1 and 2, once a fracture developed, a pressure equal to 1.38 MPa (representing the injected pore fluid) was applied to the surfaces of the fracture as it was explained earlier; these are called the wet fracture cases. For case 3, the fractures contained no fluid pressure and it is called the dry fracture case. A simple visual comparison of the final fracture patterns for cases 1 and 3 (Figure 73) vividly shows the importance of taking into account the effects of the fluid pressure on the fracture faces. In the dry fracture case, the fracture pattern is dominated by a central, vertical zone and it does not have the arcs extending from the anvil edges.

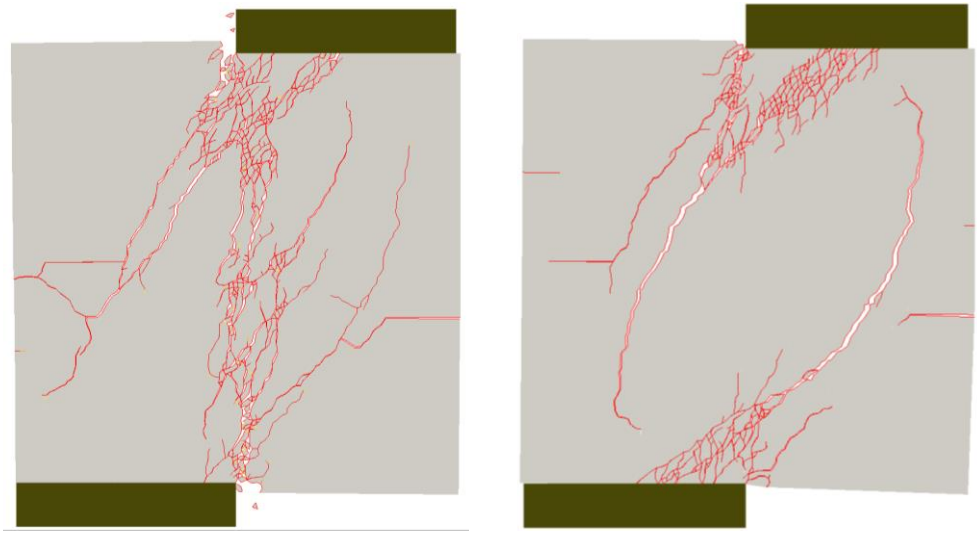

Figure 72. Comparison of numerical results for cases 1 (left) and 2 (right).

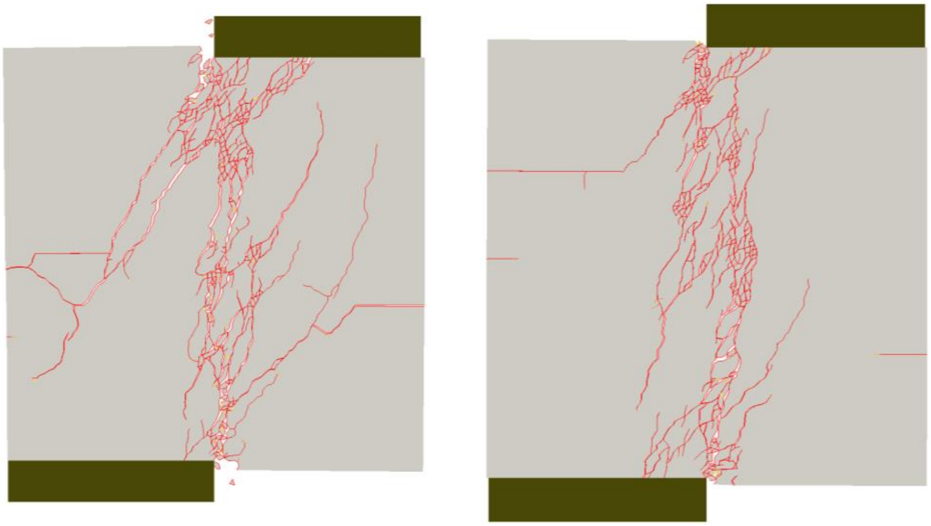

Figure 73. Comparison of numerical results for cases 1 (left) and 3 (right).

For cases 1 and 4 two different material strengths of the interlayer were simulated: 50% and 100% of the material strength of the layer (case 4 is essentially a homogenous sample). The fracture patterns obtained for these two cases are quite similar as seen in Figure 74.

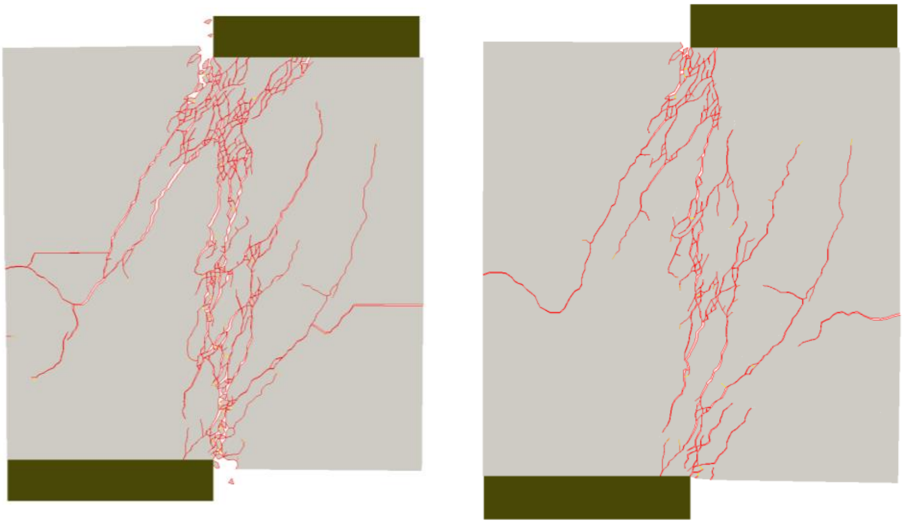

Figure 74. Comparison of numerical results for cases 1 (left) and 4 (right).

However, for case 4, without a contrast between the interlayer and layer properties, there were no fractures that developed along the interlayer, as was the case for the weak interlayer (case 1). Thus, the model with a weak interlayer reproduces the interlayer partings observed in the experiments.

2.4 Fracture Coalescence

TYPE: Peer Reviewed Paper

REFERENCE: Simulation of fracture coalescence in granite via the combined finite-discrete element method. Rock Mechanics and Rock Engineering (2019), pp. 1–15. https://doi.org/10.1007/s00603-019-01773-0

AUTHORS: B. Euser, E. Rougier, Z. Lei, E. E. Knight, L. P. Frash, J. W. Carey, H. Viswanathan, and A. Munjiza

ABSTRACT: Fracture coalescence is a critical phenomenon for creating large, inter-connected fractures from smaller cracks, affecting fracture network flow and seismic energy release potential. In this paper, simulations are performed to model fracture coalescence processes in granite specimens with pre-existing flaws. These simulations utilize an in-house implementation of the combined Finite-Discrete Element method (FDEM) known as the Hybrid Optimization Software Suite (HOSS). The pre-existing flaws within the specimens follow two geometric patterns: 1) a single flaw oriented at different angles with respect to the loading direction, and 2) two flaws, where the primary flaw is oriented perpendicular to the loading direction and the secondary flaw is oriented at different angles. The simulations provide insight into the evolution of tensile and shear fracture behavior as a function of time. The single-flaw simulations accurately reproduce experimentally measured peak stresses as a function of flaw inclination angle. Both the single- and double-flaw simulations exhibit a linear increase in strength with increasing flaw angle while the double-flaw specimens are systematically weaker than the single-flaw specimens.

PROBLEM DESCRIPTION: The experimental setup used by Lee and Jeon (2011) (Figure 75), is used as a reference for a 2-D numerical analysis of fracture coalescence in granite specimens. Two cases were studied: a specimen with a single flaw oriented at different angles with respect to the loading direction (Figure 75a); and a specimen with two flaws, where one flaw orientation is varied with respect to the loading direction (Figure 75b). For both cases, the vertical loading is applied at a constant strain rate such that quasi-static behavior is maintained. Samples are compressed between plates, where one is given a constant velocity and the other is fixed (i.e., no translation, rotation, or rigid body motion) in space. The coefficient of friction between the sample and the plates μ_s is assumed to be 0.5. The material properties used in the simulations are listed in Table 11.

Table 11. Material properties utilized in the simulations. The elastic constants and the strengths of Hwangdeung granite were reported by Lee and Jeon (2011). The fracture energies of the material are estimated based on values reported in literature (Backers 2004; Jeong et al. 2017; Paterson and Wong 2005)

Property	Value
Young’s modulus / GPa	55
Poisson’s ratio	0.15
Density / (kg m^{-3})	2650
Uniaxial Compressive Strength / MPa	209
Tensile strength / MPa	9.2
Cohesion (c) / MPa	54.4
Internal angle of friction (ϕ_c) / degrees	35
Mode I fracture energy (G_I) / (J m^{-2})	19.8

Mode II fracture energy (G_{II}) / (J m^{-2})	117.1

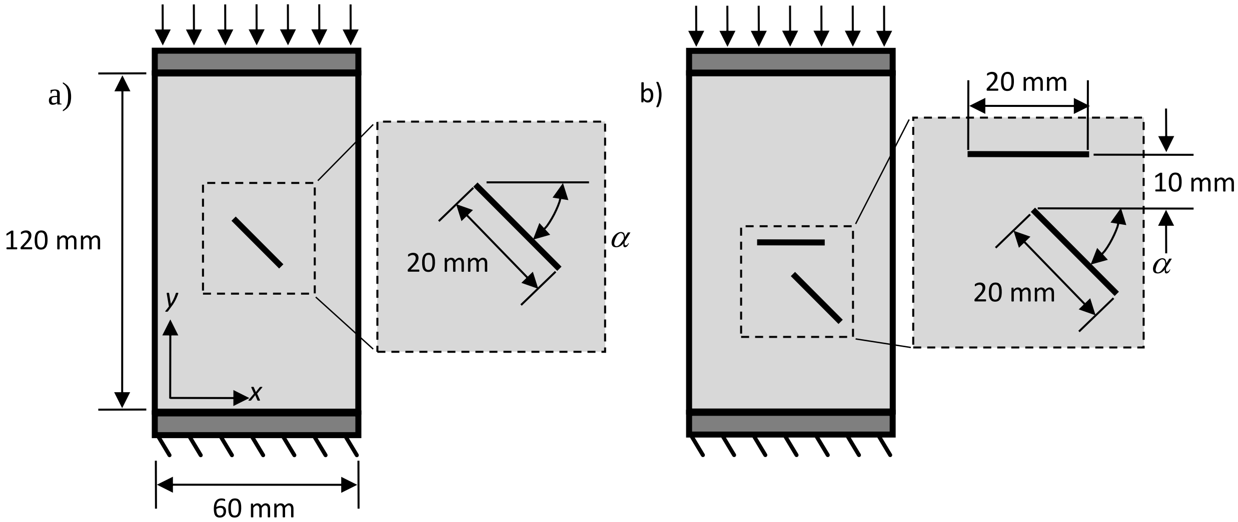

Figure 75. a) General model setup for the single-crack simulations; b) general model setup for the double-crack simulations

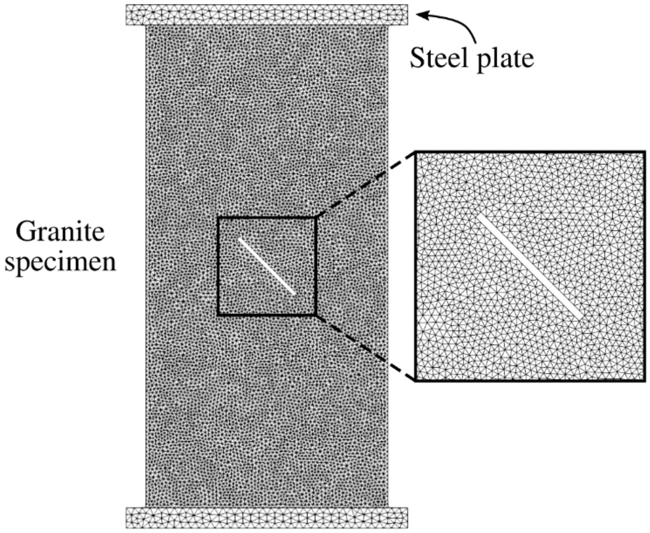

Figure 76. An illustration of the mesh for a typical simulation, the sample and the two plates are all treated as discrete solid domains that can interact with one another

RESULTS

Single-flaw specimen

Numerical results are compared to experimentally observed fractures patterns in Figure 77 and Figure 78 for the case of a specimen with a single, pre-existing flaw. The numerical results depict fractures color coded according to their damage type, where blue and orange are associated with shear and tensile damage, respectively. In most cases, only fully developed fractures (i.e., a damage value equal to 1) are visualized, as the numerical results are compared to unaided visual observations of experimental fracture patterns extracted from published images (Lee and Jeon

2011). A low fracture threshold (i.e., a damage value equal to 0.1) is used when illustrating the time series progression of fracture in Figure 77, as small amounts of damage noticeably affect the stress field.

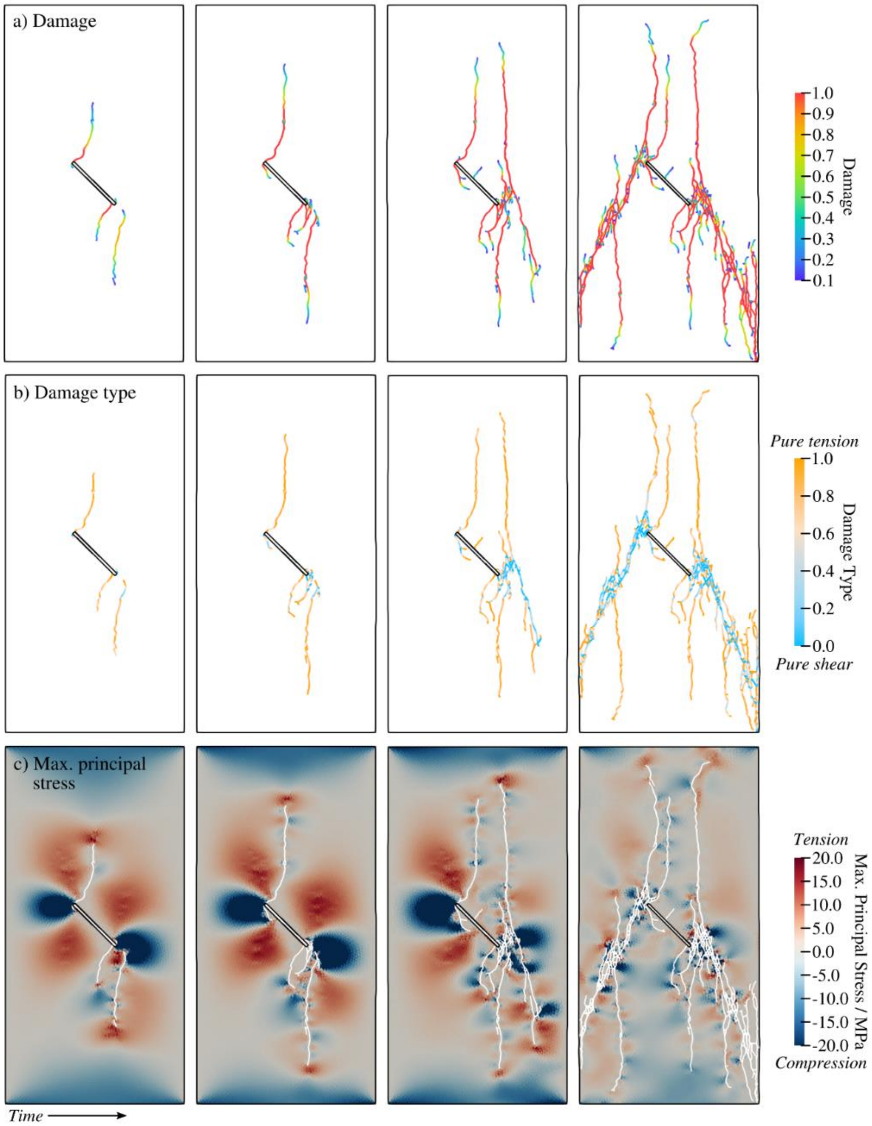

Figure 77. (a) Damage progression, (b) damage type, and (c) maximum principal stress in a specimen with a pre-existing flaw at an inclination angle $\alpha = 45°$

The stress profile in the linear-elastic regime is not identical for each simulation due to the influence of the flaw inclination angle on the stiffness of the specimen. Figure 78 shows the peak stress as a function of the flaw inclination angle α. As the angle of inclination increases, the peak stress also increases. The simulations produce peak stress values that are consistent with the experimental observations of peak stress and flaw orientation. While the DEM simulations performed by Lee and Jeon (2011) produced a similar trend, the current model more accurately predicts the magnitude of the stress (Figure 78).

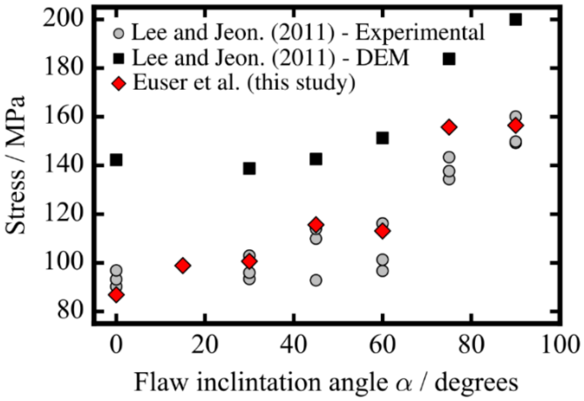

Figure 78. Peak axial stress as a function of crack inclination angle for the single-crack specimens, the numerical results are compared to experimental and numerical data reported by Lee and Jeon (2011)

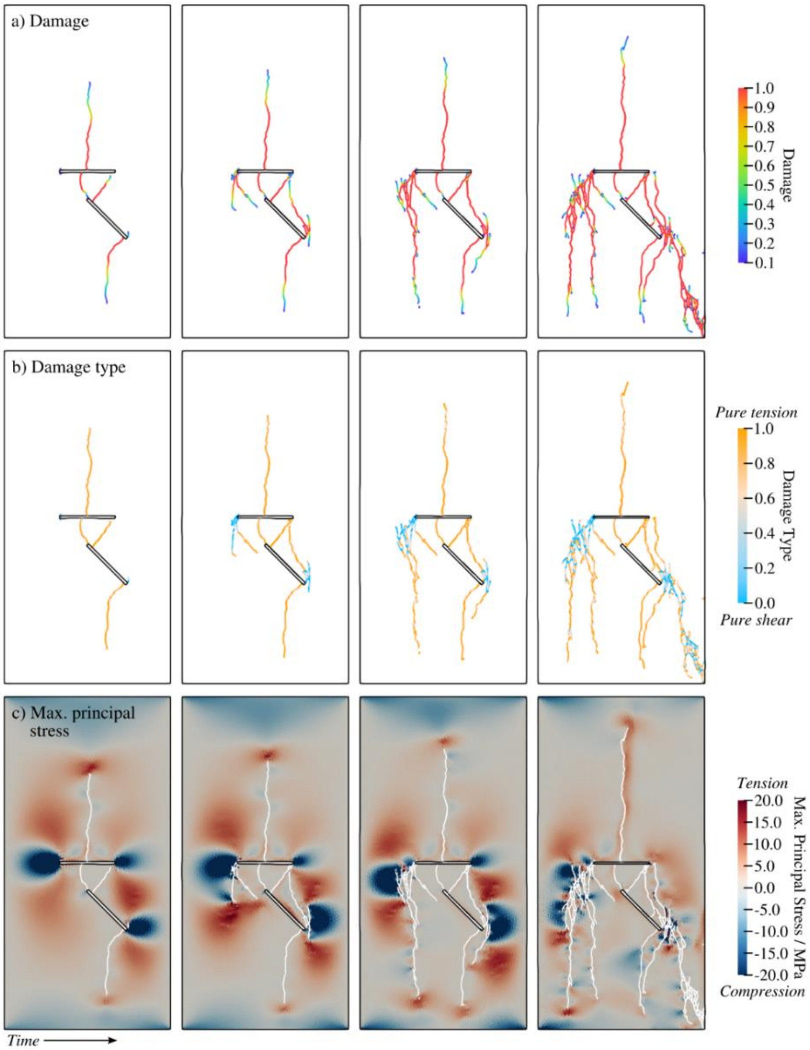

Figure 79. (a) Damage progression, (b) damage type, and (c) maximum principal stress development in a double-flaw specimen with the secondary flaw inclined at an angle of $\alpha = 45°$

Double-flaw specimen

Figure 79 illustrates the comparison of the numerical and experimental results for specimens with two pre-existing flaws. The inclination angle of the secondary flaw (Figure 75b) is varied from 15-90° in increments of 15°. A detailed illustration of the temporal evolution of the fracture and stress field in a double-flaw specimen with the secondary flaw oriented at an angle of 45° is shown in Figure 79. Initially, tensile cracks appear near the center of the horizontal crack and propagate in the direction of the maximum principal stress, and wing cracks emanate from the end of the inclined crack. As time progresses, shear fractures nucleate on the left edge of the horizontal flaw and near the right tip of the inclined fracture. The shear fractures that nucleated near the right tip of the inclined flaw propagate parallel to the flaw orientation, following a path through a region of large tensile principal stress.

Figure 80 shows the peak stress as a function of the inclination angle α for the double-flaw specimen; however, no experimental data are reported by Lee and Jeon (2011) for comparison. Similar to the case of the single-flaw specimen, the peak stress increases with increasing inclination angle. The peak stresses are lower than those observed for the single-flaw, which can likely be attributed to the presence of the primary horizontal flaw. As the secondary flaw becomes more vertical (i.e., $\alpha = 60° - 90°$), the horizontal flaw shields the secondary flaw against the vertical loading, and the magnitude of the peak stress (90 MPa) is consistent with the peak stress of the horizontal ($\alpha = 0°$) single-flaw simulation.

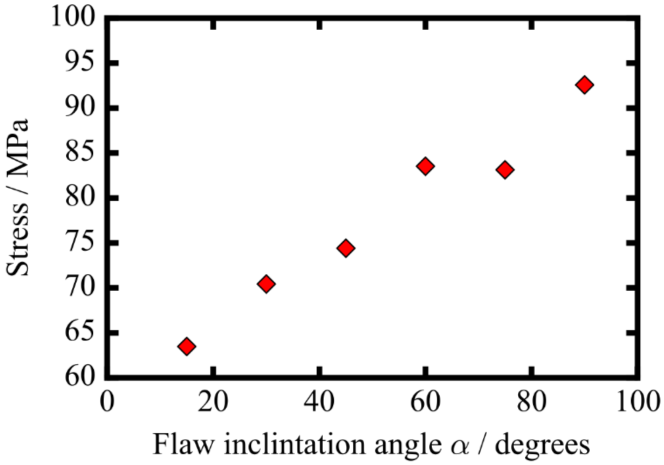

Figure 80. Peak axial stress as a function of flaw inclination angle for the double-flaw virtual specimens

For the single-flaw specimens, it is clear that there is a relationship between the flaw inclination angle and the amount of shear fracturing observed within the specimens. For small inclination angles, a mix of tensile and shear fractures contribute to the failure of the specimen. As the angle of inclination α increases, the failure of the specimens can be predominantly associated with shear fractures that are quasi-coplanar to the inclination angle. On the other hand, the double-flaw specimens largely experience failure due to shear fractures that nucleate at the tips of the primary and secondary flaws. Note that, as the angle of inclination increases for the secondary flaw in the double-flaw specimen, shear fracture nucleation shifts from the right tip of the secondary flaw to the right tip of the primary (i.e., horizontal) flaw. In both the single- and double-flaw cases, tensile fractures are generally ($\alpha < 60°$ for the single-crack specimens) more predominant than shear fractures in the early stages of fracture propagation. As time progresses, more and more shear fractures develop in the simulation leading to the eventual failure of the specimens in shear. From these figures it is clear that each specimen exhibits changes in slope in the linear-elastic regime, a behavior that is related to the relationship between the flaw inclination angle and the direction of loading (i.e., stiffer response is observed for pre-existing flaws aligned with the loading). Subsequent changes in slope, for axial strains of 0.1% and higher, are attributed to the onset of fracture.

References

Backers T (2004) Fracture toughness determination and micromechanics of rock under mode I and mode II loading. Dissertation, Universtiy of Postdam

Jeong SS, Nakamura K, Yoshioka S, Obara Y, Kataoka M. (2017) Fracture toughness of granite measured using micro to macro scale specimens. Procedia Engineering 191:761-767.

Lee H, Jeon S (2011) An experimental and numerical study of fracture coalescence in pre-cracked specimens under uniaxial compression. International Journal of Solids and Structures 48:979-999. doi:10.1016/j.ijsolstr.2010.12.001

Paterson MS, Wong T (2005) Experimental rock deformation - the brittle field. Berlin, Germany. doi:10.1007/b137431

2.5 Direct Shear Fracture Coalescence

TYPE: Conference Paper

REFERENCES: FDEM simulation on Fracture Coalescence in Brittle Materials. ARMA 49th US Rock Mechanics/Geomechanics Symposium, San Francisco, CA, June 28–July 1, 2015. https://www.onepetro.org/conference-paper/ARMA-2015-313

AUTHORS: Z. Lei, E. Rougier, E.E. Knight, A. Munjiza

ABSTRACT: Fracture coalescence has been identified as one of the factors playing an important role in the behavior of brittle materials. In this paper this phenomenon is simulated by using an in-house implementation of the Combined Finite-Discrete Element method (FDEM). Key aspects of FDEM include the introduction of finite displacements, finite rotations, and finite strain-based deformability combined with suitable material laws; the incorporation of discrete element based transient dynamics, contact detection, and contact interaction solutions and objective discrete crack initiation and crack propagation solutions that have a great deal of fidelity in reproducing complex fracture patterns and eventual fragmentation. The first examples presented in this paper consist of compression virtual experiments conducted on specimens that have two pre-existing flaws inside them. These fractures are arranged through the thickness of the specimens following different geometrical layouts. Some of the main features of the fracture propagation processes reported in this work are: initiation of wing cracks and secondary cracks; direction and propagation of the newly generated cracks and patterns of fracture coalescence. The results obtained in the simulations are qualitatively compared with experimental observations reported in the literature. This work is then extended to present results for a larger scale problem wherein fracture coalescence networks are observed when a pre-existing in-situ fracture network is stimulated.

PROBLEM DESCRIPTION: The model setup used in this work is shown in Figure 81. This setup followed the one used by Lee and Jeon for their experiments in Hwangdeung granite. The bottom of the sample is allowed to move only in the horizontal direction, while the top of the sample is pushed downwards at a constant speed. The analysis was run for three different values of the angle α (see Figure 81): 30º, 45º, and 60º.

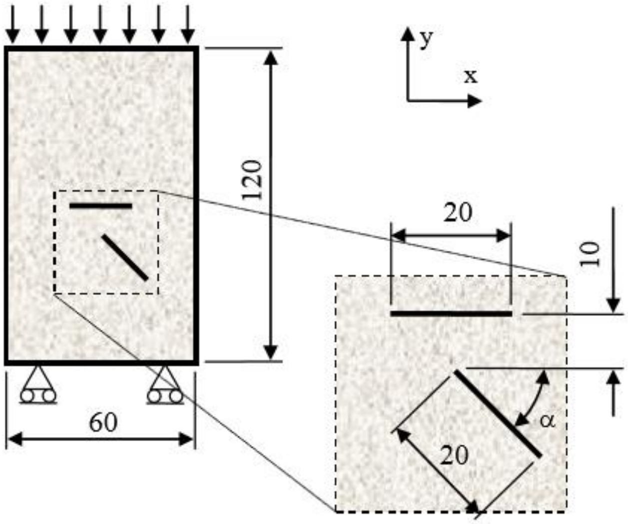

Figure 81. Model setup (all dimensions in mm), modified from Lee and Jeon.

RESULTS: A comparison of the results obtained from the numerical simulations against the experimental results reported by Lee and Jeon for the three cases with α equal to 30º, 45º, and 60º, are shown in Figure 82, Figure 83, and Figure 84, respectively.

In the first phase of the damage processes (frames b) fractures I, II, III and IV emanate from the pre-carved flaws. There is a very good agreement with fractures I, II and III and the experimental results. The remaining frames (c-f) show the progression of the propagation of the cracks until the collapse of the sample. As can be seen from the final frame of the simulation sequence, there is a quite good agreement between the modeling results and the experiments for the observed fractures i, ii, iii, iv, and v.

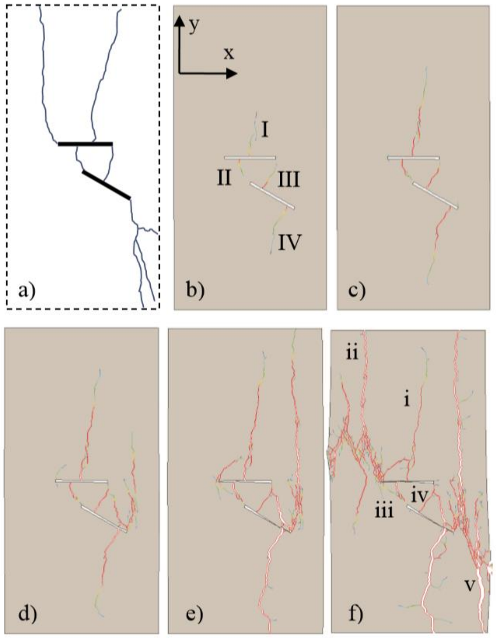

Figure 82. Coalescence of a horizontal flaw with a flaw inclined at 30 degrees clockwise with respect to the positive x axis: a) Fracture pattern reproduced from experiments; b) FDEM fracture pattern at the beginning of the failure process; c-f) FDEM fracture patterns at later stages in the simulation.

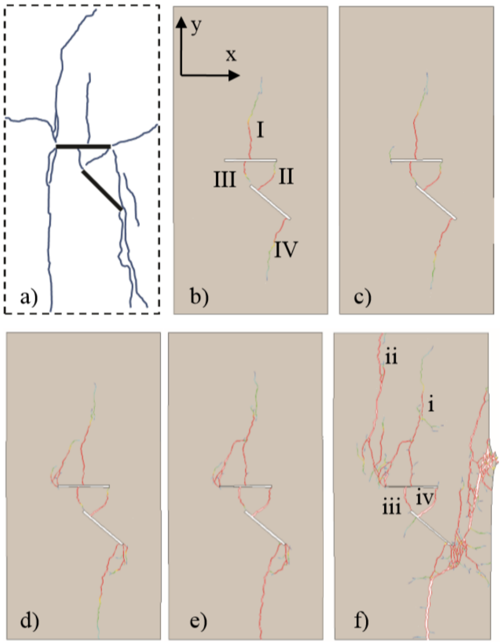

Figure 83. Coalescence of a horizontal flaw with a flaw inclined at 45 degrees clockwise with respect to the positive x axis: a) Fracture pattern reproduced from experiments; b) FDEM fracture pattern at the beginning of the failure process; c-f) FDEM fracture patterns at later stages in the simulation.

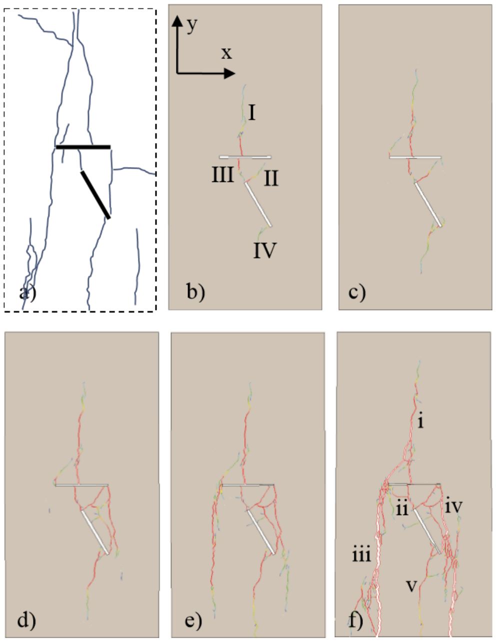

Figure 84. Coalescence of a horizontal flaw with a flaw inclined at 60 degrees clockwise with respect to the positive x axis: a) Fracture pattern reproduced from experiments; b) FDEM fracture pattern at the beginning of the failure process; c-f) FDEM fracture patterns at later stages in the simulation.

Although the FDEM results seen above are quite satisfactory for small laboratory scale experiments it is also necessary to show the method's capabilities when applied to much larger scale problems. Here, a 25m x 25m granite with an embedded *in-situ* fracture network is subjected to a constant speed kinematic boundary condition. Figure 85 displays the final fracture coalescence patterns.

As can be seen there is a high degree of complexity in this example and the method appears to perform quite adequately in representing fracture coalescence for much larger scale (albeit idealized) problems.

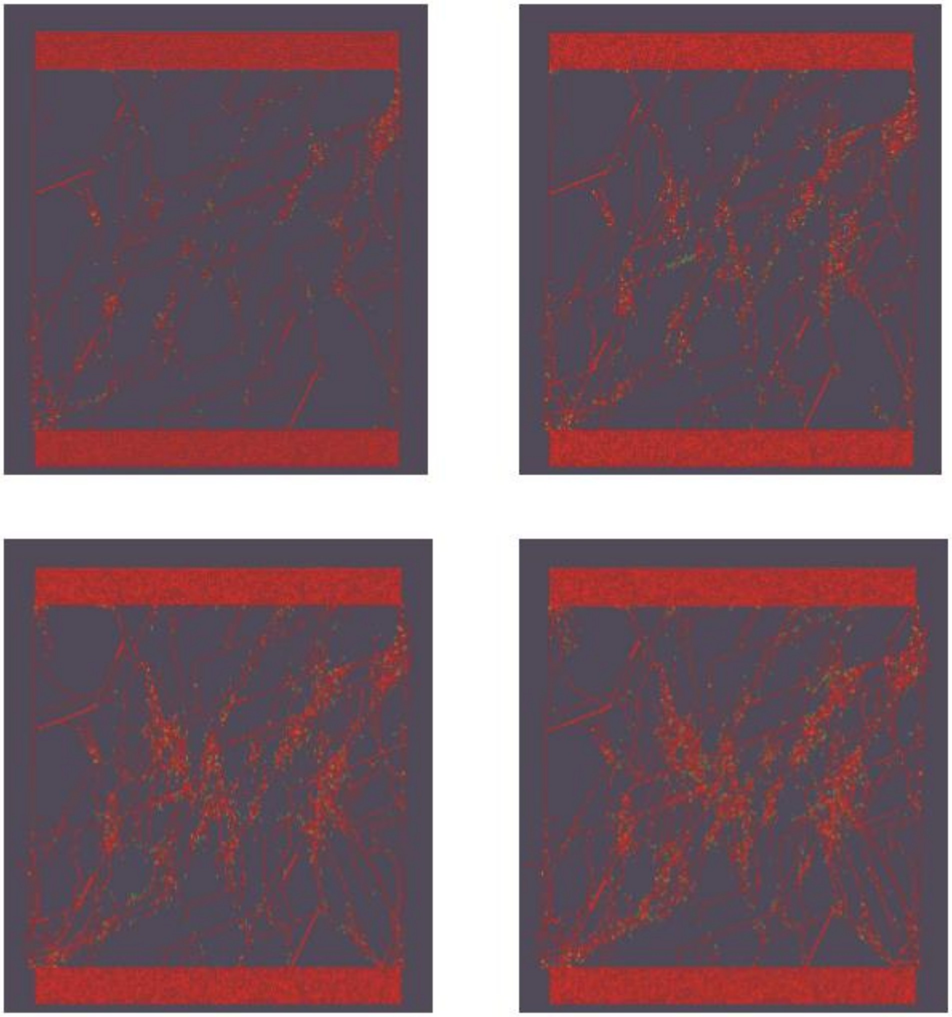

Figure 85. Latter stages of fracture coalescence seen in a large scale 25m x 25m granite block with a pre-existing in-situ fracture network.

2.6 Simulation of Mixed-mode Failure in Carrara Marble using the Combined Finite-Discrete Element Method.

TYPE: Conference Paper

REFERENCES: Simulation of Mixed-mode Failure in Carrara Marble using the Combined Finite-Discrete Element Method. ARMA 53rd US Rock Mechanics/Geomechanics Symposium, Brooklyn, NY, 23-26 June 2019.

AUTHORS: S. Boyce, J. Stormont, M. Reda-Taha, Z. Lei, E. Rougier, E. E. Knight.

ABSTRACT: In this paper the formation of hybrid fractures under mixed tensile and compressive stresses is investigated using the combined finite-discrete element method (FDEM). There are two common types of fracture in brittle geo-materials, tensile and shear. It is hypothesized that, under mixed tensile and compressive stress states, a corresponding mixed-mode, or hybrid fracture, will occur with a fracture plane at an angle greater than that of pure tensile fractures and less than that of pure shear fractures. Modelling a series of indirect tension tests with confining pressures increasing from 30 to 150 MPa allows for the development of stress states adequate to generate a spectrum of mixed-mode failure conditions. The models replicate previous experimental indirect tension tests on dog bone samples of Carrara marble. The results qualitatively agree with the experimental results from literature. This paper demonstrates that mixed-mode failure can be captured via numerical simulations, warranting further research to better understand mixed-mode fracture processes.

PROBLEM DESCRIPTION: The model setup used in this study is shown in Figure 86, in accordance with the experimental procedure used by Ramsey and Chester, 2004. The specimen is 90 mm tall with a 43 mm diameter base, and a 28 mm diameter neck. The radius of curvature for the neck is 91.5 mm. A biased tetrahedral meshing scheme, with a finer mesh size in the neck region, is used to increase computational efficiency.

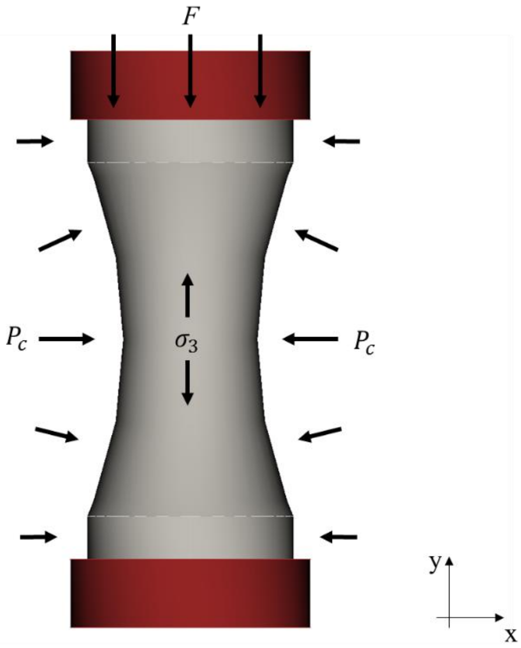

Figure 86. Model setup for confined extension tests on a dogbone geometry.

The material parameters for Carrara marble used in the simulation are obtained from literature and are shown in Table 12.

Table 12. Material Properties of Carrara Marble.

Young's Modulus	E (GPa)	65
Density	ρ (kg/m^3)	2626.4
Poisson's Ratio	υ	0.25
Tensile Strength	σt (MPa)	5
Shear Strength	τ (MPa)	20
Internal Friction Angle	φ (degrees)	37

The simulation consists of two phases. First, the confining pressure, P_c, is applied to the specimen, and an axial load, F, is applied via the top plate, while the bottom plate is held fixed. The first phase is continued until the system reaches a steady state condition, i.e., the kinetic energy of the system is dissipated. In the second stage, extension is initiated by displacing the top plate at a constant velocity; the bottom plate remains fixed through the duration of this stage. A convergence study on the plate velocity was performed to find the optimal velocity, 2.5e-2 m/s. Any further reductions in the speed of the plate did not affect the results of the simulation; thus, quasi-static conditions are assumed. The confining pressure remains constant throughout both stages, inducing an indirect tensile stress that eventually causes the specimen to fail.

Four different triaxial extension experiments were simulated on 3D, isotropic, homogenous samples, with confining pressures equal to 30, 70, 90, 150 MPa, respectively. These four cases provide conditions that vary from triaxial compression to confined tension.

RESULTS: Figure 87 illustrates the temporal propagation of a single mixed-mode fracture. The associated damage type matches this progression, as the cooler colours show shear fractures dominating initial failure at higher confining pressures near the edge of the specimen. Once these regions start to break, the axial force acts on a reduced cross-sectional area, increasing tensile stress, and causing tensile damage in the center of the specimen.

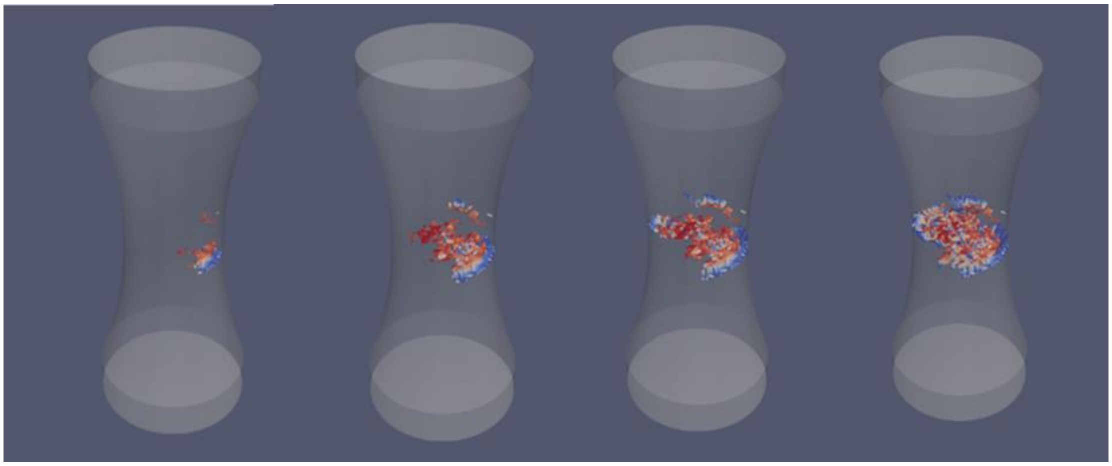

Figure 87. Propagation of fracture plane at a confining pressure of 90 MPa.

Figure 88 shows the progressive change in fracture orientation as the confining pressure increases; confirming the orientation of hybrid fractures planes at angles greater than those formed by uniaxial tension tests and less than fractures from triaxial compression tests.

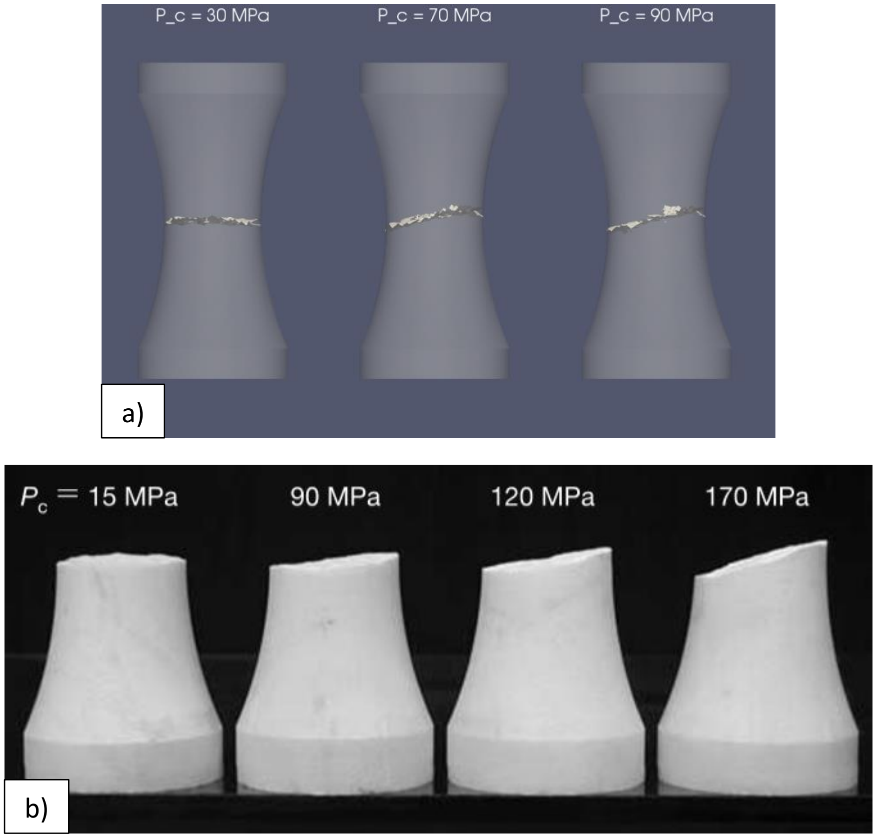

Figure 88. Progression in fracture plane orientation corresponding to increasing confining pressure; a) Fracture planes from FDEM simulations, b) fracture planes from experiments by Ramsey and Chester, 2004.

Table 13 provides a direct comparison of the results from numerical simulation and those reported by Ramsey. The values of axial force, F, at failure show good agreement with experimental values. The orientations of the fracture angles show qualitative agreement. It is interesting that the hybrid region has the least amount of error in terms of axial force but the greatest error when comparing the inclination of the fracture planes. It is worth noting that the experimental fracture planes were measured using a drag profilometer, while the simulated fracture planes are calculated to a best fit plane considering every node of the fracture. More importantly, the simulated specimens are perfectly isotropic and do not account for any possible heterogeneity that occur in the real samples. It is hypothesized that these factors are likely to contribute to the discrepancies observed in the fracture angle inclinations.

Table 13. Comparison of Results of Triaxial Extension of Carrara Marble

P_c (MPa)	F (kN)[1]	σ_3 (MPa)[1]	Fracture Angle (degrees)[1]	F (kN)[2]	σ_3 (MPa)[2]	Fracture Angle (degrees)[2]	Fracture Classification
30	20.2	-7.8	1.1	18.4	-10.9	0.9	Tensile
70	52.0	-10.6	1.9, 2.1	52.4	-9.9	10.4	Hybrid
90	71.0	-6.9	6.1	70.7	-7.6	12.2	Hybrid
150	128.1	4.3	19.9	126.2	1.5	19.3	Shear

[1] Experimental Data from Ramsey, 2004 [2] Numerical Results from FDEM Model

The numerical results agree with experimental work done by Ramsey and Chester, 2004. The axial force at failure for each case match with less than 10% error. While the orientations of the fracture planes and induced tensile stresses exhibit varying degrees of quantitative accuracy, they still qualitatively agree with the progressive increase in fracture with confining pressure. This paper demonstrates that mixed-mode failure can be captured via numerical simulations with the finite-discrete element method.

3 Fluid-Solid Interaction Solver (FSIS)

3.1 2D Stress Wave Propagation from a Single Source

TYPE: Peer Reviewed Paper – Under Review

REFERENCE: FSIS – A novel Fluid-Solid Interaction Solver for Fracturing and Fragmenting Solids. Submitted to Computer Methods in Applied Mechanics and Engineering.

AUTHORS: Munjiza, A., Rougier, E., Lei, Z., & Knight, E.E.

ABSTRACT: To address a wide range of multi-physics problems, an explicit fluid solver has been fully integrated (as opposed to coupled) into LANL's in-house combined finite-discrete element method code known as HOSS (Hybrid Optimization Software Suite). The solver addresses transient pressure wave propagation in fluid, fluid viscosity, equation of state for the fluid, energy transport, momentum transport and interaction with the fracturing solid domains, which is done through a novel immersed boundary approach. The solver is based on the governing equations being resolved using different control volume schemes, with discretization errors of either third, second or first order. The solver is fully explicit and conditionally stable with a time step that is synchronized with the FDEM's time step. Current FSIS implementation has been done in 2D. Extension to 3D is in progress.

PROBLEM DESCRIPTION: A single high energy source is placed in the center of the 2D mesh. The fluid pressure is modeled using an ideal gas EOS, as follows

$$\tilde{p} = -\tilde{\rho} R_{spec} \tilde{T} \tag{45}$$

where $\tilde{p}$ is the current pressure, R_{spec} is the specific gas constant and $\tilde{T}$ is the current temperature, which is given by

$$\tilde{T} = \frac{\tilde{E}}{\tilde{m} c_v} \tag{46}$$

where $\tilde{E}$ and $\tilde{m}$ are the current energy and current mass at each M-material node, while c_v is the specific heat at constant volume of the gas. It is worth noting that $R_{spec} = c_v(\gamma - 1)$ where γ is the ratio of the specific heat at constant pressure and the specific heat at constant volume ($\gamma = c_p / c_v$), so equation (46) reduces to

$$\tilde{p} = -(\gamma - 1)\frac{\tilde{E}}{\tilde{V}} \tag{47}$$

An instantaneous source is introduced by an initial deposition of energy ($\bar{e} = 1.0 \ \mathrm{MJ/kg}$) at time $t = 0$ inside the cell located at the center of the mesh.

RESULTS: From the onset the high pressure and high temperature gases contained in the source cell expand though the fluid domain with a wave front in the form of a circular shape, as shown in Figure 89. This example demonstrates that the fluid solver does not have preferential directions in terms of the wave speed and the symmetry of the problem is preserved.

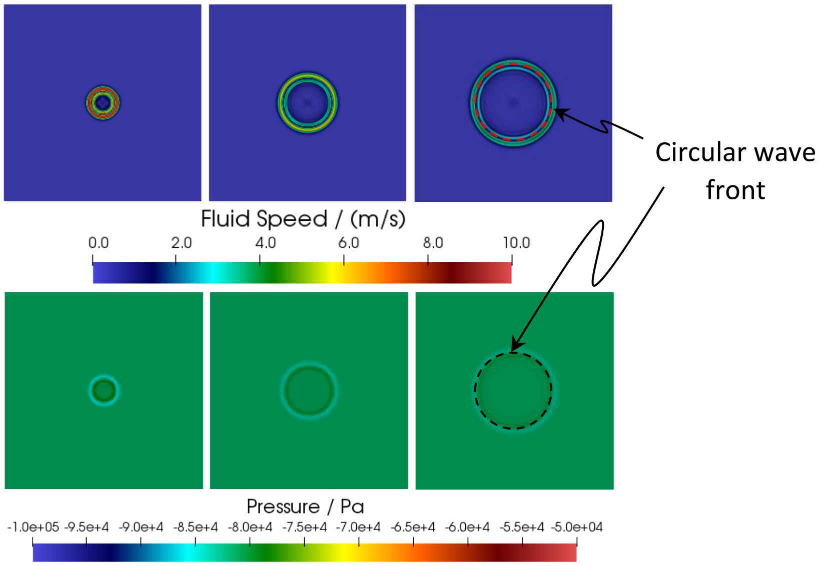

Figure 89. Temporal sequence of circular pressure wave propagation from a point source.

3.2 1D Compressible Flow – Sod Problem

TYPE: Peer Reviewed Paper – Under Review

REFERENCE: FSIS – A novel Fluid-Solid Interaction Solver for Fracturing and Fragmenting Solids. Submitted to Computer Methods in Applied Mechanics and Engineering.

AUTHORS: Munjiza, A., Rougier, E., Lei, Z., & Knight, E.E.

ABSTRACT: To address a wide range of multi-physics problems, an explicit fluid solver has been fully integrated (as opposed to coupled) into LANL's in-house combined finite-discrete element method code known as HOSS (Hybrid Optimization Software Suite). The solver addresses transient pressure wave propagation in fluid, fluid viscosity, equation of state for the fluid, energy transport, momentum transport and interaction with the fracturing solid domains, which is done through a novel immersed boundary approach. The solver is based on the governing equations being resolved using different control volume schemes, with discretization errors of either third, second or first order. The solver is fully explicit and conditionally stable with a time step that is synchronized with the FDEM's time step. Current FSIS implementation has been done in 2D. Extension to 3D is in progress.

PROBLEM DESCRIPTION: The setup of the Sod problem, also known as the shock tube problem, is shown in Figure 90-a. In this problem two gases at different pressures, $p_L > p_R$, and with different densities, $\rho_L > \rho_R$, are separated by an imaginary rigid membrane placed in the middle of the tube. Given a sudden burst of this membrane, the two gases in the tube try to equilibrate pressures and temperatures, thus creating a shock wave that travels from the middle of the tube towards the right and a rarefaction wave traveling from the middle of the tube towards the left. The following initial conditions were set for this example: $\rho_\mathrm{L} = 1.0\ \mathrm{kg/m^3}$, $p_\mathrm{L} = 0.1\ \mathrm{MPa}$, $\rho_\mathrm{R} = 0.125\ \mathrm{kg/m^3}$, $p_\mathrm{R} = 0.01\ \mathrm{MPa}$ and $\gamma = 1.4$. At a given point in time we highlight the results for five different areas, as shown in Figure 90-a: area L (left), where the gas is still at high-pressure high-density conditions; area R (right), where the gas is still at low-pressure low-density conditions; area 1, which is right behind the shockwave traveling into the low-pressure low-density area; area 2, which is right behind the density and specific internal energy discontinuity traveling behind the shockwave; and area 3, which contains the rarefaction zone.

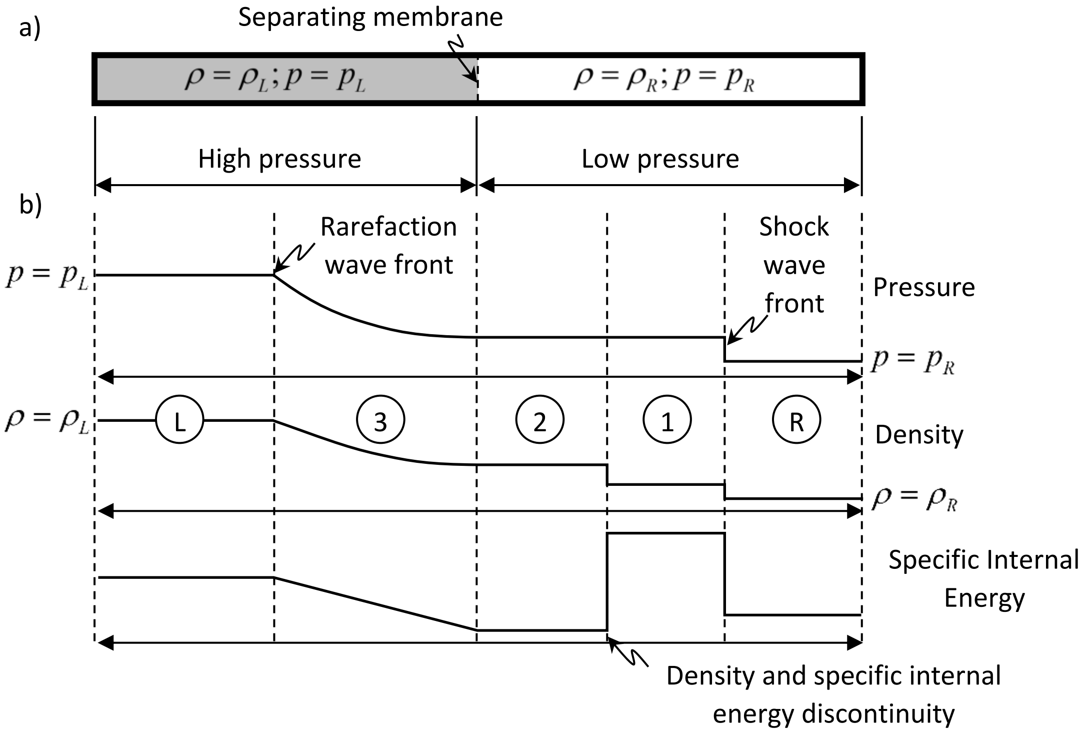

Figure 90. Schematic of the setup of the Sod problem.

RESULTS: The theoretical results for this type of problem can be found in Rathakrishnan, E. (2019) Applied Gas Dynamics (2nd Ed.). John Wiley and Sons LTD. ISBN 978-1-11950045-2. The results obtained using the FSIS developed in this work are shown in Figure 91. The obtained results show very good agreement with the analytical solution.

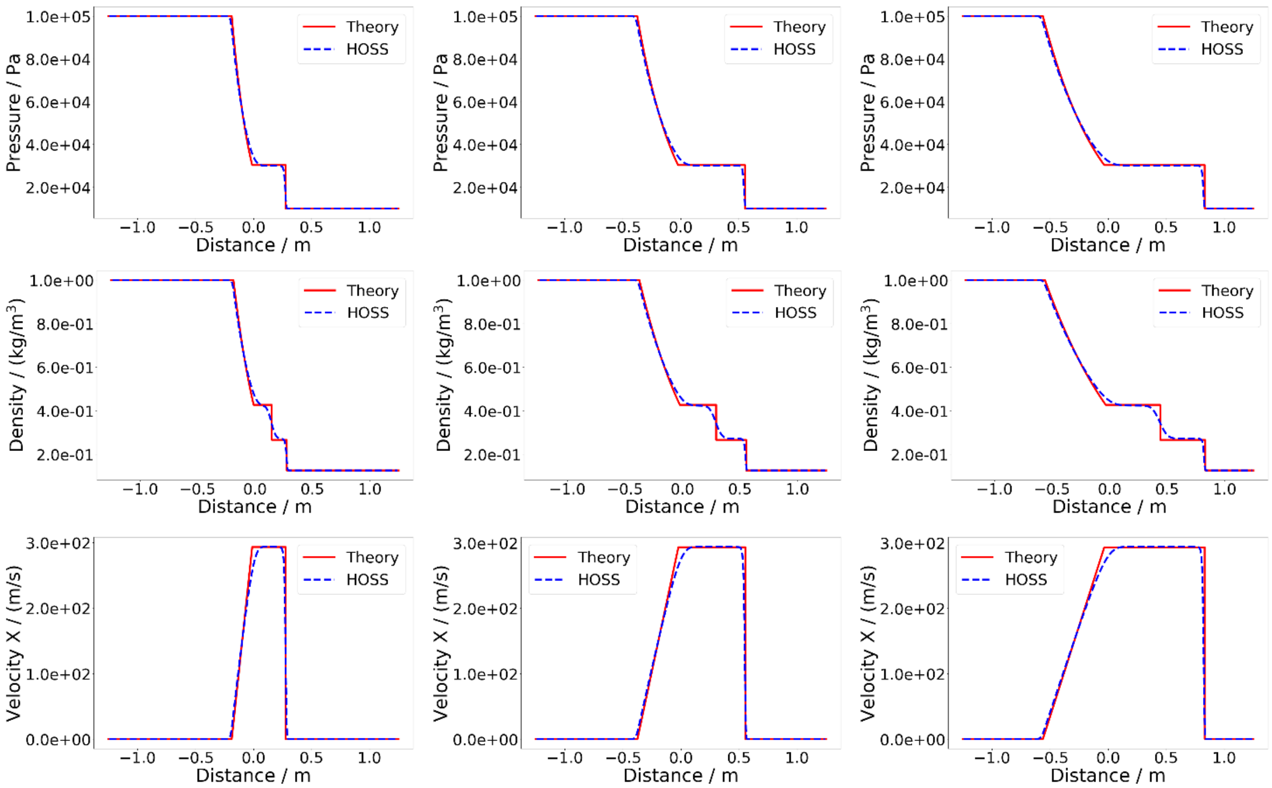

Time = 0.5e–3 s Time = 1.0e–3 s Time = 1.5e–3 s

Figure 91. Comparison of the numerical results obtained from the solver introduced in this paper with the theoretical solution of the shock tube problem. The three rows (in descending order) show the evolution of fluid pressure, density and velocity respectively. The three columns correspond to simulation times of 0.5e–3 s, 1.0e–3 s and 1.5e–3 s respectively.

3.3 Planar Poiseuille Flow

TYPE: Peer Reviewed Paper – Under Review

REFERENCE: FSIS – A novel Fluid-Solid Interaction Solver for Fracturing and Fragmenting Solids. Submitted to Computer Methods in Applied Mechanics and Engineering.

AUTHORS: Munjiza, A., Rougier, E., Lei, Z., & Knight, E.E.

ABSTRACT: To address a wide range of multi-physics problems, an explicit fluid solver has been fully integrated (as opposed to coupled) into LANL's in-house combined finite-discrete element method code known as HOSS (Hybrid Optimization Software Suite). The solver addresses transient pressure wave propagation in fluid, fluid viscosity, equation of state for the fluid, energy transport, momentum transport and interaction with the fracturing solid domains, which is done through a novel immersed boundary approach. The solver is based on the governing equations being resolved using different control volume schemes, with discretization errors of either third, second or first order. The solver is fully explicit and conditionally stable with a time step that is synchronized with the FDEM's time step. Current FSIS implementation has been done in 2D. Extension to 3D is in progress.

PROBLEM DESCRIPTION: For a successful planar Poiseuille flow simulation, the steady state solution for a viscous nearly incompressible laminar fluid flow driven by a pressure gradient between two parallel plates must be achieved. The general setup of the problem is shown in Figure 92. The inlet density, ρ_{in}, and velocity, $\mathbf{v}_{in}$, and the outlet pressure, p_{out}, are prescribed. No-slip boundary conditions between the fluid and the plates are also enforced during the simulation. The dimensions of the fluid channel are $L = 20.0 \text{ m}$ and $H = 1.0 \text{ m}$. Three different mesh sizes were tested in this benchmark exercise: $h_1 = 0.12500 \text{ m}$, $h_2 = 0.06250 \text{ m}$, and $h_3 = 0.03125 \text{ m}$. The values used in this example for the dynamic or first viscosity and for the second viscosity are $\mu = 3.0 \text{ Pa s}$ and $\xi = 0.0 \text{ Pa s}$ respectively. The x component of the inlet velocity, v_{xin}, was set in such a way that the x component of the maximum velocity across the cross section of the 2D channel, $v_{x\max} = 1.0 \text{ m/s}$, while the initial density of the fluid was set to $\bar{\rho} = 1.0 \text{ kg/m}^3$. The equation of state used in this benchmark example is the following

$$p = -\frac{1}{2}k\left(\frac{\tilde{\rho}}{\bar{\rho}} - \frac{\bar{\rho}}{\tilde{\rho}}\right) \tag{48}$$

where k is the bulk modulus of the fluid while $\bar{\rho}$ and $\tilde{\rho}$ are the initial and the current density of the fluid respectively. In this work $k = 100.0 \text{ kPa}$.

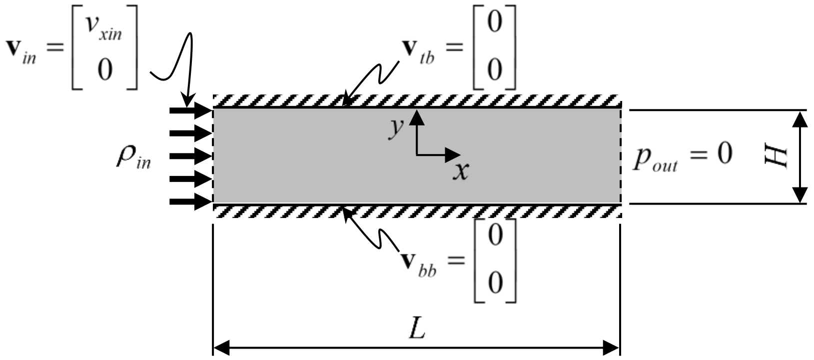

Figure 92. General setup for the planar Poiseuille flow problem. The inlet velocity, $\mathbf{v}_{in}$, and the inlet density, ρ_{in}, are fixed, as it is the outlet pressure, p_{out}. The velocity boundary conditions at the interface between the fluid and the top and bottom plates are prescribed by $\mathbf{v}_{tb}$ and $\mathbf{v}_{bb}$ respectively.

RESULTS: It is evident that the simulation recovers the exact velocity profile and this is for all grid resolutions. This is because the viscosity component is integrated with second order accuracy with respect to the space, which ensures that the exact result is achieved for a parabolic velocity profile, see Figure 93.

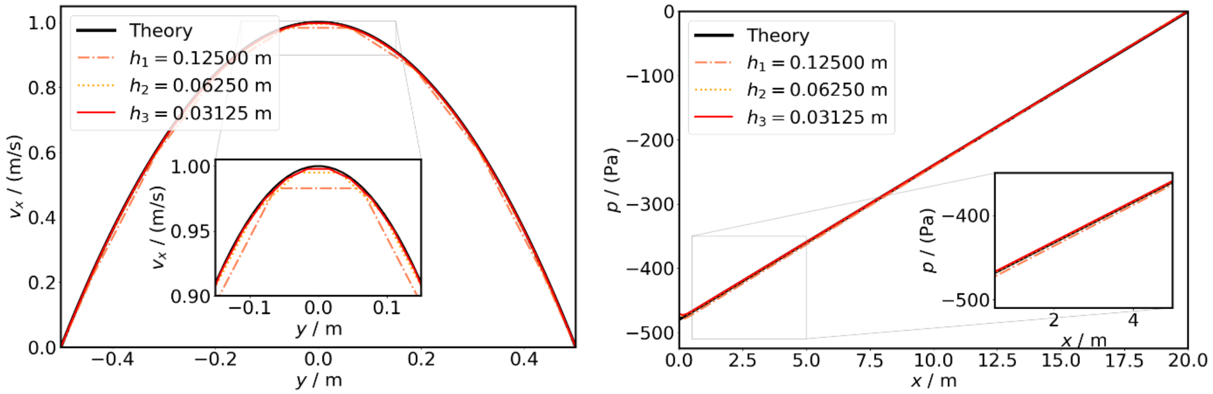

Figure 93. Flow between parallel plates. Results obtained for the mesh sizes used in this example. Left: Comparison between the theoretical and numerical solution for the x component of the fluid velocity across a cross section of the 2D channel. Right: Comparison between the theoretical and numerical solution for the fluid pressure decay along the 2D channel.

3.4 Lid-Driven Cavity Flow

TYPE: Peer Reviewed Paper – Under Review

REFERENCE: FSIS – A novel Fluid-Solid Interaction Solver for Fracturing and Fragmenting Solids. Submitted to Computer Methods in Applied Mechanics and Engineering.

AUTHORS: Munjiza, A., Rougier, E., Lei, Z., & Knight, E.E.

ABSTRACT: To address a wide range of multi-physics problems, an explicit fluid solver has been fully integrated (as opposed to coupled) into LANL's in-house combined finite-discrete element method code known as HOSS (Hybrid Optimization Software Suite). The solver addresses transient pressure wave propagation in fluid, fluid viscosity, equation of state for the fluid, energy transport, momentum transport and interaction with the fracturing solid domains, which is done through a novel immersed boundary approach. The solver is based on the governing equations being resolved using different control volume schemes, with discretization errors of either third, second or first order. The solver is fully explicit and conditionally stable with a time step that is synchronized with the FDEM's time step. Current FSIS implementation has been done in 2D. Extension to 3D is in progress.

PROBLEM DESCRIPTION: "The lid-driven cavity flow is most probably one of the most studied fluid problems in the field of computational fluid dynamics", Erturk, E. (2009). Discussions on driven cavity flow. International Journal for Numerical Methods in Fluids, 60:275-294. The setup of the problem is shown in Figure 94. The initial density of the fluid was set to $\bar{\rho} = 1000.0 \text{ kg}/\text{m}^3$, while the first (or dynamic) and second viscosities were set to $\mu = 0.1 \text{ Pa s}$ and $\xi = 0.0 \text{ Pa s}$ respectively, yielding a Reynolds number for the problem of 1000. Three different mesh sizes were used in this analysis: $h_1 = 0.00500 \text{ m}$, $h_2 = 0.00250 \text{ m}$ and $h_3 = 0.00125 \text{ m}$. The simulation was run until steady state conditions were reached, and then the streamline patterns were compared against those obtained by Erturk.

RESULTS: The obtained results are shown in Figure 95. The convergence of streamlines patterns in terms of grid resolution is clearly demonstrated (red lines correspond to the results obtained with the solver presented in this work – black lines correspond to the results from Erturk). A similar comparison (shown in Figure 96) was made against the results obtained from Botella, O. and Peyret, R. (1998). Benchmark spectral results on the lid-driven cavity flow. Computers and Fluids, 27(4):421-433, where similar convergence is observed.

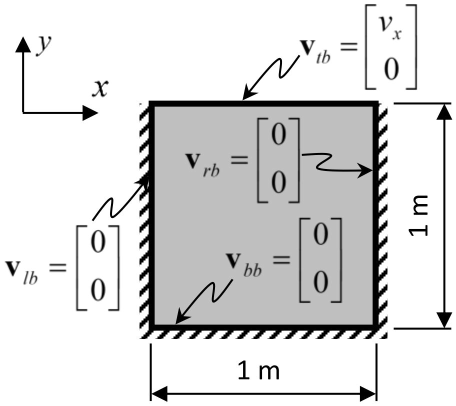

Figure 94. General setup for the lid-driven cavity flow problem.

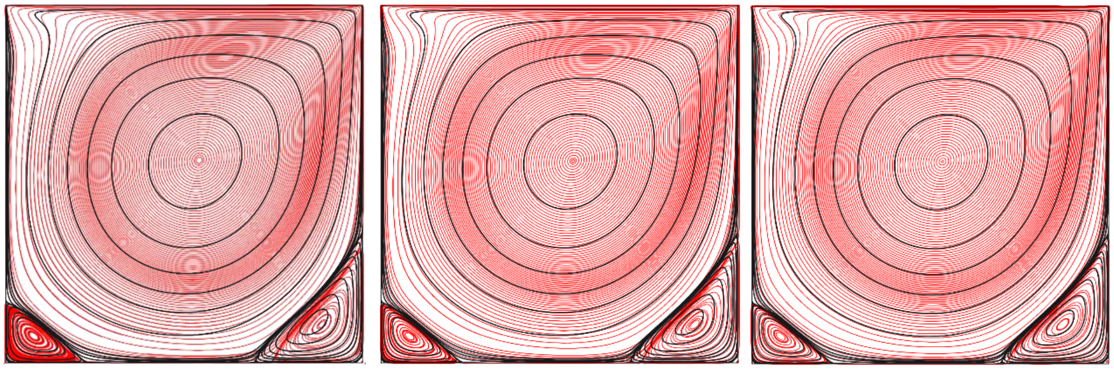

Figure 95. Comparison of steady state streamlines for the case of $\mathrm{Re} = 1000$ (red lines: current work) against the results obtained from Erturk, 2009 (black lines). Left: $h_1 = 0.00500\ \mathrm{m}$; Center: $h_2 = 0.00250\ \mathrm{m}$; Right: $h_3 = 0.00125\ \mathrm{m}$.

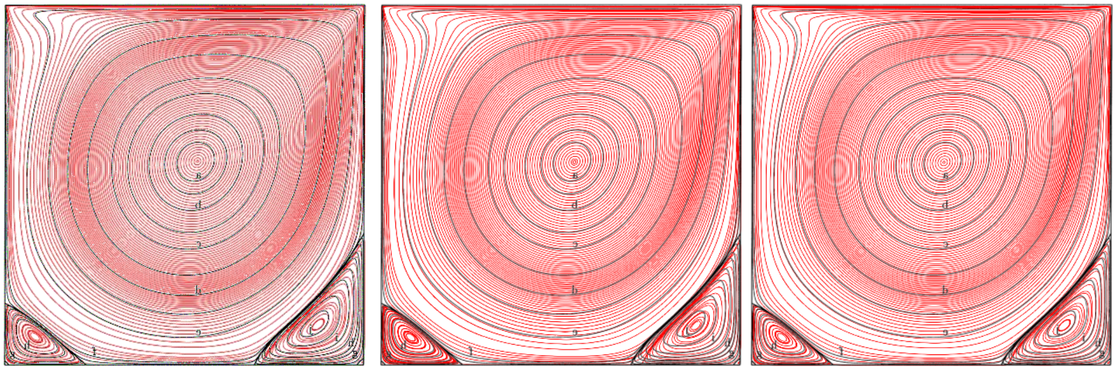

Figure 96. Comparison of steady state streamlines for the case of $\mathrm{Re} = 1000$ (red lines: current work) against the results obtained from Botella and Peyret, 1998 (black lines). Left: $h_1 = 0.00500\ \mathrm{m}$; Center: $h_2 = 0.00250\ \mathrm{m}$; Right: $h_3 = 0.00125\ \mathrm{m}$.

3.5 Von Karman Vortex Street

TYPE: Peer Reviewed Paper – Under Review

REFERENCE: FSIS – A novel Fluid-Solid Interaction Solver for Fracturing and Fragmenting Solids. Submitted to Computer Methods in Applied Mechanics and Engineering.

AUTHORS: Munjiza, A., Rougier, E., Lei, Z., & Knight, E.E.

ABSTRACT: To address a wide range of multi-physics problems, an explicit fluid solver has been fully integrated (as opposed to coupled) into LANL's in-house combined finite-discrete element method code known as HOSS (Hybrid Optimization Software Suite). The solver addresses transient pressure wave propagation in fluid, fluid viscosity, equation of state for the fluid, energy transport, momentum transport and interaction with the fracturing solid domains, which is done through a novel immersed boundary approach. The solver is based on the governing equations being resolved using different control volume schemes, with discretization errors of either third, second or first order. The solver is fully explicit and conditionally stable with a time step that is synchronized with the FDEM's time step. Current FSIS implementation has been done in 2D. Extension to 3D is in progress.

PROBLEM DESCRIPTION: Another well-established benchmark problem in fluid dynamics is named after Theodore von Karman (von Kármán, T. (1963) Aerodynamics. McGraw-Hill. ISBN 978-0-07-067602-2). The setup of the problem is shown below where a circular obstacle is placed in the middle of a laminar flow between two fixed plates. In this work the same dimensions adopted in Landau, L.D. and Lifshitz, E.M. (1987), Fluid Mechanics. Volume 6 if Course of Theoretical Physics, Second English Edition, Revised. Pergamon Press, were used, i.e., $L_1 = 8\text{ m}$, $L_2 = 25\text{ m}$, $H = 16\text{ m}$ and $\phi = 1\text{ m}$. The fluid's viscosities were set to $\xi = 0.0\text{ Pa s}$ and $\mu = 1.0\text{ Pa s}$, while the inlet fluid velocity was fixed at $v_{xin} = 100\text{ m/s}$, yielding a Reynolds number of 100. Three different mesh sizes were used for this case, $h_1 = 0.100\text{ m}$, $h_2 = 0.050\text{ m}$ and $h_3 = 0.025\text{ m}$. A monitoring point placed ten meters behind the center of the circular obstacle, is used to store the history of the fluid velocity during the simulations.

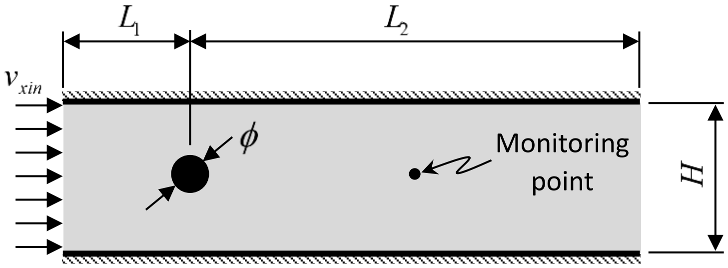

Figure 97. Problem setup for the von Karman vortex street problem.

RESULTS: Figure 98 shows the steady state map of the fluid velocity for the finer mesh size, i.e., $h_3 = 0.025\text{ m}$. A detailed view of the streamlines of the flow behind the circular obstacle is shown in Figure 99.

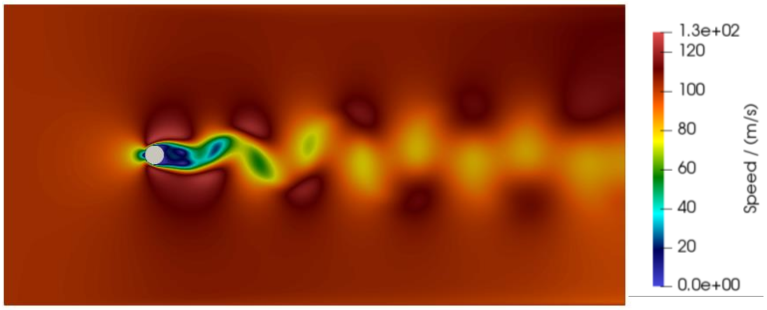

Figure 98. Final frame of the Von Karman street simulation for a mesh size $h_3 = 0.025\ \text{m}$.

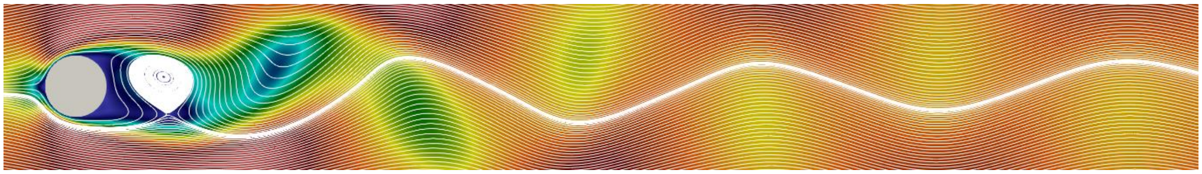

Figure 99. Detailed view of the final frame of the Von Karman street simulation showing the streamlines for a mesh size $h_3 = 0.025\ \text{m}$.

An example of the time history of the y-component of the velocity at the monitoring point for the finer mesh ($h_3 = 0.025\ \text{m}$) is shown in Figure 100-a). After the oscillations in the y-component of the velocity start to develop (around 0.2 s) it takes some time for the system to reach steady state conditions. In this analysis, Fast Fourier Transforms of the velocity time histories for the period of time defined by $2.0\ \text{s} \le t \le 4.5\ \text{s}$ were calculated and the frequency at which the peak of the spectra was observed was recorded (see Figure 100-b). The nature of the oscillatory flow behind the circular cylinder can be characterized via the Strouhal number which is given by

$$\text{St} = \frac{f\ L}{v} \tag{49}$$

where f is the frequency of the oscillations, L is the representative dimension of the problem (in this case $L = \phi$) and v is the free stream velocity of the flow. It has been demonstrated experimentally that, for a Reynolds number of 100, $0.16 < \text{St} < 0.17$, Roshko, A. (1954) On the development of turbulent wakes from vortex streets. Report 1191. California Institute of Technology – Work conducted for the National Advisory Committee for Aeronautics. The results obtained in this work show that, as the mesh size is decreased, the Strouhal number of the oscillatory flow behind the circular cylinder tends to the experimental range reported by Roshko, i.e., $\text{St}_{h_1} = 0.1260$, $\text{St}_{h_2} = 0.1437$ and $\text{St}_{h_3} = 0.1568$ for mesh sizes h_1, h_2 and h_3 respectively.

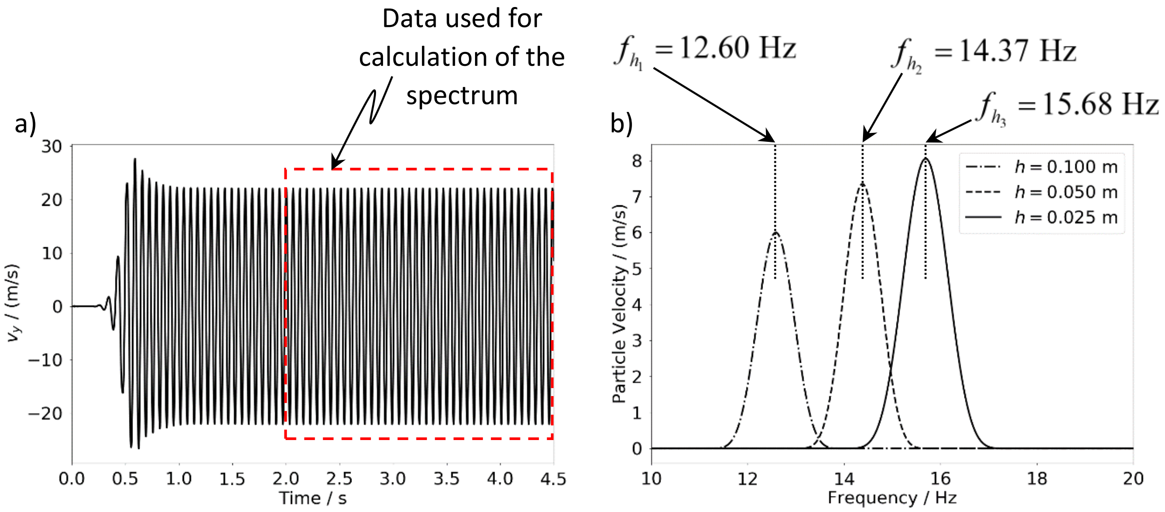

Figure 100. a) Time history of the y-component of the fluid velocity at the monitoring point (ten meters behind the center of the circular obstacle). b) Spectra of the y-component of the fluid velocity shown in the left pane.

3.6 High Energy Source inside a Disk

TYPE: Peer Reviewed Paper – Under Review

REFERENCE: FSIS – A novel Fluid-Solid Interaction Solver for Fracturing and Fragmenting Solids. Submitted to Computer Methods in Applied Mechanics and Engineering.

AUTHORS: Munjiza, A., Rougier, E., Lei, Z., & Knight, E.E.

ABSTRACT: To address a wide range of multi-physics problems, an explicit fluid solver has been fully integrated (as opposed to coupled) into LANL's in-house combined finite-discrete element method code known as HOSS (Hybrid Optimization Software Suite). The solver addresses transient pressure wave propagation in fluid, fluid viscosity, equation of state for the fluid, energy transport, momentum transport and interaction with the fracturing solid domains, which is done through a novel immersed boundary approach. The solver is based on the governing equations being resolved using different control volume schemes, with discretization errors of either third, second or first order. The solver is fully explicit and conditionally stable with a time step that is synchronized with the FDEM's time step. Current FSIS implementation has been done in 2D. Extension to 3D is in progress.

PROBLEM DESCRIPTION: In this section we demonstrate the robustness of the integrated solver in simulation of fluid driven fragmentation processes. The setup of the system is shown in Figure 101, where a square fluid domain of 3.7 m size is considered. A solid disk is placed inside the fluid domain and a high energy source is placed inside the fluid at the center of the disk (inset of Figure 101). At $t = 0$ s the high energy source is initiated at the center, which triggers the progressive initiation of the rest of the charge.

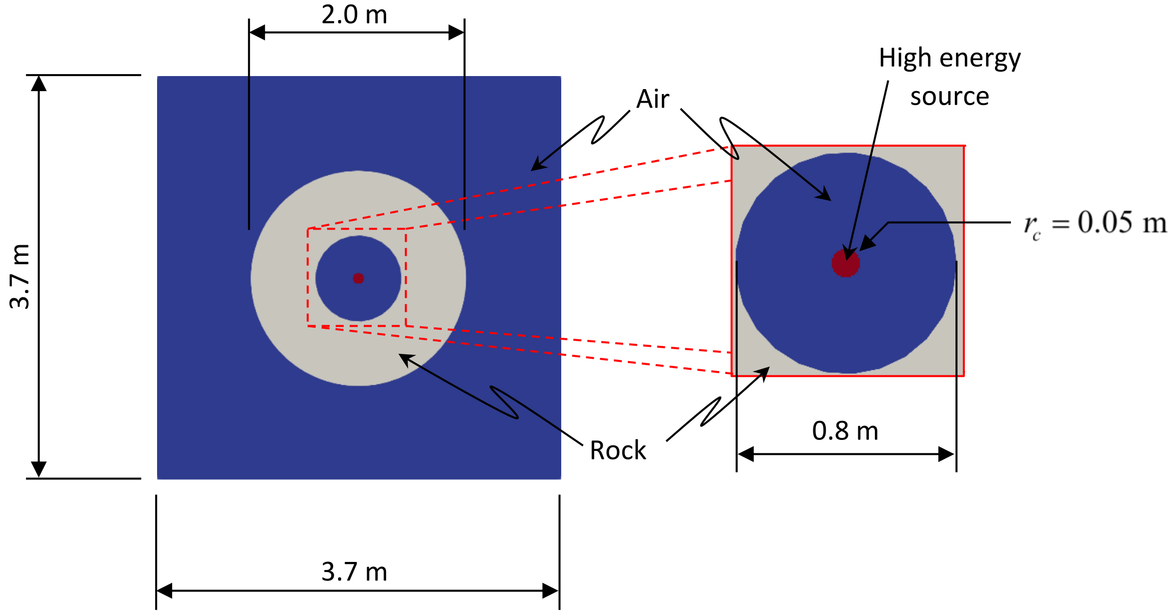

Figure 101. Problem setup: Fluid solver interacting with fracturing solids.

RESULTS: Figure 102 shows two snapshots of the simulation results corresponding to time instances $t = 5.0e-04$ s and $t = 4.0e-03$ s; solid fragmentation is shown in Figure 102-a and Figure 102-b, while the corresponding fluid pressure fields are shown in Figure 102-c and Figure

102-d. It is worth noting that the solid fragmentation produces a natural path for escape ("jet out") of the high-pressure, high-temperature gases contained inside the cavity, as shown in Figure 102-d.

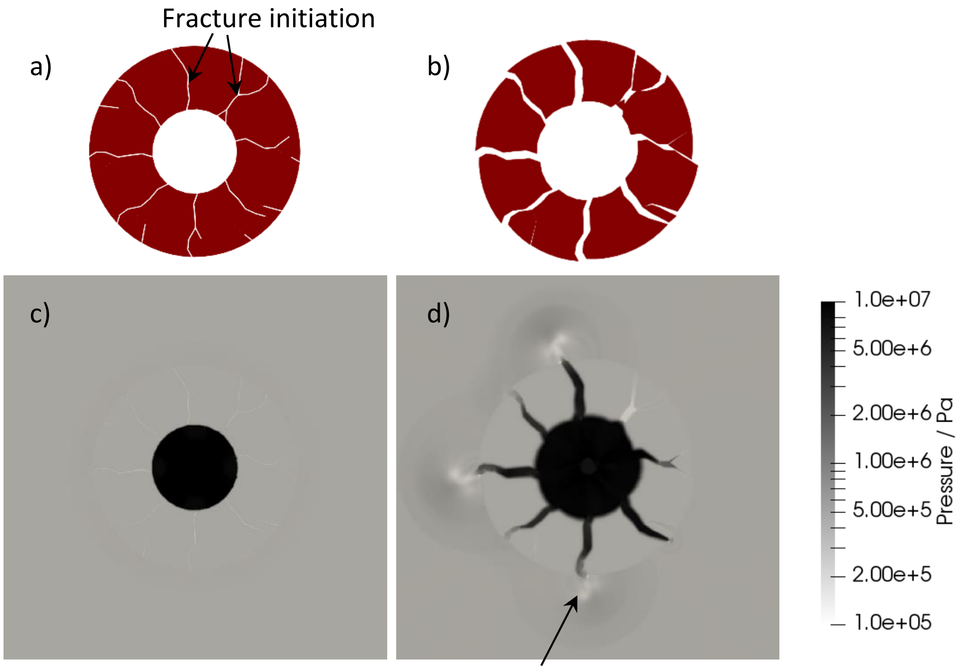

High temperature – high pressure fluid jetting from the cavity

Figure 102. Evolution of the fracturing process in the rock disk and fluid pressure as the solid fractures and fragments. a) and b) fracturing of the rock disk at 5.0e-04 s and 4.0e-03 s respectively. c) and d) map of fluid pressure at 5.0e-04 s and 4.0e-03 s respectively.

Figure 103 shows two snapshots of the velocity of the fluid; at $t = 5.0e - 04$ s and $t = 4.0e - 03$ s. The pressure wave in the surrounding air is generated by the deformation of the solid. Later on, at $t = 4.0e - 03$ s the gas jetting, though the fractured solid, at high pressure and high temperature is clearly observed (see Figure 103-b)

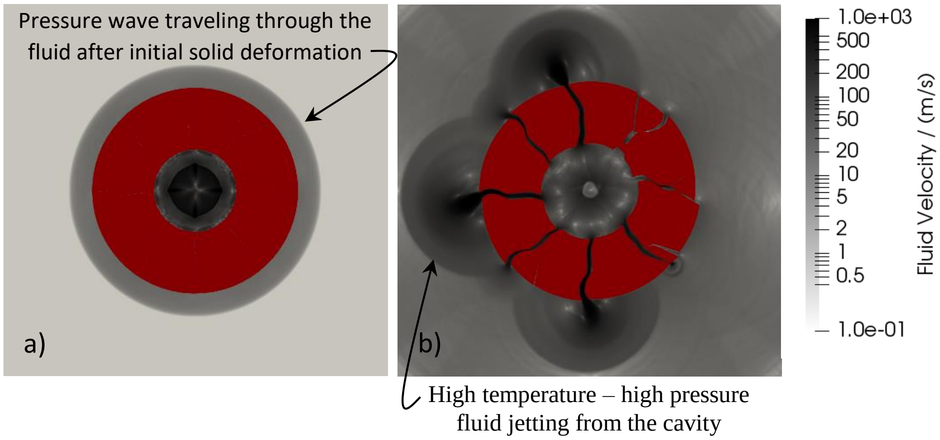

Pressure wave traveling through the fluid after initial solid deformation

High temperature – high pressure fluid jetting from the cavity

Figure 103. Map of the fluid velocity at different stages during the simulation. a) $t = 5.0e - 04$ s, b) $t = 4.0e - 03$ s.

4 Large Scale

4.1 Cross-validation of earthquake dynamic rupture modeling with HOSS

TYPE: Peer Reviewed Paper

REFERENCE: Dynamics, radiation and overall energy budget of earthquake rupture with coseismic off-fault damage. Journal of Geophysical Research: Solid Earth, 124. 2019. https://doi.org/10.1029/2019JB017304

AUTHORS: Kurama Okubo, Harsha S. Bhat, Esteban Rougier, Samson Marty, Alexandre Schubnel, Zhou Lei, Earl E. Knight, Yann Klinger

REFERENCE: Thesis: Dynamic earthquake ruptures on multiscale fault and fracture networks. Institut de Physique du Globe de Paris, 2018.

AUTHORS: Okubo, K.

ABSTRACT: We performed cross-validation of HOSS to assess the achievable accuracy of earthquake rupture modeling by comparing the results against other numerical schemes. In our analysis we chose the finite different method (FDM), the spectral element method (SEM) and the boundary integral equation method (BIEM) as comparison basis, which have been verified in previous studies. The cross-validation effort follows a similar process as the one proposed by Kaneko et al. (2008). The result shows the HOSS is capable of modeling dynamic earthquake ruptures as the evolution of slip velocity has an agreement with other verified numerical schemes. We also conducted a systematic parametric study associated with grid size and viscous damping, showing the reasonable combination of those parameters to archive numerical accuracy enough to resolve the dynamic earthquake rupture process.

PROBLEM DESCRIPTION:

Validation of 2-D in-plane dynamic earthquake ruptures.

We follow the version 3 of the benchmark problem proposed by the Southern California Earthquake Center/U.S. Geological Survey (SCEC/USGS) dynamic earthquake rupture code verification exercise (Harris et al., 2009), commonly used for cross-validating numerical schemes (Day et al., 2005; Kaneko et al., 2008; Rojas et al., 2008; De La Puente et al., 2009). The model is originally described in 3-D so that the 2-D analog model was used in this study, similar to Rojas et al. (2008), Kaneko et al. (2008), and De La Puente et al. (2009).

Figure 104 illustrates the model setup for the cross-validation, which has a single planar fault in the middle of a homogeneous and isotropic elastic medium. The linear slip-weakening law with zero cohesion is operating along the fault. Since the outer boundary edges are fixed, the model domain size is set large enough to avoid the interference from waves originating from reflected boundaries. The domain is discretized by spatially adaptive unstructured triangular mesh, where the element size is smallest on and around the fault, and increases in proportion to the distance from the main fault. The grid spacing is a priori defined uniformly on the fault itself. For the sake of cross-validation, the off-fault cracking is not allowed so that the off-fault medium behaves as a purely elastic material. Material constants and frictional properties are listed in Table 1. A slippery zone where frictional resistance is lower than outside is set in the middle of the fault to nucleate the earthquake rupture from the patch. The length of the slippery zone is slightly greater than the critical nucleation length at instability, L_c, derived by Palmer and Rice (1973) such as

$$L_c = \frac{2\mu D_c\left(\tau_p - \tau_r\right)}{\pi\left(\sigma_{yx}^0 - \tau_r\right)^2} \tag{50}$$

where μ is shear modulus, D_c is characteristic slip distance associated with slip-weakening law, τ_p , τ_r and σ_{yx}^0 are the peak strength, residual strength and initial shear stress on the pre-existing fault, respectively.

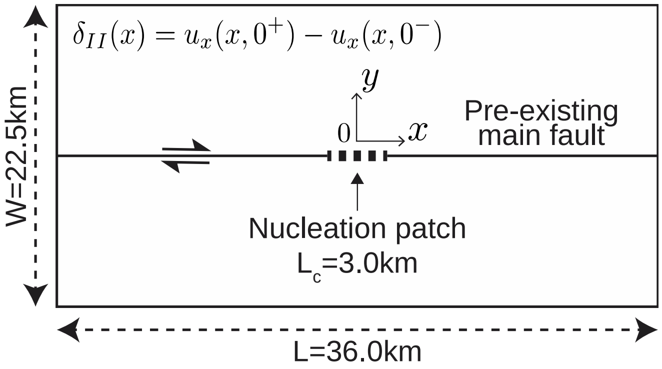

Figure 104. Schematic model for 2-D cross-validation. δ_{II} is relative slip on the fault defined as $u_x(x, 0^+) - u_x(x, 0^-)$

Table 14. Stress and Frictional Parameters used for 2-D Cross-validation.

Valuables (units)	Nucleation area	Outside Nucleation
σ_{yx}^{0} (initial shear stress, MPa)	70.0	70.0
$-\sigma_{yy}^{0}$ (initial normal stress, MPa)	120.0	120.0
f_s (peak friction)	0.554	0.677
f_d (residual/dynamic friction)	0.430	0.525
D_c (characteristic slip distance, m)	0.4	0.4
c_p (dilatation wave velocity, m/s)	6000.0	6000.0
c_s (shear wave velocity, m/s)	3464.0	3464.0
E (Young's modulus, GPa)	85.4	85.4
μ (shear modulus, GPa)	32.0	32.0
υ (Poisson's ratio)	0.33	0.33
τ_p (peak strength, MPa)	66.5	81.2
τ_r (residual strength, MPa)	51.6	63.0
$\Delta\sigma = (\tau_0 - \tau_r)$ (stress drop, MPa)	18.4	7.0

Note: $\Delta\sigma$ is the stress drop, where τ_0 is initial shear traction on the fault.

Since the shear traction and the slip rate vary significantly within the process zone around the rupture front, the resolution of the grid, often defined by the number of grid points within the process zone, is considered as a useful indication of the numerical accuracy in earthquake rupture modeling (Day et al., 2005). The dynamic process zone size, $R_f(v_r)$, is generally inversely proportional to the rupture velocity v_r, given by Rice (1980, eq. (6.16)) and Freund (1990, eq. (6.2.35)) such as

$$R_f(v_r) = A_{II}(v_r)^{-1} R_0 \tag{51}$$

$$A_{II}(v_r) = \frac{v_r^2 \alpha_s}{(1-\nu) c_s R} \tag{52}$$

where ν is Poisson's ratio, c_s is shear wave velocity, R_0 is the quasi-stationary process zone

$$R_0 = \frac{9\pi}{16(1-\nu)} \frac{\mu D_c}{(\tau_p - \tau_r)} \tag{53}$$

and

$$R = 4\alpha_s\alpha_p - \left(1+\alpha_s^2\right)^2 \tag{54}$$

$$\alpha_p^2 = 1 - \frac{v_r^2}{c_p^2} \tag{55}$$

$$\alpha_s^2 = 1 - \frac{v_r^2}{c_s^2} \tag{56}$$

where c_p is dilatational wave velocity. It is notable that the function $A_{II}\left(v_r\right)$ has the properties that $A_{II} \to 1$ as $v_r \to 0^+$ and $A_{II} \to \infty$ as $v_r \to c_R$, where c_R is the Rayleigh wave speed as the limiting speed in the context of sub-Rayleigh rupture. Thus, the process zone size gradually shrinks and asymptotically converges to zero as the rupture velocity approaches c_R, which is typically known as Lorentz contraction. The process zone resolution is defined with the median value of $R_f\left(v_r\right)$ in previous studies (Day et al., 2005; Kaneko et al., 2008), providing the effective grid resolution of the process zone through the simulation. However, for the sake of simplicity, we use the quasi-stationary process zone size R_0 for evaluating the grid resolution. Thus, the process zone resolution in this study implies an indication of numerical accuracy related with grid size rather than the actual number of grid points within the actual process zone size during the dynamic rupture propagation.

RESULTS: Figure 105 shows the comparison of evolution of slip velocity on the fault, and Figure 106 shows the comparison of slip velocity history at x = 9 km from the center of the main fault. The results of HOSS are compared with other results by FDM, SEM and BIEM, where the grid spacing on the fault is chosen for the highest resolution as $\Delta x = 8$ m ($R_0/\Delta s = 116$) for HOSS, FDM and BIEM and $\Delta x = 10$ m ($R_0/\Delta s = 93$) for SEM. Note that in the framework of SEM, to effectively enhance the numerical accuracy, Lagrange polynomials are chosen as a basis function for the Galerkin method and an element is then discretized by the Gauss-Lobatto-Legendre (GLL) points for the numerical integration, which is not spatially uniform. Thus, the grid spacing of SEM is evaluated by average spacing, which implies the minimum grid spacing of SEM is equivalent to $\Delta x = 8$. The oscillation of slip velocity observed in FDM, SEM and the BIEM results is related to artificial viscous damping. There is no viscous damping in the BIEM and the FDM, whereas the SEM utilizes the Kelvin-Voigt viscous damping. The value of viscosity for the SEM is carefully chosen to avoid over damping of rupture propagation. For HOSS, we applied Munjiza viscosity, which is high enough to removes the high-frequency numerical noise. It is notable that the comparison of HOSS results to BIEM is no longer fair due to the artificial viscous damping, so that the systematic evaluation of viscous damping was conducted to investigate the effect of the viscosity on the dynamic rupture propagation in the following section.

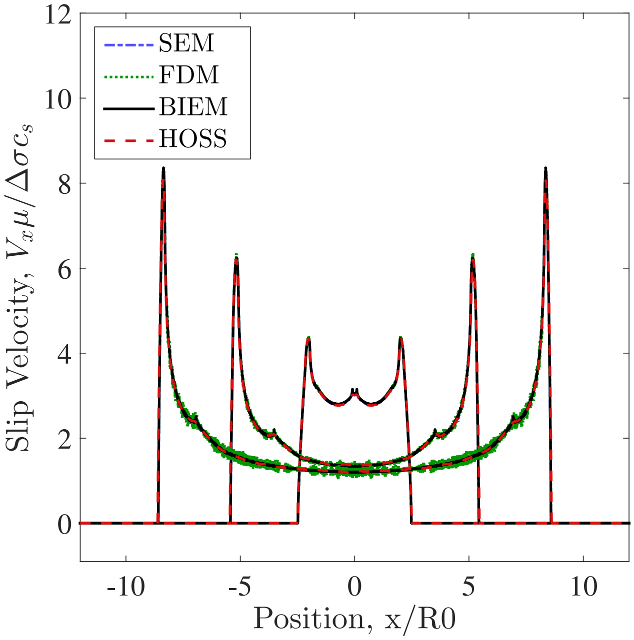

.

Figure 105. Comparison of the evolution of slip velocity with time. The rupture propagates bilaterally on the pre-existing fault. Red dotted line shows the result with HOSS, which has an agreement with other schemes. The numerical oscillation associated with FDM is due to no artificial damping.

The slip velocity of HOSS is globally in accordance with the other methods except for the peak slip velocity. The numerical oscillation is suppressed by artificial viscous damping with the result for HOSS. The peak slip velocity of HOSS is 4.1 percent smaller than that of BIEM, and the rupture arrival time is slightly faster than the others. Both of the small discrepancies are explained by the artificial viscous damping applied on the whole medium by the Munjiza viscosities such that the strain rate-dependent viscosity smooths the rise of slip velocity, which causes the reduction of the peak velocity and accelerates the rupture arrival time.

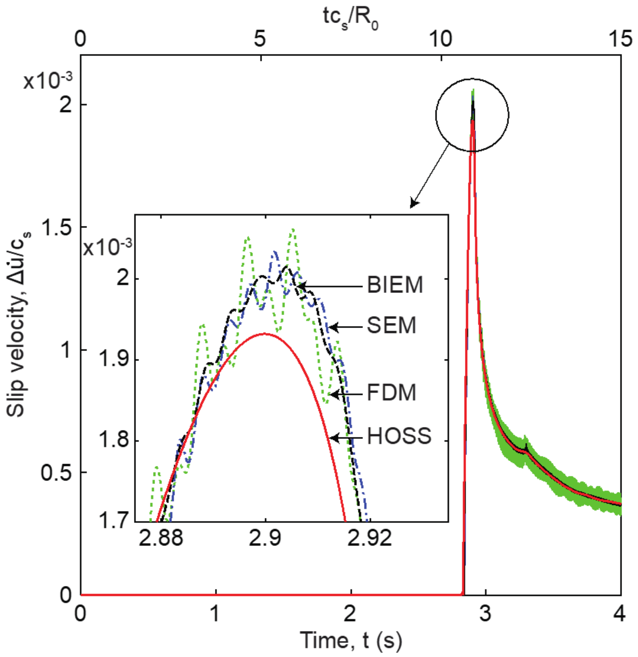

Figure 106. Slip velocity histories at x = 9.0 km ($x/R_0 = 9.7$). The grid size on the fault is 8 m ($R_0/\Delta x = 116$) for HOSS, FDM and BIEM and 10 m ($R_0/\Delta x$ = 93) for SEM. The HOSS simulation is performed with one point per edge. The inset shows the focused window around the peak velocity at t = 2.9s.

Figure 107 shows the grid convergence of HOSS and other results. The numerical accuracy as a function of grid resolution is evaluated by the root-mean-square (RMS) difference, interpolated with the spacing of 100 m over the right side of the fault region given by 3.0 km ≤ x ≤ 9.0 km in the same manner proposed by Kaneko et al. (2008). The RMS error of the rupture arrival time is defined by the comparison to the benchmark solution provided by the solution of BIEM with highest resolution. The convergence rate of HOSS is similar with the BIEM following the power law with the scaling exponent of 1.6 for HOSS and 1.4 for BIEM though the RMS error is slightly higher than the FDM and SEM due to the viscosity. Thus, the numerical accuracy is assured with proper grid size Δs small enough to satisfy the required error range of the earthquake rupture modeling.

Error assessment with various artificial viscous damping.

As mentioned above, the high-frequency numerical oscillation is suppressed by the viscous damping, whereas the smoothed velocity field causes the reduction of the peak velocity and the acceleration of rupture arrival time as shown in Figure 3. Thus, the evaluation of the effect of artificial viscous damping is required to assess the numerical precision of the earthquake rupture modeling. Figure 108 shows the RMS error of the rupture arrival time with various viscosity values and grid resolutions with the highest resolution of BIEM as reference.

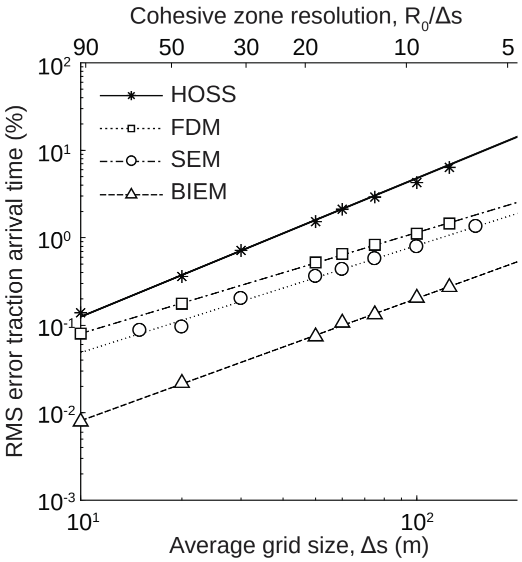

Figure 107. Grid convergence as a function of process zone resolution. The RMS error is calculated by the comparison of rupture arrival time to the benchmark result provided by the highest resolution solution of BIEM at linear interpolated points with the spacing of 100 m over the fault region given by $3.0 \le x \le 9.0$ km. The HOSS simulations are performed with two points per edge.

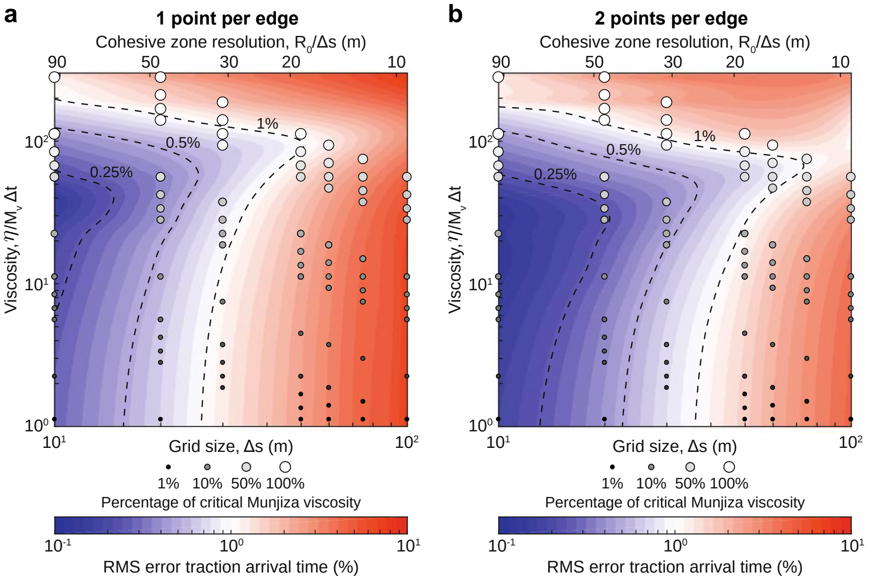

Figure 108. RMS error of the rupture arrival time with viscous values and grid resolutions. (a) shows the error with one point per edge of element, while (b) with two points per edge. The circles show the tested combinations of the viscous values and grid resolutions, where the size of circles with monochromatic gradation represents the proportion of viscous values to the critical viscosity (the viscosity is higher with white and large circles). The color contour is interpolated with the tested combinations. Viscosity is nondimensionalized by the Munjiza elastic constant, M_v, and the time step Δt.

The number of points per edge is defined as that of target points within the edge of elements at which the contact force is evaluated, which plays a significant role on the integration accuracy of the distributed contact forces. We performed the analysis of the RMS error with one point and two points per edge. Grid size is defined by the spacing of the grids on the fault, while the process zone resolution is evaluated by R0/Δx, same as Figure 108. The viscous damping is controlled by the dynamic viscosity η, input into the FDEM framework in the form of Munjiza viscosity.

The dynamic viscosity is then nondimensionalized by the volumetric Munjiza elastic constant, Mv, and the time step Δt. Note that the time step is constant during the simulation. The derivation of the Munjiza elastic constants are documented in Munjiza et al. (2015, Chapter 17). In Figure 109, the circles indicate the tested combinations of the viscosity values and the grid resolutions, where the size of circles with monochromatic gradation represents the proportion of the viscous values to the theoretically derived reference viscosity, called the critical viscosity ($M_v^c = 2h_{min}\sqrt{\rho M_v}$, where h_{min} is the length of minimum edge among all elements). The RMS error is desirable with proper combi- nation of the viscous damping and grid resolution. The saddle of the RMS error along η/M_v Δt ≈ 102 is explained by the competition between the numerical oscillation and the overdamped system. In addition, it is clearly shown that the convergence of the RMS error is better with the two integral points per edge. Hence the grid resolution, viscosity values and the number of points per face should be carefully chosen for the required numerical accuracy. Since the number of points per edge should be more than two to allow for the secondary cracks in off-fault medium due to numerical reasons, we chose the proper grid size and viscosity based on Figure 109 for the dynamic rupture modeling with off-fault damage.

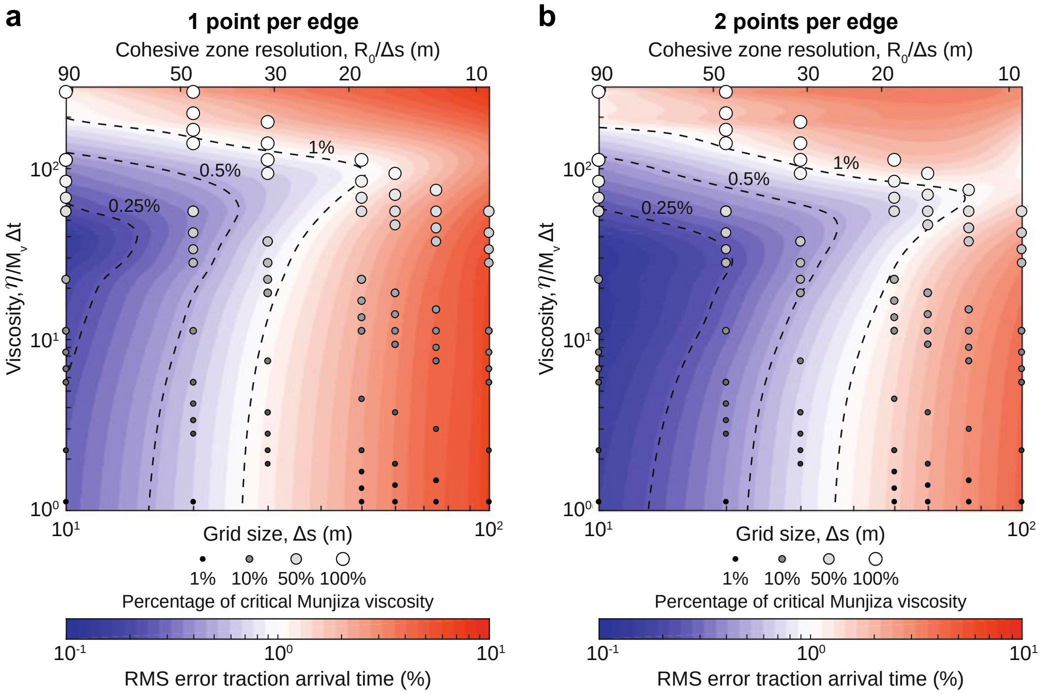

Figure 109. RMS error of the rupture arrival time with viscous values and grid resolutions. (a) shows the error with one point per edge of element, while (b) with two points per edge. The circles show the tested combinations of the viscous values and grid resolutions, where the size of circles with monochromatic gradation represents the proportion of viscous values to the critical viscosity (the viscosity is higher with white and large circles). The color contour is interpolated with the tested combinations. Viscosity is nondimensionalized by the Munjiza elastic constant, M_V, and the time step Δt.

References:

Day, S. M., Dalguer, L. A., Lapusta, N., and Liu, Y. (2005), Comparison of finite difference and boundary integral solutions to three-dimensional spontaneous rupture, J. Geophys. Res., 110, B12307, doi:10.1029/2005JB003813.

de la Puente, J., Ampuero, J.-P., and Käser, M. (2009), Dynamic rupture modeling on unstructured meshes using a discontinuous Galerkin method, J. Geophys. Res., 114, B10, doi:10.1029/2008JB006271.

Freund, L. B. (1990), Dynamic Fracture Mechanics, Cambridge {U}niversity {P}ress.

Harris, R. A., Barall, M., Archuleta, R. J., Dunham, E. M., Aagaard, B., Ampuero, J.-P., Bhat, H. S., Cruz-Atienza, V., Dalguer, L., Dawson, P., Day, S. M., Duan, B., Ely, G., Kaneko, Y., Kase, Y., Lapusta, N., Liu, Y., Ma, S., Oglesby, D. D., Olsen, K. B., Pitarka, A., Song, S., and Templeton, E. L. (2009), The SCEC/USGS dynamic earthquake rupture code verification exercise, Seismol. Res. Lett., 80, 1, doi:10.1785/gssrl.80.1.119.

Kaneko, Y., Lapusta, N., and Ampuero, J. P. (2008), Spectral element modeling of spontaneous earthquake rupture on rate and state faults: Effect of velocity-strengthening friction at shallow depths, J. Geophys. Res., 113, B09317, doi:10.1029/2007JB005553.

Munjiza, A., Knight, E. E., and Rougier, E. (2015), Large strain finite element method: a practical course, John Wiley \& Sons.

Palmer, A. C. and Rice, J. R. (1973), Growth Of Slip Surfaces In Progressive Failure Of Over-Consolidated Clay, Proc. R. Soc. Lond. Ser-A, 332, 527–548, doi:10.1098/rspa.1973.0040.

Rice, J. R. (1980), The mechanics of earthquake rupture, in Physics of the earth's interior (Proc. Intn'l. School of Physics `Enrico Fermi', Course 78, 1979), Italian Physical Society and North-Holland Publishing Co., Amsterdam, edited by Dziewonski, A. M. and Boschi, E., pp. 555-649.

Rojas, O., Day, S., Castillo, J., and Dalguer, L. A. (2008), Modelling of rupture propagation using high-order mimetic finite differences, Geophys. J. Int., 172, 2, 631–650, doi:10.1111/j.1365-246X.2007.03651.x.

4.2 Simulation of hypervelocity impact using the combined-finite discrete element method

TYPE: Internal Report

REFERENCE: N/A

AUTHORS: Bryan Euser, Esteban Rougier, Earl E. Knight, Zhou Lei

ABSTRACT: Traditionally, empirical laws have been used to determine the seismic efficiency of bolide or asteroid impacts. However, empirical laws are not always reliable since they provide seismic efficiency estimates that vary from 10^{-2} to 10^{-5}. Recent developments in numerical methods and the increase of computing power make numerical modeling a promising alternative to investigate the physics of impacts to provide answers to the outstanding question of seismic efficiency. The goal of this work is to understand the dependence of the seismic efficiency variability on the impactor characteristics (mass, velocity, angle of attack), geologic structure of the target medium and the properties of the ground. For this analysis we are using an in-house multiphysics code called HOSS (Hybrid Optimization Software Suite) which is based on the combined finite-discrete element method [1-3].

PROBLEM DESCRIPTION: The simulations consider a 1 km diameter body impacting a 15km diameter half space, which is based on another verification/validation paper (Pierrazzo et al., 2015). Data is collected at a variety of locations and is then compared to data from other hydrocodes simulations of the same problem. The simulations consider two different impact velocities with cases for both normal and oblique impacts.

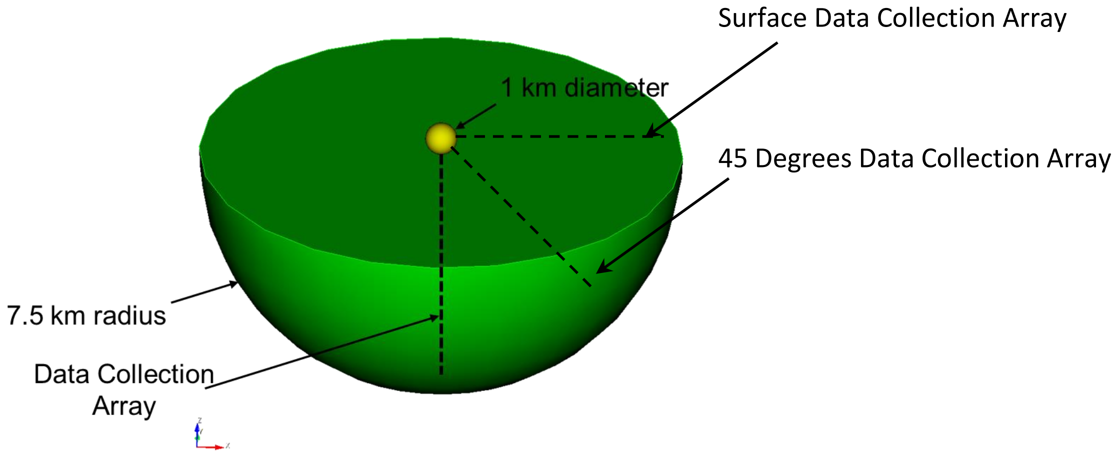

Figure 110. General model setup for the hypervelocity impact simulations, a normal (90° with respect to horizontal) impact and oblique (45° with respect to horizontal) are considered. Lines along which the data collection arrays were set are indicated.

RESULTS

Two snapshots showing the wave propagation and the material being ejected for the vertical and the 45 degree angle impacts with an initial projectile velocity of 5 km/s are shown in Figure 111 and Figure 112.

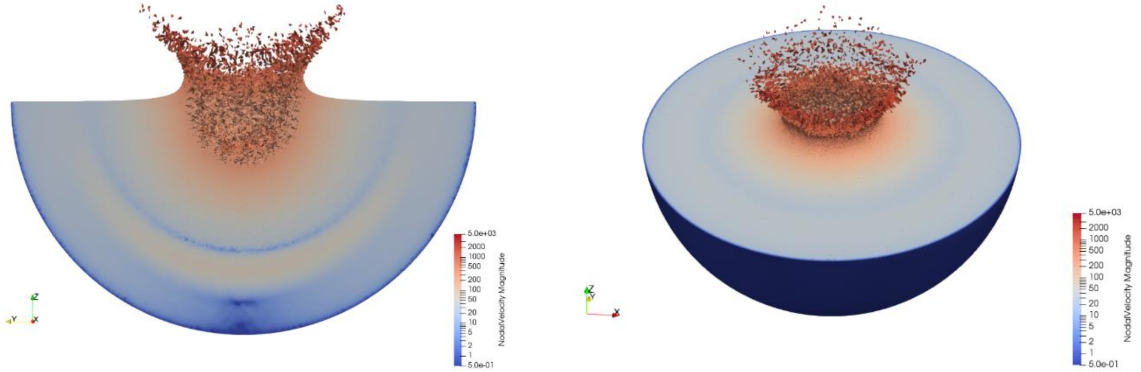

Figure 111. Results from a simulation of a normal impact with an impact velocity of 5 km/s.

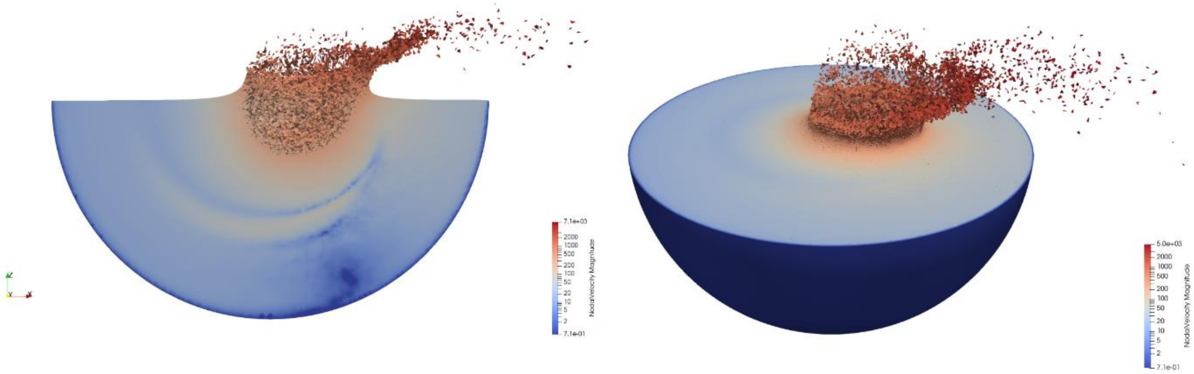

Figure 112. Results from a simulation of an oblique impact with an impact velocity of 5 km/s.

Comparisons of the calculated peak pressure with distance for the vertical impact case with initial velocities of 5 km/s and 20 km/s are shown in Figure 113 and Figure 114. There is a very good agreement between the results obtained with HOSS and those obtained with other hydrocodes.

For the oblique impact case with an initial velocity of 20 km/s the comparison of the peak pressure with range for the vertical data collection array is shown in Figure 114, while the results obtained for the horizontal data collection array are shown in Figure 115. For the vertical data collection array there is a very good agreement for the near source peak pressure and for the decay with distance. A peak in the peak pressure obtained with HOSS in the region connecting the near source with the decay is observed. This difference is currently being studied.

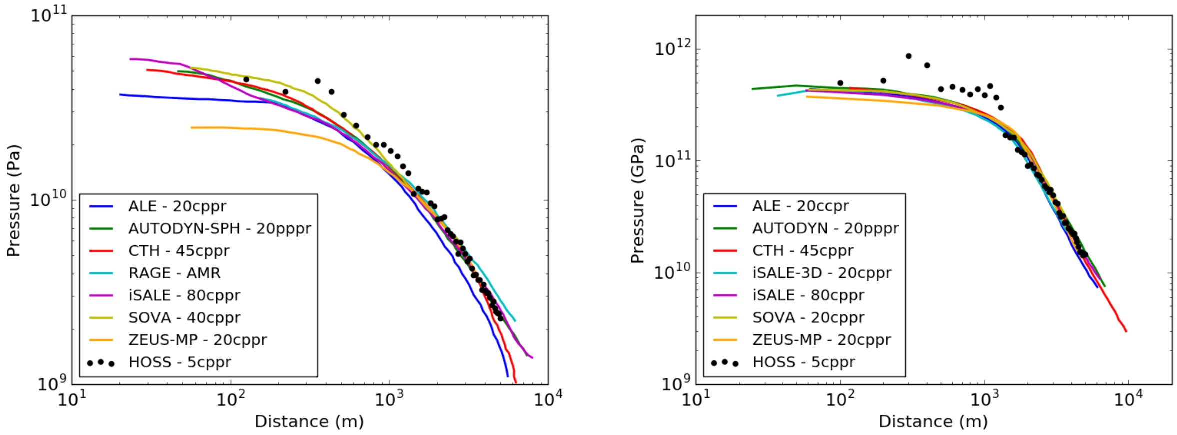

Figure 113. Vertical pressure decay versus distance for a normal impact with: a) impact velocity of 5 km/s. b) impact velocity of 20 km/s.

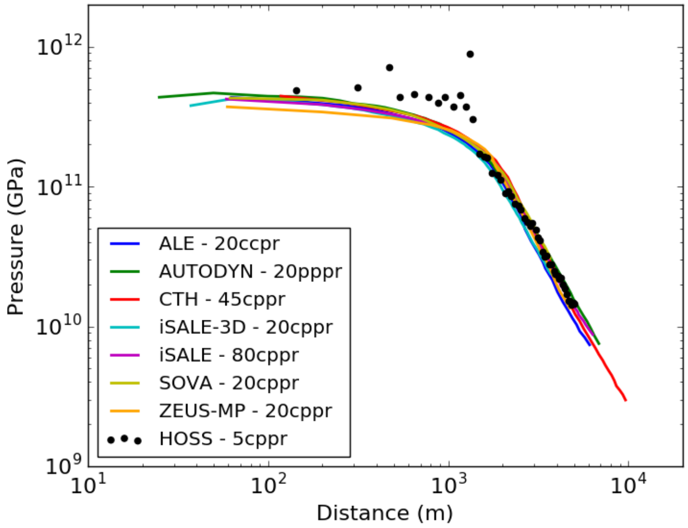

Figure 114. Vertical pressure decay versus distance for an oblique impact with an impact velocity of 20 km/s.

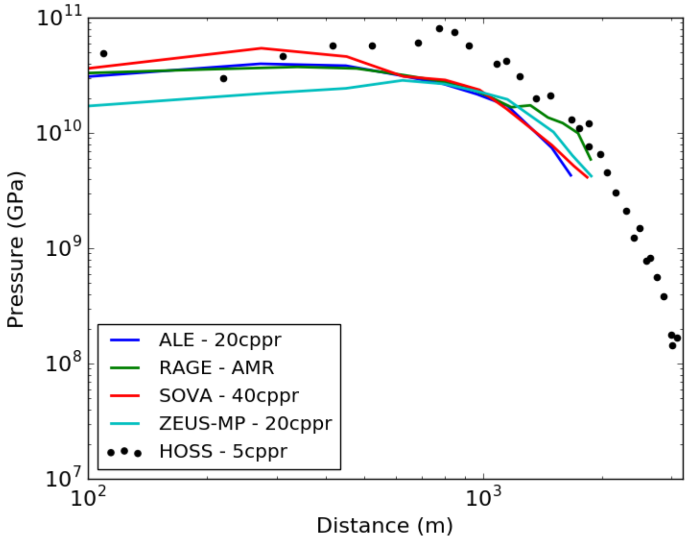

Figure 115. Horizontal pressure decay versus distance for an oblique impact with an impact velocity of 20 km/s.

References

Munjiza (2004) John Wiley & Sons, Ltd, doi:10.1002/0470020180
Munjiza, Knight, Rougier (2011) John Wiley & Sons, Ltd, doi:10.1002/9781119971160
Munjiza, Rougier, Knight (2015) John Wiley & Sons, Ltd, ISBN: 978-1-118-40530-7
Pierazzo et al., (2008), vol. 43, pp. 1917–1938.

4.3 Source Physics Experiment's (SPE) Phase 1

TYPE: Conference Paper

REFERENCE: Effect of damage and spallation on Rg waves for SPE-5. AGU Fall Meeting, Washington, D.C., Dec 10–14, 2018. http://adsabs.harvard.edu/abs/2018AGUFM.S21D0474L

AUTHORS: Z. Lei, E. Rougier, H.J. Patton, C. Larmat, C. Bradley.

ABSTRACT: Advances in numerical methods and computing power now allow the exploration of the effects of damage and spallation on the generation of seismic waves by underground explosions. In this work, HOSS is used to model the non-linear near-source area via the implementation of equations of state for the explosive and the surrounding material which are subjected to very high strain rate regimes, with large deformation and also fragmentation. A major advantage of HOSS in this study, relative to some traditional continuum based tools, is that it describes the dynamic fracture and spallation explicitly. In addition, this work also enabled the incorporation of pre-existing damage in the material, which proves to be an important factor in the estimated spall for the SPE-5 event. Furthermore, it has been found that the larger extent of damage observed in the simulations for SPE-5 is in agreement with the image survey of the surface deformation after taking into account the pre-existing damage that was generated by SPE-2.

PROBLEM DESCRIPTION: The main focus of the Source Physics Experiment (SPE) is to bring empirical and theoretical advances to the problem of detection and identification of underground explosions. SPE consists of a series of chemical explosions in each of two phases: Phase I in granite and Phase II in dry alluvium. Phase I included six tests with explosive sources of varying yield and depth. A schematic view of the model used for the hydrodynamic simulations is shown Figure 116. Both the SPE-2 and SPE-5 sources are considered in this model. Based on the geologic characterization, the model considered three different layers of material: the intact granite, where the shots were detonated; the weathered granite, which is located on top of the intact granite layer; and the test pad, which is composed of a fill material with properties corresponding to dirt. The aim was to estimate the damage generated by the SPE-5 source while taking into account the damage introduced by SPE-2. Since the focus is on the spallation signal and damage near the free surface, the geometry used for this analysis consists of a 1/8th symmetric model centered on the SPE-5 event. The intact granite was modeled using a pure FEM mesh (i.e. no explicit fracture processes), while the weathered and the test pad layers were modeled using a hybrid FDEM mesh that allows for fracture and fragmentation of the material.

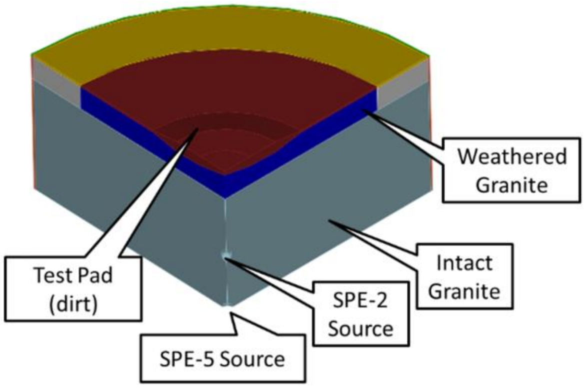

Figure 116. Schematic description of the numerical model used in the HOSS simulations.

RESULTS: In the following, we show damage and spallation results obtained using HOSS for SPE-2 and SPE-5. SPE-2 was the first experiment of the series expected to create significant subsurface damage. Our modeling confirms the existence of such damage (within the weathered and the dirt layers) as shown in Figure 59.

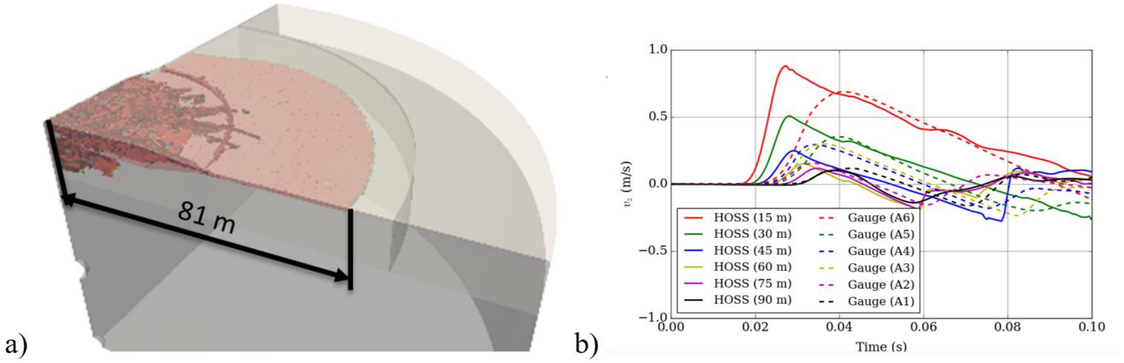

Figure 117. a) Fracture patterns (damage) obtained after SPE-2. b) Comparison between numerical results and observations of the spallation signals for the surface gauges.

It can be seen from Figure 59 that the fractures are concentrated on the top two layers of the model, defining a conical area of damage that, at ground zero, has almost the same depth as the weathered-dirt layers combination. This damage area is generated upon the reflection of the stress wave from the free surface. There is also a "de-lamination" process that occurs between the weathered granite material and the dirt layer. The range of the fractures measured from GZ is around 81 m, which is in good agreement with observations that showed spallation (i.e. fracturing of the top layers) between 90 m and 100 m from GZ. A series of monitoring points were placed in the upper layer of the model in order to capture the spallation signal with range. The comparison between the numerical results and the observation for SPE-2 are shown in Figure 59-b. The arrival of the signal in the numerical model happens earlier than in the experiments. The numerical model does over-predict the peak velocity for gauges A6 and A5, however the results for the other gauges are in line with the observations. The numerical model calculates spallation signals (acceleration of -1 g) for all the gauges up to 75 m range, which is in good agreement with the observations.

This damage map is then preserved for the simulation of the SPE-5 experiment. The results obtained after SPE-5 are shown in Figure 118. The extent of the fractures near the surface is now approximately 90 m (Figure 118-a). The comparison of the spallation signals obtained from the model with those observed is shown in (Figure 118-b). In this case, the peak velocity is over-predicted for gauge A5, while it is under-predicted (by between 10 and 15%) for all of the other gauges. A clear spallation signal is seen for the numerical results corresponding to gauges A2 though A6. As it was the case for SPE-2 the signal arrives to the surface sooner than in the observations.

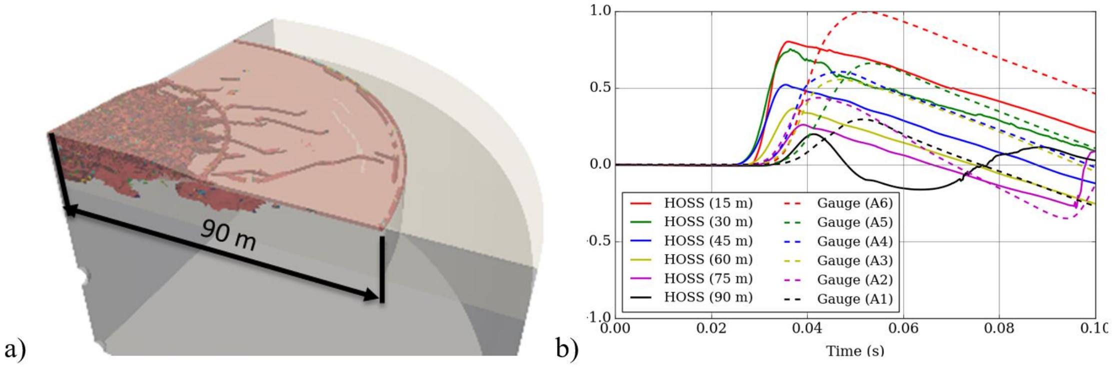

Figure 118. a) Fracture patterns (damage) obtained after SPE-2. b) Comparison between numerical results and observations of the spallation signals for the surface gauges.

4.4 Earthquake Gouge - Modeling of Stick-Slip Behavior in Sheared Granular Fault Gouge Using the Combined Finite-Discrete Element Method

TYPE: Peer Reviewed Paper

REFERENCE: (2018). Modeling of Stick-Slip Behavior in Sheared Granular Fault Gouge Using the Combined Finite-Discrete Element Method. Journal of Geophysical Research: Solid Earth, 123, 5774– 5792. https://doi.org/10.1029/2018JB015668

AUTHORS: Gao, K., Euser, B. J., Rougier, E., Guyer, R. A., Lei, Z., Knight, E. E., Johnson, P. A.

ABSTRACT: The presence of randomly packed solid granular particles in fault gouge has considerable influence on the slip properties of tectonic faults. Therefore, sheared granular layers undergoing stick-slip behavior are broadly employed to study the physics and dynamics of earthquakes. Here, a two-dimensional implementation of the combined finite-discrete element method (FDEM), which merges the finite element method (FEM) and the discrete element method (DEM), is used to explicitly simulate a sheared granular fault system including both gouge and plate. In the FDEM model, the deformation of plates and particles is simulated using the FEM formulation while particle-particle and particle-plate interactions are modeled using DEM-derived techniques. The simulation results show great agreement with the physical experiment in terms of the distribution of the size of seismic events.

PROBLEM DESCRIPTION: Among the many numerical methods used to describe the evolution of granular systems, the discrete element method (DEM) has been the most popular. However, DEM is incapable of capturing real and detailed deformation and stress distributions within the particles and plates. The combined finite-discrete element method (FDEM), which merges finite element based analysis of continua with discrete element based transient dynamics, contact detection and contact interaction solutions of discontinua, provides a natural solution to modeling such fault system.

Figure 119 illustrates the geometry of the FDEM model, which is based on the two-dimensional, photoelastic shear laboratory experiment conducted by Geller et al. (2015). The model consists of 2,817 non-destructive circular particles confined between two identical plates. Each main plate has dimensions of 570 × 250 mm in width and height, respectively. At the interface between the main plates and the particles, a series of half-circular shaped "teeth" are added to the plates to increase the friction between plates and particles and, thus, facilitate the transmission of shear stresses (Figure 120). A number of "sensor" points are set on both plates and particles in order to track the motion of different components of the system. A series of relatively small normal loads ranging from 12 kPa to 44 kPa, in increments of 8 kPa, are employed to investigate the influence of different loading conditions on the stick-slip behavior of the gouge. A shear velocity of V = 0.5 mm/s is selected, which guarantees the occurrence of slip events.

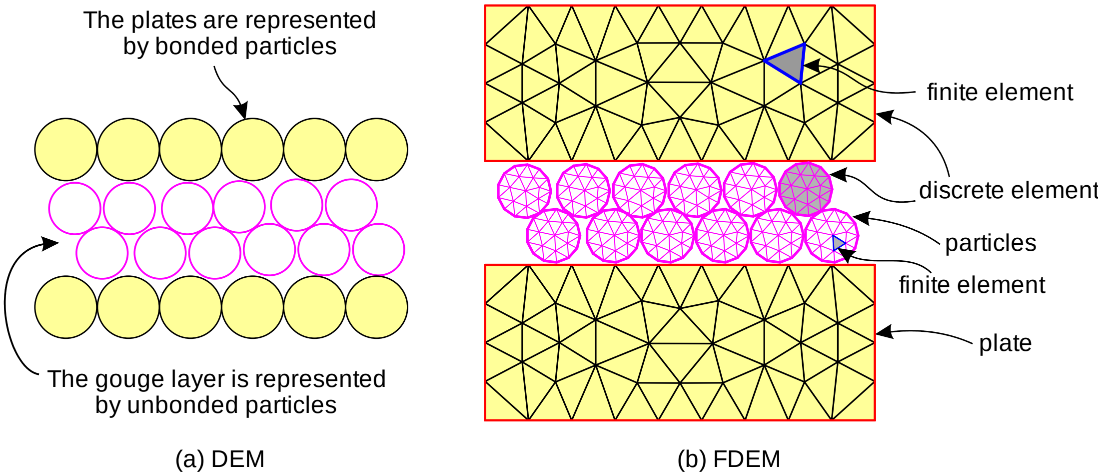

(a) DEM (b) FDEM

Figure 119. Numerical representation of the fault containing granular fault gouge using the DEM and FDEM. (a) In the DEM the plates are simplified by a set of bonded particles and the gouge layer is composed of a series of rigid particles. (b) In the FDEM the plate is explicitly represented and both plates and particles are further discretized into finite elements to capture their deformation and stress evolution.

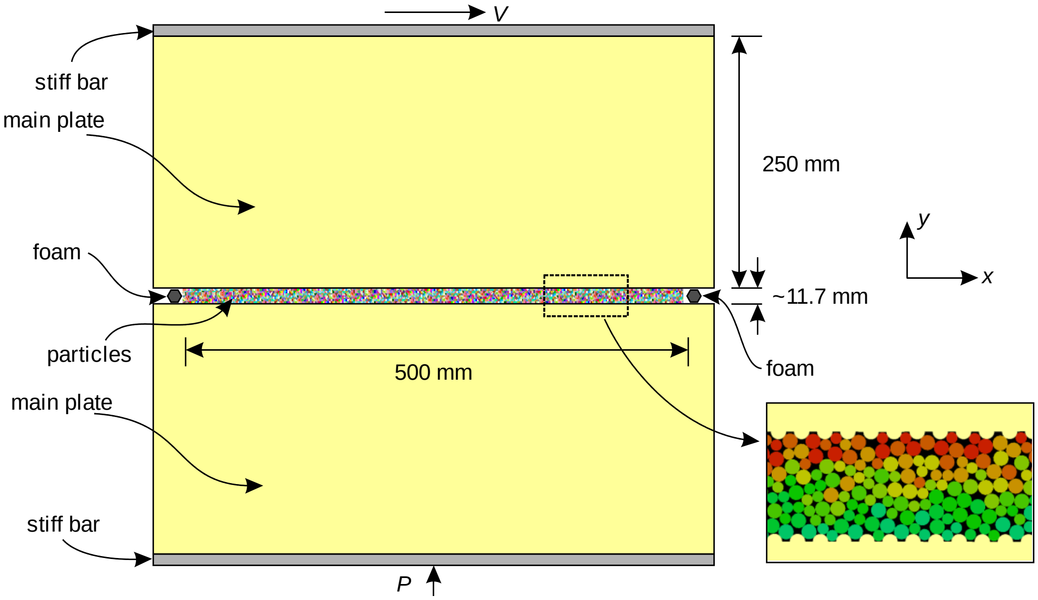

Figure 120. FDEM model of the granular gault gouge system and its geometrical dimensions.

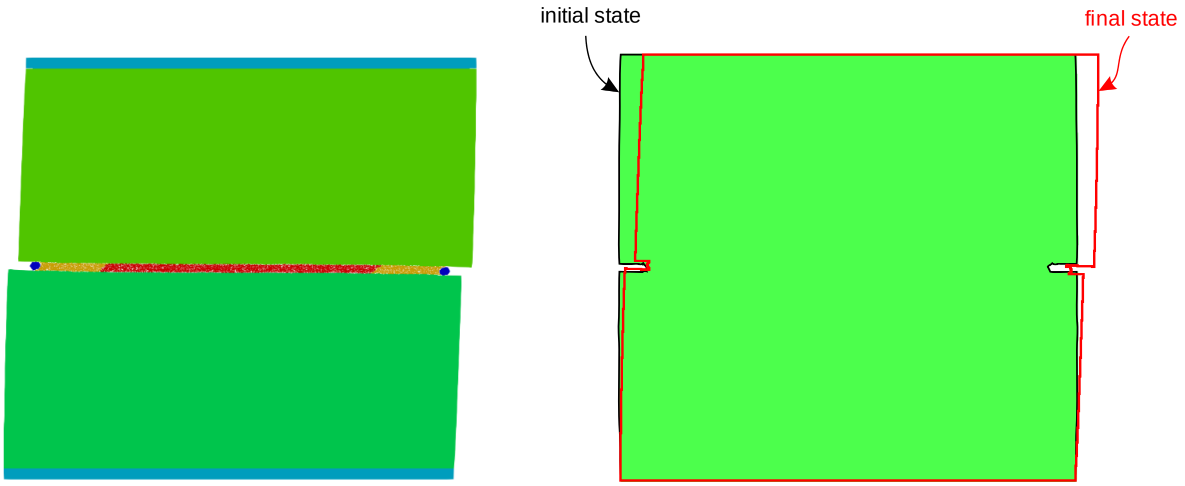

(a) Final state (end of shear) (b) Overlay of the outlines of beginning and final state

Figure 121. Deformation of the granular fault gouge system subjected to 44 kPa normal load: (a) final state of the model, i.e., at the end of shear; (b) overlay of the outlines of the initial (i.e., at the beginning of shear) and final states of the model according to their coordinates.

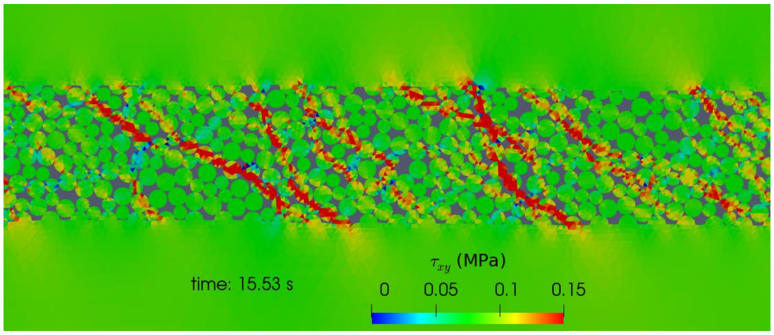

(a) Stress concentration in the granular fault gouge immediately before a slip event

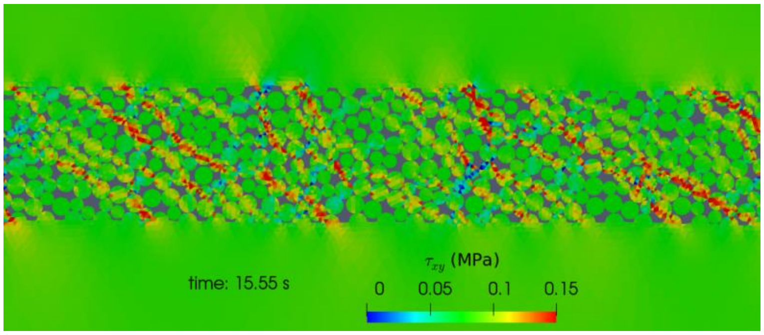

(b) Relatively more uniform stress distribution in the granular fault gouge immediately after the slip event

Figure 122. Stress evolution in the granular fault gouge immediate (a) before and (b) after a slip event for the fault subjected to 44 kPa normal load. (Note that only part of the fault gouge is presented and locations of these two stages on the time series plot is further marked).

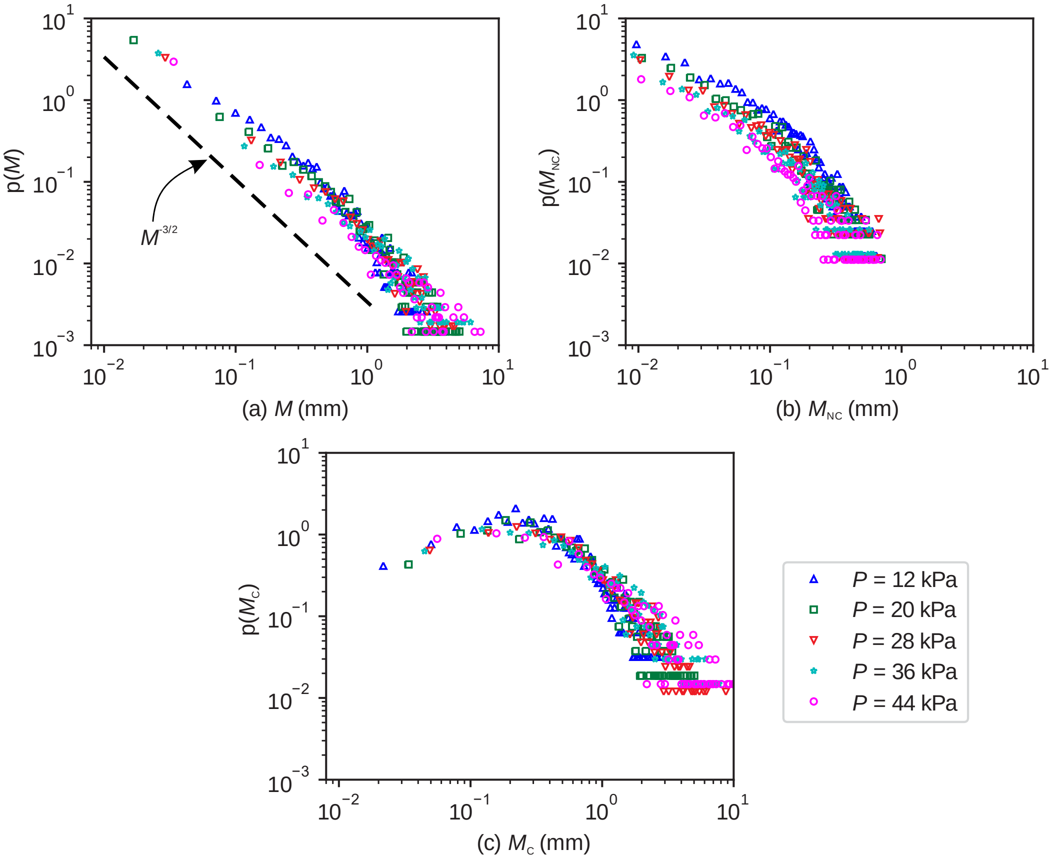

Figure 123. Probability density distribution of the seismic moment of (a) all events, (b) NC events and (c) C events for different normal loads.

Figure 123 illustrates the probability density distributions of all, None-Cohesion (NV) and Cohesion (C) events. The results agree with the experimental data collected by Geller et al. (2015). The probability density distribution of all events $p(M)$ is consistent with the Gutenberg-Richter law (Gutenberg & Richter, 1955) and is predicted to scale as $M^{-3/2}$ (the power -3/2 is within the range of -1.4 to -1.8 observed in real earthquake (Geller et al., 2015)) (Figure 123a). The NC events are generally distributed as a power law consistent with $M^{-3/2}$ (Figure 123b). The C events are broadly peaked, concentrated at large M with a probability density distribution that consistent with log-normal (Figure 123c). The simulated results using FDEM are not only consistent with the laboratory experiments, but also agree with our observations of increased likelihood of large seismic moments at higher normal load (Geller et al., 2015). This also demonstrates that it is the capability of FDEM for explicit plate deformation simulation that makes the seismic moment analysis possible.